Study of aerodynamic interactions in counter-rotating coaxial rotors

by

Lokesh Silwal

A dissertation submitted to the Graduate Faculty of
Auburn University
in partial fulfillment of the
requirements for the Degree of
Doctor of Philosophy

Auburn, Alabama
December 9, 2023

Keywords: Multi-rotors, Counter-rotating coaxial rotors, Ground effect, Blade crossover

Approved by

Vrishank Raghav, Chair, Associate Professor of Aerospace Engineering
Brian S. Thurow, Chair, W. Allen and Martha Reed Professor of Aerospace Engineering
Roy Hartfield, Walt and Virginia Woltosz Professor
Anwar Ahmed, Professor of Aerospace Engineering
Mahendra Bhagwat, Senior Research Scientist

Abstract

Counter-rotating coaxial rotors (CCR) are ubiquitous in emerging next-generation configurations, demonstrating enhanced performance metrics such as increased forward-flight speed, flight range, and payload capabilities compared to single-rotor configurations. At the same time, multiple rotors in the CCR also result in high aerodynamic interactions that govern their performance. Therefore, it is necessary to better understand the nature and influence of these aerodynamic interactions. This dissertation seeks to address this knowledge gap by undertaking experimental investigations into the impact of select aerodynamic interactions on the performance of counter-rotating coaxial rotors. The primary focus is on studying the effects of rotor-ground and blade-on-blade interactional effects, specifically in hovering flight in close proximity to the ground.

The rotor-ground interactions significantly alter the hover performance of a rotor operating in ground effect (IGE). In the case of the CCR, the individual rotors interact with each other and the ground plane, leading to a complex aerodynamic environment. Through a rigorous experimental investigation, this dissertation shows that the CCR behaves as a single rotor when operating in IGE despite these interactional effects. However, the individual rotors in CCR show very different performance behavior compared to a single rotor, contingent upon rotor spacing and proximity to the ground plane. Similarly, the blade-on-blade interaction in CCR occurs during the crossover between the upper and lower rotor blades. These periodic events introduce transient excursions in airloads, resulting in vibratory loads and potential alterations to the vehicle's acoustic signature. This dissertation studies the fundamental physics of these interactional effects, employing a canonical representation of the problem, i.e., a crossover between two translating airfoils. The investigation identifies key non-dimensional parameters influencing the problem and observes a significant analogy between blade crossover and gust interaction problems. In particular, applying the Kussner model, commonly used to predict the

response of airfoil lift to gusts, demonstrates promising predictive capabilities, especially in the initial stages of blade crossover.

Acknowledgments

I would like to express my profound gratitude to the forces of destiny for granting me the opportunity, the resilience, and the strength to fulfill a childhood dream. This dream, which I carry on behalf of my family, holds a deep and significant place in my heart. I dedicate this document to those who have been my unwavering pillars of support.

First, I acknowledge my family, the bedrock of my life's journey. My grandfather, whose name I bear, instilled a sense of identity and purpose. My grandmother, pivotal in my upbringing, has left an indelible mark on my character. My mother, Tulasa Mainali, a constant source of inspiration, lived vicariously through my dreams, guiding me to pursue my dreams. My father, Chhabiraman Silwal, has been a constant source of unconditional love and trust, inspiring me in every endeavor. This document stands as a testament to their hopes and dreams, and it is for them that I have pursued my path with dedication and perseverance.

My academic journey has been enriched by the guidance and mentorship of my advisor, Dr. Vrishank Raghav. I express my heartfelt gratitude for his unwavering support and the challenges he presented, which have propelled me to achieve the best I can. I also deeply appreciate the members of my esteemed committee, Dr. Brian Thurow, Dr. Anwar Ahmed, Dr. Roy Hartfield, and Dr. Mahendra Bhagwat, for their constant support and invaluable suggestions.

The Department of Aerospace Engineering at Auburn University has nurtured my growth as a researcher. I am grateful for the environment that it provided to foster my academic journey. My lab members and colleagues have been more than collaborators; they have been friends who provided unwavering support, making the research journey enjoyable.

I appreciate the undergraduate researchers who joined me at various stages of my journey. Your dedication and contributions have been crucial in completing my dissertation. I have also enjoyed the opportunity to mentor and learn from you. I would like to mention Mr. Andy Weldon from the Aerospace Engineering Department at Auburn University, whose remarkable

patience and unique skills brought my CAD designs to life. Your contributions have been invaluable, and I am deeply grateful for your help.

Participating in the Plume-surface interaction project, funded by NASA's Early Stage Innovations grant, has been a tremendous learning experience. I wish to extend my heartfelt thanks to my partner in this project, Daniel Stubbs. Beyond being a colleague, you have been a true friend and an outstanding engineer. Our collaboration has been a source of enlightenment and personal growth. I also thank Dr. David Scarborough and Dr. Brian Thurow for their valuable insights and guidance during our collaboration.

I would like to acknowledge the pivotal role played by NASA, including Dr. Ashley Korzun at NASA Langley Research Center, Dr. Wesley Chambers at NASA Marshall Space Flight Center, and Dr. James Mantovani from Kennedy Space Center. Their support and collaborative spirit have been instrumental in the success of our research endeavors.

Furthermore, the final years of my graduate school were enriched by the support from the US Army/Navy/NASA Vertical Lift Research Center of Excellence Cooperative Agreement, with Dr. Mahendra Bhagwat serving as the Program Manager and Technical Agent. Grant Number W911W6-21-2-0002 facilitated our research and allowed us to make valuable contributions to the field.

I would be remiss not to acknowledge the Nepalese community in Auburn. As an international student, the journey can be challenging, marked by homesickness and a longing for family. However, the warmth and camaraderie of the Nepalese community in Auburn provided a sense of belonging and made Auburn feel like a second home.

I would also like to thank the Bengali community for welcoming me into their world with open arms. Their inclusivity and the opportunity to partake in events and play football have made me feel cherished and special.

My gratitude extends to the friends I have made throughout my years at Auburn. Your companionship, support, and shared experiences have provided joy and solace.

Finally, I reserve my deepest appreciation for my wife, Sushmita Jha. This journey has demanded great strength and perseverance, and I have been fortunate to have you by my side,

providing unwavering support and love. Your presence has been my anchor throughout, and this dissertation is a testament to our shared dreams and aspirations.

I express my profound gratitude to all participating in this remarkable journey. Your contributions, support, and companionship have made this achievement possible and truly meaningful.

Table of Contents

List of Figures

List of Tables

Chapter 1

Introduction

Multi-rotor configurations, in general, have improved performance metrics, such as increased forward-flight speed, flight range, and payload, compared to single-main rotor (SMR) helicopters. As such, the application of multi-rotor helicopters or unmanned aerial systems in civilian and military scenarios and even for extra-planetary exploration has increased in recent years. Common multi-rotor configurations being developed include the counter-rotating coaxial rotor (CCR), tandem, side-by-side configurations for full-scale helicopters, and quad and coaxial rotor configurations at the smaller scales. Examples of full-scale multi-rotors are the V-22 Osprey (side-by-side configuration), CH-47 Chinook (tandem configuration), and Sikorsky S-97 (CCR), and Ingenuity, a CCR configuration that achieved the first extra-terrestrial flight on Mars.

While the multi-rotor configurations find their applications in an ever-increasing range of fields, our understanding of the interactional aerodynamics associated with the multiple rotors is not well developed. Through experiments across different parametric spaces, this thesis will study the effects of different aerodynamic interactions, such as rotor-on-rotor, blade-on-blade, and rotor-ground interactions prevalent in CCR configuration multi-rotors. This chapter gives an overview of counter-rotating coaxial rotors (CCR) and the aerodynamic interactions that influence their performance. It includes an in-depth literature review on these interactional effects, followed by the specific objectives of this dissertation and their underlying motivations.

1.1 Single main rotor configuration helicopters

Helicopters offer a unique advantage with their ability to hover, making them distinct from fixed-wing aircraft. Most helicopters today utilize a single main rotor for vertical take-off and landing (VTOL) and hovering capabilities. A tail rotor is employed to balance the torque generated by the main rotor. Igor Sikorsky is credited with pioneering these Single Main Rotor (SMR) configurations, with the Vought-Sikorsky VS-300 achieving its first successful free flight on May 13th, 1940 [12]. This groundbreaking achievement marked the first instance of a helicopter using a single main rotor for thrust generation and a tail rotor for yaw control. Subsequently, the SMR configuration has been widely adopted in the helicopter industry. Prominent contemporary examples of SMR helicopters include the Sikorsky UH-60 Black Hawk and the Boeing AH-64 Apache, as shown in Fig. 1.1.

(a) Sikorsky UH-60 Black Hawk

(b) Boeing AH-64 Apache

Figure 1.1: Examples of single rotor configuration helicopters [1, 2].

Although SMR helicopters have proven successful in various applications, these configurations face limitations in meeting the growing demands for increased speed, range, and payload capacity. Aerodynamic challenges such as *retreating blade stall* and *compressibility* effects constrain the operational capabilities of SMR helicopters. For example, during forward flight, the dynamic pressure on the advancing side of the rotor blades is significantly higher than on the retreating side. This pressure differential can lead to a rolling moment. To counteract this effect, the angles of attack on the advancing side are reduced, while those on the

retreating side are increased. Consequently, the retreating side may experience a stall, while the advancing side encounters high compressibility effects. These factors limit the maximum forward flight speed attainable by SMR helicopters. Payload capacity is also restricted by the size of the main rotor, often necessitating an expanded physical footprint to enhance payload capabilities. These limitations have ignited a renewed interest in multi-rotor configuration helicopters, which have the potential to extend the operational boundaries of modern helicopters further.

1.2 Counter rotating coaxial rotors

Counter-rotating coaxial rotors (CCR) represent an innovative rotor configuration with two main rotors mounted on a single shaft, rotating in opposite directions. This design eliminates the need for a tail rotor to counter the main rotor torque. Consequently, the power that would otherwise be consumed for torque balance in single-rotor configurations can be redirected to generate additional lift and/or propulsion. This increased thrust capacity translates to higher payload capabilities, all within a physical footprint similar to that of single-rotor helicopters. Moreover, in place of a tail rotor, CCR helicopters incorporate a pusher propeller, enhancing their forward flight speed compared to their single-rotor counterparts. In CCR setups, the advancing blades on both sides of the vehicle bear the primary thrust load, reducing the thrust requirements on the retreating blade side. This mitigates the risk of retreating blade stall, allowing CCR vehicles to maintain their lifting capabilities even at high forward speeds.

The presence of two main rotors contributing to thrust production also results in greater payload capacities within a footprint similar to that of single-main rotor (SMR) configuration vehicles. Despite these advantages, two rotors on a single shaft can introduce mechanical complexities, partly explaining why SMR configurations gained popularity in the early 1940s.

Numerous attempts were made before the 1950s to develop aerial vehicles using CCR configurations. However, the concurrent popularity of SMR helicopters and limited technological advancements to create two rotating main rotors on a single shaft hindered the progress of CCR helicopter development. The first successful flight for CCR in the USA was achieved in 1944 by Stanlet Hiller, Jr., just at the age of 19. He built XH-44 (refer to Fig. 1.2a), the first

helicopter to fly with all-metal rigid blades. Nevertheless, Hiller's full-scale CCR designs did not gain widespread acceptance [3].

A significant breakthrough in CCR configuration development came with the introduction of the Advancing Blade Concept (ABC) rotor system by the U.S. Army and NASA in 1964. This system featured two counter-rotating coaxial rotors with rigid blades measuring 12 meters in diameter. In 1970, extensive wind tunnel tests at NASA Ames were conducted across different advance ratios, highlighting the advantages of CCR in forward flight. Consequently, in December 1971, the U.S. Army contracted Sikorsky Aircraft to design, fabricate, and fly the XH-59A. This effort aimed to showcase the capabilities of the CCR design and assess its handling and maneuvering characteristics. The XH-59A program encountered setbacks, including serious damage during the first flight, unrelated to the ABC concept. However, the second flight achieved over 100 hours of flight time and set a speed record of 238 knots [13]. Despite these achievements, the presence of rigid blades led to a high moment transfer at the hub, resulting in increased vibrations within the vehicle. Ultimately, the program was discontinued in 1981.

In recent years, Sikorsky rekindled interest in CCR configuration, taking it to new heights by introducing the X2 Technology Demonstrator (X2TD), as depicted in Fig. 1.2b. Building on the legacy of the XH-59A, the X2TD incorporated active vibration control technology to address the vibration issues that plagued its predecessor. In 2008, the X2TD made its first flight and eventually broke records by reaching a speed of 250 knots. Drawing from the X2TD's success, Sikorsky developed the S-97 Raider and SB$>$1 DEFIANT helicopters, illustrated in Fig. 1.2c and d, respectively. These cutting-edge helicopters were built to compete for contracts in the U.S. Army's Future Aircraft Reconnaissance Aircraft (FARA) and Future Long-Range Assault Aircraft (FLRAA) programs, both integral components of the broader Future Vertical Lift (FVL) initiative launched by the U.S. Department of Defense (DOD) in 2009. The FVL program aims to replace the existing helicopter fleet with state-of-the-art Vertical Take-Off and Landing (VTOL) aircraft.

The advances achieved in CCR configuration helicopters and the successful demonstrations of their capabilities have reinvigorated interest in CCR designs across industrial and research communities. Furthermore, CCR configurations have found applications in Unmanned

(a) XH-44, 1944

(b) X2 Technology demonstrator, 2008

(c) S-97 Raider, 2015

(d) SB>1 DEFIANT, 2019

Figure 1.2: Evolution of counter-rotating coaxial rotors over the years [3, 1].

(a) DARPA TERN

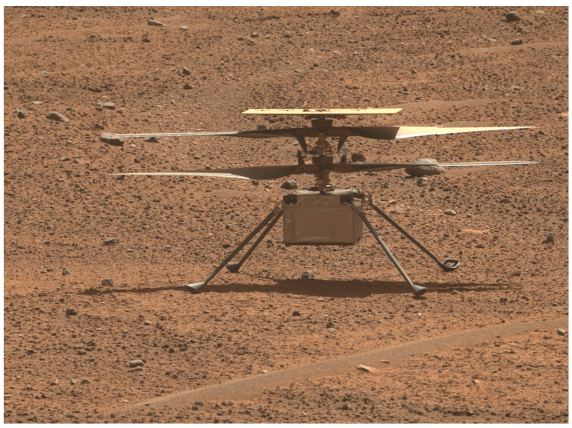

(b) Ingenuity

Figure 1.3: Examples of unmanned aerial vehicles with counter-rotating coaxial rotor configuration [4].

Aerial Vehicles (UAVs), such as the DARPA TERN (refer to Fig. 1.3a), designed for launch from littoral combat ships. In particular, Mars helicopter ingenuity (refer to Fig. 1.3b) adopted

a CCR configuration and achieved a groundbreaking feat as the first aircraft to perform powered, controlled flight on an extraterrestrial planet. Since its maiden flight on April 19, 2021, Ingenuity has completed an impressive 58 flights, totaling 104.2 flying minutes, far surpassing its initial goal of just five successful flights. This accomplishment marks a historic milestone in aerospace exploration.

1.2.1 Aerodynamic interactions

The combination of multiple rotors in CCR provides distinct advantages over its SMR configuration counterparts. As a result, the application of CCR has increased drastically, as illustrated in the previous section. However, the coaxial arrangement of two counter-rotating rotors also leads to high aerodynamic interactions, which dictate the performance characteristics of these vehicles. Some common interactions that persist in CCR configurations are **rotor-on-rotor, blade-on-blade, and blade-vortex interactions**. When the CCR rotors operate near the ground, interactions between the rotors and the ground plane also exist, which is categorized as **rotor-ground interactions**. These interactions are illustrated in Fig. 1.4.

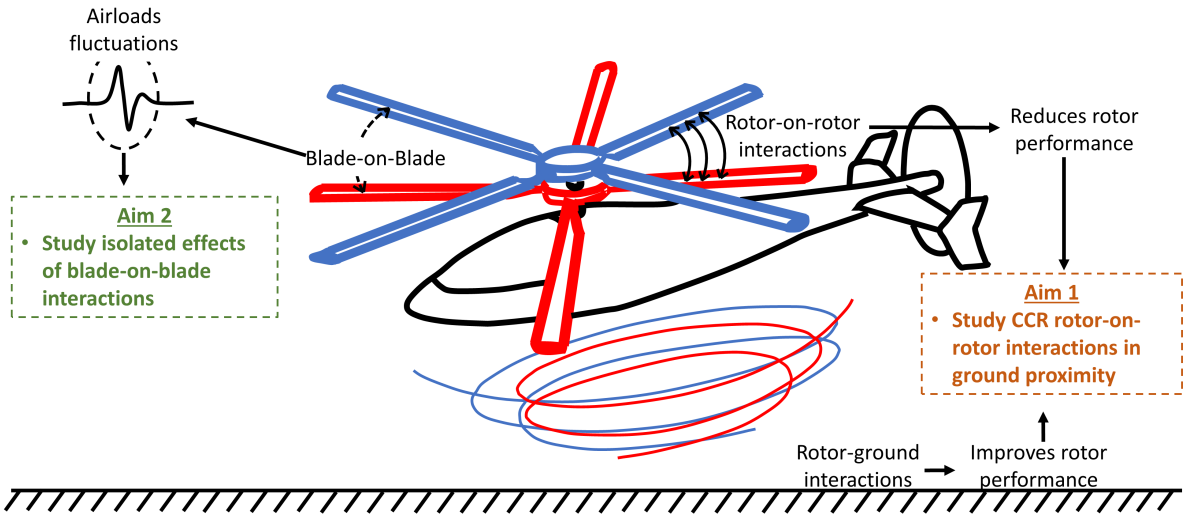

Figure 1.4: Summary of interactional aerodynamic effects in the counter-rotating coaxial rotor configuration in hover; helicopter schematic adapted from [5] and modified

Rotor-on-rotor interactions arise from the interplay between the upper and lower rotors, primarily driven by the effects of tip vortices and the bound circulation generated by the rotor blades. As both rotors rotate, helical tip vortex structures form at the rotor tips due to finite wing effects, and these vortices convect downwards along with the rotor's wake. These helical

vortex structures induce an inflow onto the rotors from which they originate, a phenomenon known as *self-induced inflow*. Furthermore, the tip vortices generated by one rotor in a CCR configuration also influence the other, introducing an inflow onto the second rotor. Therefore, both rotors experience induced effects from each other, as well as self-induced effects. Additionally, the lower rotor in a CCR configuration operates within the wake of the upper rotor. This combination of interactions, involving induced and inflow effects from both the adjacent rotor and its tip vortices, collectively diminishes the performance of the upper and lower rotors compared to their performance in isolated single rotor configuration[1]. These intricate interactional effects are collectively referred to as rotor-on-rotor interactions.

Rotor-on-rotor interactions dictate the steady-state characteristics of the CCR, but the unsteady interactions are also prevalent. Blade-vortex and blade-on-blade interactions are the two common sources of unsteadiness in the CCR. Blade-vortex interactions result from the interactions between the tip vortices and the blade. In SMR configuration helicopters, blade-vortex interactions are commonly observed during forward flight conditions and moderate to high advance ratios. However, the blade-vortex interactions are observed even in hover conditions for CCR due to the wake impingement of the upper rotor onto the lower rotor. These interactions can add vibratory loads on the rotor blades and hubs. In addition to the blade-vortex interactions, blade-on-blade interactions are also prevalent in CCR. Blade-on-blade interactions on CCR result from blade crossover events between the upper and lower rotor blades. As the two rotors rotate in opposite directions in CCR, the upper and lower rotor blades' bound circulation induces upwash and downwash onto each other, resulting in excursions in their loads. These interactions are periodic in nature and are a major source of vibrations.

When rotors operate in in-ground effect (IGE) conditions, their performance is influenced by the aerodynamic interactions with the ground plane. In IGE, several additional aerodynamic effects come into play. Firstly, the rotor wake is deflected horizontally after impinging onto the ground plane, resulting in a rotor outwash. Due to the wake impingement, the inflow velocity distribution on the rotor plane is modified, resulting in a change in rotor characteristics.

[1]Even though the individual rotors in CCR have degraded performance compared to its isolated counterpart, CCR as a whole still performs better when compared to isolated single rotor with same solidity, i.e., with twice the number of blades.

Additionally, the wake expansion in IGE causes the axial spacing between the helical vortex structures in the near wake to increase. This increase in vortex spacing reduces the induced effects on the rotor plane. Consequently, the rotor's performance is improved when operating near the ground, allowing the rotors to produce higher thrust for the same given torque.

In the context of CCR in IGE, ground effects enhance the performance of the upper and lower rotors. However, rotor-on-rotor interactions, which are inherent to CCR configurations, can simultaneously reduce the performance of both rotors. Depending on the proximity to the ground plane, the rotor-on-rotor interactions or the rotor-ground interactions may dominate the overall CCR performance characteristics. Moreover, it's important to note that the effects of blade-vortex interactions and blade-on-blade interactions can be amplified in IGE conditions due to the improved performance of the individual rotors. Since the rotors produce higher thrust for the same torque in IGE, the shed tip vortices could be stronger due to increased blade-bound circulation. Consequently, the severity of blade-vortex interactions in IGE may also increase. Furthermore, the increased blade-bound circulation in IGE can lead to larger load excursions during blade-on-blade interactions, resulting in higher vibratory loads.

1.3 Literature review

The influence of rotor-on-rotor interactions on the CCR performance has been well characterized, with the blade-vortex interactional effects also extensively studied in the context of SMR configurations. However, only a few studies focused on studying the blade-on-blade interactional effects. The performance characteristics of CCR in in-ground effect (IGE) conditions have also been limited. As such, this dissertation studies the effects of rotor-on-rotor interactions in the proximity of the ground plane and the blade-on-blade interaction. This section presents a comprehensive summary of the literature review on the aerodynamic interactions of the CCR rotors in hover and some outstanding scientific questions that still need to be answered.

1.3.1 Rotor-on-rotor interactions

The first reported CCR study in the public domain was by Taylor [14], where a Balsa dust technique was used to visualize the flowfield of a model-scale CCR system. Taylor observed

no unsteady interactions between the upper and lower rotor tip vortices in out-of-ground effect (OGE) conditions for a fixed value of axial rotor separation of 35% of the rotor radius. This was followed by an investigation of the performance of a full-scale CCR in out-of-ground conditions [15]. In this investigation, the performance characteristics of a four-bladed CCR rotor were compared with those of a two-bladed single rotor. The performance characteristics were also compared with that from the rotor-hovering theory [16] to explore if the momentum theories for a single rotor are adequate to predict the performance characteristics of CCR. He concluded that for the tested range of rotor spacing of (16-19%) of the rotor radius, the CCR performance can be predicted with the same level of accuracy as that of a single rotor by assuming CCR as a single rotor of equal solidity.

Besides these two seminal investigations, there were a few more studies [17, 18, 19, 20, 21] on CCR, scattered in the later part of the 20th century, as summarized in a detailed review by Coleman [22]. The introduction of the Advancing Blade Rotor (ABC) by the U.S. Army and NASA in the 1960s resulted in numerous small and large-scale wind tunnel testing of CCR rotors. Cheney [23] provides a detailed summary of these test results. From the small-scale tests, it was inferred that there was a beneficial effect on the total CCR performance, and it was postulated that the swirl recovery could be the attributing factor. It was also concluded that the spacing did not significantly impact the rotor performance for the tested range of 14% and 20% of the rotor radius. The full-scale wind tunnel testing of XH-59A also showed that the CCR rotor had performance benefits compared to the single rotor with equivalent solidity [17].

Nagashima [24] performed flow visualization to study the tip vortex characteristics of CCR and compared that with a single rotor of an equivalent solidity. The tip vortex trajectory for a single rotor followed a close trend with that suggested by Landgrebe [25]. However, the tip vortices from the upper and lower rotor in the CCR configuration convected at higher velocities than Landgrebe's model. The collective pitch of the lower rotor was also varied to study its effects in the wake. The change in the lower rotor collective was observed to have significant effects on the wake structures. The optimal settings for the lower rotor collective were determined to be where the tip vortices from the upper and lower rotor were evenly spaced and did not interact. It was also theorized that these optimal conditions based on the flow field

characteristics would correspond to the yaw-trimmed conditions, but this theory was never tested.

In the late 1950s, a few lower-order models were also developed to predict the CCR performance, and the one proposed by Nagashima and Nakanshi [20] was particularly interesting. Here, the actuator disk and free wake analysis were used to model the rotor wakes and their effects on rotor performance. The interesting aspect of this work was modeling the mutual interactions between the upper and lower rotors by considering the axial velocities induced by the two rotors onto each other. These interference factors were a function of the axial spacing between the rotors. Analysis of these interference factors showed that the interactions between the two rotors decreased with increasing rotor spacing. Although these studies in the 20^{th} century highlighted key features of the CCR rotors, important questions regarding the flow physics behind the aerodynamic interactions between the rotors remained to be investigated.

It was only until the recent renewed interest in CCR that more research was conducted to understand the influence of CCR aerodynamic interactions on its performance at different conditions. Recent aerodynamic studies explored the effects of rotor-on-rotor interactions on CCR through experimental studies where parameters such as the rotor spacing, blade planform, thrust conditions, etc. were varied [26, 6, 27]. All of these studies showed that the upper rotor outperformed the lower rotor. This is expected since the lower rotor operates in the wake of the upper rotor, which results in higher inflow velocities (U_P) (refer to Fig. 1.5) on the inboard portion of the lower rotor. Consequently, the lower rotor sectional effective angle of attack (α) (refer to Fig. 1.5) reduces, resulting in reduced rotor performance.

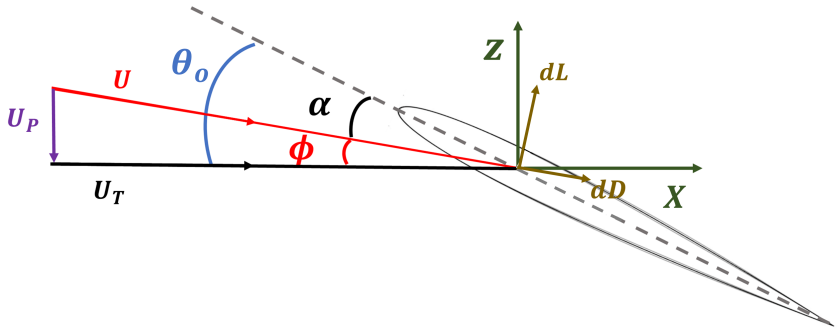

Figure 1.5: Schematic representation of an airfoil section

Likewise, the rotor spacing also significantly impacted the individual rotors, with the upper rotor exhibiting reduced performance and the lower rotor exhibiting improved performance at smaller rotor spacing [26, 6, 27]. As the rotor spacing reduced, the lower rotor imparted higher inflow onto the upper rotor, reducing its performance and decreasing the wake impingement onto the lower rotor. As a result, the lower rotor experienced reduced inflow (and a corresponding increase in the effective angle of attack (α)), which improved its performance at smaller rotor spacing [6]. Figure 1.6 shows the variation in the performance of the CCR and its rotors with respect to rotor spacing at two thrust conditions. As discussed, the performance of the upper rotor degraded while the lower rotor improved with the reduction in the rotor spacing. In summary, these studies showed that the rotor-on-rotor interactions degrade the performance of the individual rotors in CCR configuration compared to an isolated rotor operating under similar conditions.

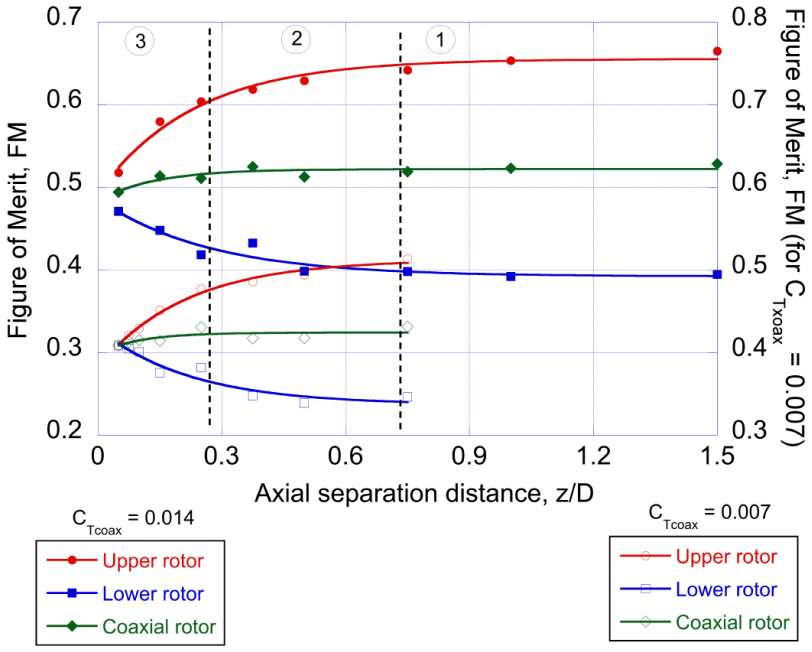

Figure 1.6: Variation in the performance of CCR and its rotors with respect to rotor spacing for different thrust conditions. The figure is taken from a study by Ramasamy [6].

Additional flowfield studies of the CCR elucidated important near-wake characteristics, corroborating the above-mentioned observations from the performance studies. Mortimer [28] showed that the upper rotor tip vortices exhibited higher convection velocities and wake contraction compared to the lower rotor tip vortices, which agreed with the observations made by

Silwal [29]. Consequently, the upper rotor exhibited improved performance as the self-induced inflow was reduced due to increased vortex spacing. Silwal [29] also compared the inflow velocity of the upper rotor in the CCR configuration with that of a single rotor producing the same thrust. The comparison was carried out at different rotor spacing. They observed that for a given thrust, the inflow distribution for the upper rotor was higher than that compared with the single rotor. The upper rotor at minimum rotor spacing tested also had the highest integrated inflow. These results suggest that the torque required to produce the same thrust for the upper rotor is higher than that of the single rotor. The torque requirement also increases with the reduction of the rotor spacing. These observations corroborate with the performance measurements made by Ramasamy [6].

Numerous studies have also focused on characterizing the tip vortex interactions in the near-wake of CCR. These investigations have yielded intriguing findings. Shukla [30] showed that the tip vortices generated by the lower rotor exhibited two distinct trajectories in the CCR near-wake, possibly due to the vortex interactions in the CCR near-wake. The characteristics of these vortex interactions have been studied in detail by Konus [31], where different types of long-wave vortex instabilities were identified.

In addition to experimental investigations, lower-order models have been developed to accurately predict the performance of Counter-Rotating Coaxial Rotor (CCR) configurations. These models include Blade Element Momentum Theory, Free Vortex, and Prescribed Wake models, among others [32, 33, 34, 35, 8]. Leishman [36] introduced a lower-order model based on Blade Element Momentum Theory. It assumed the upper and lower rotors were adequately spaced apart for the upper rotor wake to fully develop before reaching the lower rotor. Additionally, it considered that the lower rotor's performance did not influence the upper rotor. Landgrebe's model [25] was incorporated to account for wake contraction, determining the radial location in the lower rotor where the upper rotor's wake impinges. The model's results were compared to experimental data from Harrington's analysis [15], demonstrating a favorable agreement. However, it's important to note that this model's assumptions may not be universally valid, particularly in cases where the lower rotor significantly affects the upper rotor's performance.

Lee [37] modified Leishman's model to address non-linear interactions between the upper and lower rotors. This modification introduced interference factors and coefficients to account for these complex interactions. The results were compared with the experimental data by Ramasamy [6], and constant coefficients were introduced to match the experimental results. However, the fundamental understanding behind these coefficients remained elusive. These model development efforts underscore the intricate nature of aerodynamic interactions in CCR configurations. They emphasize the need for continued measurements and research to understand the underlying physics, ultimately enhancing the predictive capabilities of these models.

1.3.2 Rotor-ground interactions

The previous section delved into the intricate aerodynamic interactions between the upper and lower rotors in the CCR configuration. However, these interactions can evolve when the CCR operates close to the ground, adding another layer of complexity to its performance. Unlike the CCR, SMR performance near the ground has been extensively studied, while the CCR's performance in In-Ground Effect (IGE) conditions has received less attention.

In SMR IGE studies, experiments are typically conducted under either fixed-collective (untrimmed) [38] or constant-thrust (trimmed) [39, 7] conditions. In fixed-collective experiments, the collective pitch of the rotor blades remains constant while the rotor's height above the ground is gradually reduced. As the rotor gets closer to the ground, the thrust it generates increases significantly, a phenomenon well-documented in the literature across various rotor parameters and sizes [38, 40, 41, 42]. This thrust augmentation, as seen in Fig.1.7, occurs because of reduced inflow due to the proximity of the ground, leading to a higher effective angle of attack (α) for a fixed collective pitch ($\theta_\circ$) (see Fig.1.5).

Compared to fixed-collective experiments, constant-thrust experiments involve trimming the collective pitch of the rotor blades to maintain a constant thrust while varying the rotor's height. As the ground effect results in reduced rotor inflow, the collective pitch of the rotors is reduced to maintain constant thrust at lower rotor heights. Thus, the power requirement for producing the same thrust reduces with the reduction in rotor height, which has also been well reported in the literature [39, 7]. For both fixed collective and constant thrust experiments,

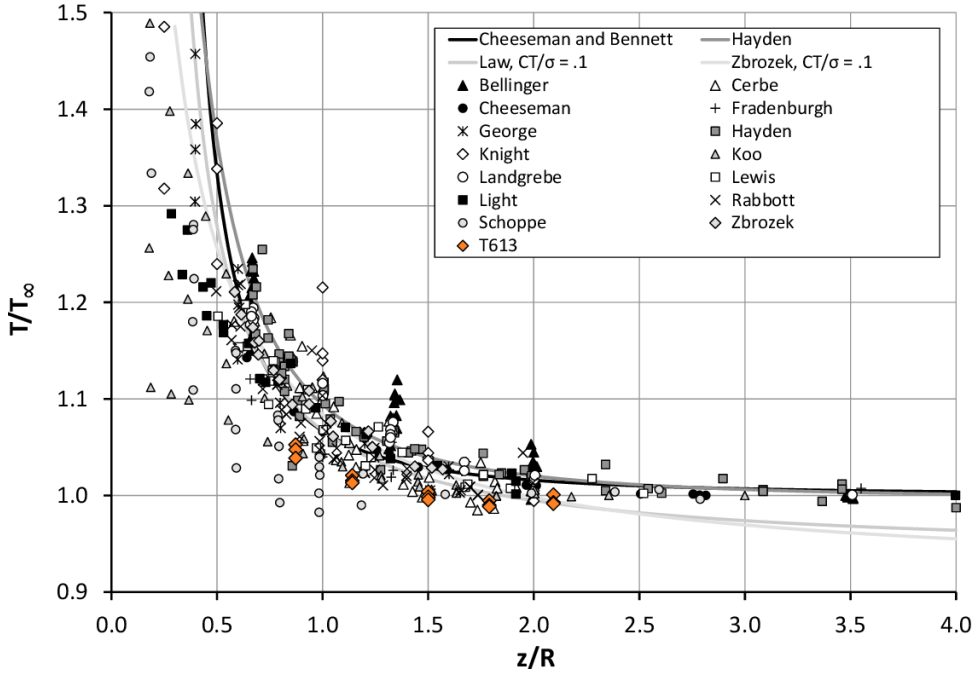

Figure 1.7: Summary of thrust augmentation with the reduction in rotor height observed across different studies. The figure is taken from a study by Tanner [7]

the performance of a single rotor typically improves as it gets closer to the ground due to reduced induced inflow resulting from ground proximity. Various models have been introduced to predict the performance changes in Coaxial Counter-Rotating (CCR) rotor systems in In-Ground Effect (IGE) conditions.

Cheeseman [43] suggested the following equation to predict the thrust augmentation on the single rotor when in IGE:

$$\frac{T_{IGE}}{T_{OGE}} = \frac{1}{1 - 15(R/z)^2} \tag{1.1}$$

where T_{IGE} is the rotor thrust in IGE conditions, T_∞ is the rotor thrust in out-of-ground conditions (OGE), R is the rotor radius, and Z is the rotor distance from the ground plane. This equation was based on the methods of image analysis carried out by Betz [44], where he considered the rotor to be the source and the image a sink. However, the results from this analysis resulted in a decrease in rotor thrust with a reduction in the rotor height. This was due to the additional inflow induced by the image sink. Cheeseman [43] modified this approach with both the rotor and the image considered as a source, reducing the rotor inflow and increasing rotor thrust while reducing rotor heights.

The model proposed by Cheeseman [43] provided a good first-order estimate of the rotor performance in IGE but tended to overpredict the performance. As such, Hayden [45] added empirical corrections to this model, and the equation is given as:

$$\frac{T_{IGE}}{T_{OGE}} = A + 2B\left(\frac{1}{z/R}\right)^2 \tag{1.2}$$

where A and B are empirical constants with values $A = 0.9926$, and $B = 0.039$. This model provided an overall better estimation of the rotor performance in IGE, as seen in Fig. 1.7.

In addition to the performance, flowfield characteristics of SMR in In-Ground Effect (IGE) conditions have been extensively studied, providing valuable insights into rotor performance and wake behavior near the ground. Light [41] conducted flow visualization experiments and observed that the spacing between the helical vortex structures for SMRs in IGE increases compared to those in OGE conditions. This change directly affects the induced effects at the rotor plane, influencing rotor performance.

Rauleder [46, 47] conducted comprehensive studies to better characterize the rotor wake and outwash characteristics of SMRs to understand their role in brownout phenomena. Rauleder measured turbulence intensity and shear stress distribution in the wake to quantify their contributions to particle upliftment and entrainment in the flow. His observations suggested a significant change in turbulence intensity due to entrained particles in the wake, indicating a two-way coupling between the rotor wake and entrained particles. This finding challenged existing models that did not account for such two-way coupling and emphasized the need for more accurate predictions of brownout phenomena.

The outwash generated by rotor wakes, especially in IGE conditions, has been the subject of extensive study for SMR [7, 48] and multi-rotor configurations like tandem rotors [49, 50]. This research is crucial due to the safety and environmental concerns of the high outwash velocities. Peak outwash velocities for single rotors in IGE conditions have been reported to reach values as high as 150% of the mean rotor velocity, posing significant safety risks for ground personnel [49]. For instance, Schane [51] reported that different rotor configurations

with varying disk loadings could result in peak outwash velocities of up to $28m/s$ for a CH-47A configuration with a disk loading of $289N/m^2$. Such high velocities are hazardous to personnel on the ground and can damage the surrounding environment and structures.

To mitigate these risks, Mehrabi [50] suggested a safe operating distance of three rotor radii from the vehicle for the ground crew. Ramasamy [49] found that for tandem rotor configurations, the outwash displayed self-similar characteristics beyond a radial distance of one rotor diameter away from the rotor tip. Understanding and controlling outwash behavior is essential for improving the safety of rotorcraft operations in IGE conditions.

While the performance and flowfield characteristics of the SMR and some multi-rotor configurations like tandem rotors have been studied extensively, the CCR performance and flowfield characteristics remain uninvestigated. The CCR performance is expected to show improvement similar to that of SMR due to ground effects. However, the behavior could be different because of rotor-on-rotor interaction effects. The rotor-on-rotor interactions could act to negate some of the benefits of the ground plane. On the contrary, the ground effect could also overcome the rotor-on-rotor interactional effects and improve the performance characteristics of the individual rotors.

The only work that has attempted to understand the performance of CCR in IGE was by McAlister [26]. In this study, the torque of the upper and lower rotor was matched by changing the lower rotor collective pitch while that of the upper rotor was kept constant. The total thrust of the system was observed to increase with reducing rotor height. The thrust produced by the upper and lower rotor was also observed to increase, but the rate of increase was larger for the lower rotor. But as the total thrust of the coaxial rotor system was allowed to vary with change in rotor height, the aerodynamic environment that the rotors are subjected to also changes and insights regarding the influence of interactions between the upper and lower rotor on CCR IGE performance cannot be gained.

Thus, there is a need to conduct a comprehensive study of the CCR performance in IGE to understand the influence of two opposing effects, rotor-on-rotor and rotor-ground interactions, on CCR performance. As the rotor-on-rotor interactions result in degrading rotor performance, some of the benefits due to ground proximity could be negated, which needs to be quantified.

Understanding these interactional effects can help predict the outwash characteristics, which have implications for the safety of the ground crew and the brownout phenomenon. Studying the physics of the aerodynamic interactions of CCR in IGE can also assist in formulating a lower-order modeling approach such as those for SMR [43, 45].

1.3.3 Blade-on-blade interactions

The literature review so far has presented the influence of rotor-on-rotor interactions on CCR performance, providing insight into its steady-state characteristics. However, blade-on-blade interactions are also dominant in the multi-rotor configurations, which can be a primary source of unsteadiness. These interactions result from interactions between the blades of the two rotors. For example, blade-on-blade interactions are observed in co-rotating coaxial rotor configurations, where the interaction between the bound circulation and wake from the two blades can significantly impact rotor airloads and acoustics [52, 53]. Parameters such as the index angle (azimuthal spacing) between the upper and lower rotors and axial spacing have been found to have a substantial influence on rotor performance [52, 53]. Uehara [52] conducted performance measurements on a model-scale co-rotating coaxial rotor and found that optimizing the index angle could enhance rotor hover performance. Similarly, Tinney investigated how a combination of rotor index angle, axial spacing, and rotor rotational speed affected rotor performance and acoustic signatures [53].

In CCR, the blade-on-blade interactions occur due to the blade crossover between the upper and lower rotor blades (refer to Fig. 1.8). These interactions are highly unsteady and induce transient changes in the rotor loads. This behavior has been reported in some of the experimental and numerical studies, which showed that the blade crossover had a significant influence on the rotor loads (thrust and torque) with observed transient excursions corresponding to the number of blade crossovers per revolution [54, 55, 56, 8, 35]. These transient effects can induce vibratory loads onto the CCR rotors and its hubs and alter its acoustic characteristics [57, 58]. Characterizing these vibratory loads on CCR blades and hubs is even more important as the blades are rigid, and rotor hubs are hinge-less to avoid collision between the blades.

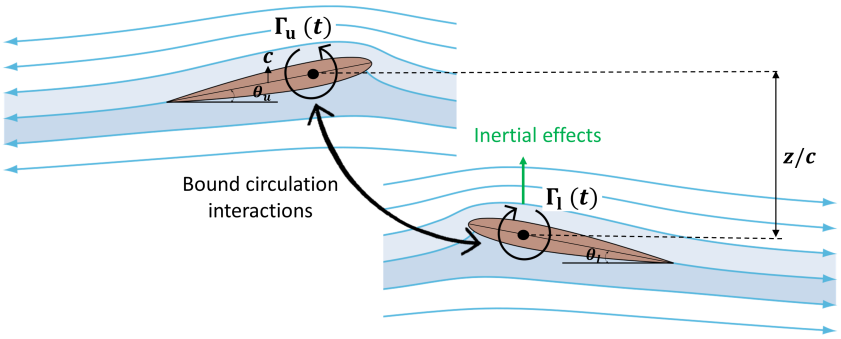

Figure 1.8: Schematic two-dimensional representation of the blade-on-blade interactions due to blade crossover

The experimental studies carried out so far have measured these transient loads at the rotor hub, which is an integrated effect of rotation, induced, and blade-on-blade interactions. Singh [56] conducted experiments in a Mach-scaled coaxial rotor thrust stand at UT Austin to measure the loads experienced by the rotors. Numerical simulations were also performed using RCAS and Helios to compare with the experimental data. As the rotors were two-bladed, the blades experienced four excursions per revolution due to the blade-on-blade interactions. In addition, peak-to-peak variations in the load measurements were observed when the experimental data were compared with the simulation results. These variations were attributed to the differences in the blades, which could be introduced due to manufacturing defects. Here, it was also shown that the magnitude of the transient loads measured at the blades during the blade crossover was less than that measured at the hub. This observation illustrates that the hub measurements are inadequate to understand the true effects of blade crossover on the blade loads. A translating wing facility is required because the blade measurements are challenging in a rotating thrust stand setup.

Uehara [55] hypothesized that the observed excursions during the blade crossover are due to the interaction between the bound circulation of the upper and lower rotor blades. As the blades approach each other, the bound circulation of the blades introduces upwash on each other, increasing the blades' effective angle of attack. As a result, the sectional lift increases, increasing the rotor thrust. Similarly, the bound circulation of the blades introduces downwash on each other after the blade crossover, resulting in a reduced effective angle of attack and, thus, reduced rotor thrust. After the blades are far apart, the blade-on-blade interactions reduce, and

the load excursions disappear. However, the parameters that influence these effects have not been quantified.

Lower-order models that account for the unsteadiness [59, 8] have been developed to study blade-on-blade interactions. Singh [8] developed a numerical framework using the viscous vortex particle method, simulated blade crossover, and studied the interactions. The results for the blade crossover of the NACA0012 airfoil section at a spacing of $1c$ at different pitch angles are shown in Fig. 1.9. At zero pitch angle, the upper airfoil experienced a positive increase in the lift. In contrast, the lower airfoil experienced a negative increase due to the airfoil curvature effects. At higher pitch angles, both the upper and lower airfoils showed a positive increase in their lift, with the increase higher for the upper airfoil. However, these models have not been validated using experimental data. As such, detailed studies are required to gain a fundamental understanding of the blade crossover effects. These experiments become even more critical at high-pitch angles where the flow separation can induce non-linear effects. At these conditions, existing hypotheses for most lower-order models, such as the satisfaction of the Kutta condition at the trailing edge, might not be valid [60].

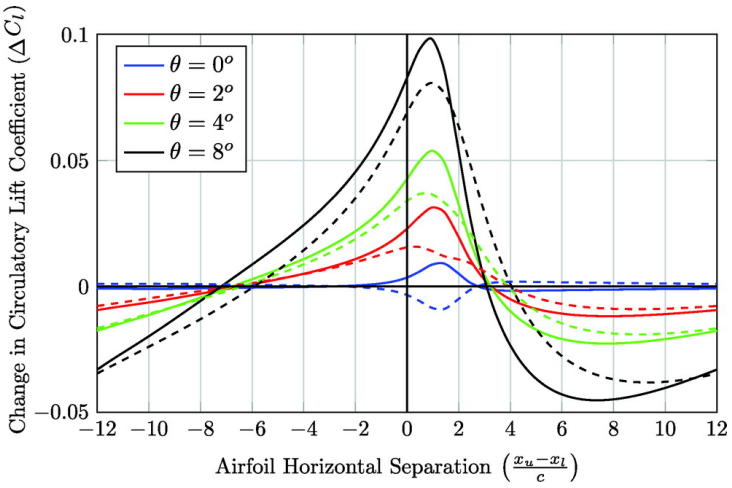

Figure 1.9: Effects of blade crossover on the airfoil lift at different angles of attack. The figure is taken from a study by Singh [8]. The solid lines represent the top blade, and the dashed lines represent the bottom blade.

An analogy can be made between the blade crossover event and the crossover event involving bluff bodies, such as trains. In a study by Ogawa [61], numerical simulations were conducted to examine the crossover effects between two trains. The simulations revealed that

as the trains approached each other, the pressure between them increased. During the crossover, a low-pressure region developed between the trains due to airflow acceleration. The pressure at the nose of the trains decreased as they passed each other. Following the crossover, the pressure at the nose of the train gradually returned to its pre-crossover values. These pressure fluctuations resulted in an increase in lift and a reduction in drag experienced by the trains. A similar flowfield evolution can be anticipated during the blade crossover event, although there may be differences because trains are inherently bluff bodies. The presence of bound circulation on streamlined bodies like airfoils can lead to variations in the evolution of the flowfield. However, such flowfield evolutions between airfoils have not been quantified under different operational conditions.

Insights into the expected effects of the blade crossover event can also be drawn from studies on interactions between lifting bodies and mutating ground conditions [9, 62, 63, 64]. For example, a study by Qu [9] involved numerical simulations investigating an airfoil's loads and flowfield characteristics in a mutating ground condition. The study observed that as the airfoil approached the step-rise edge of the ground plane, the lift initially increased due to upwash effects from the ground edge. As the airfoil entered the mutating ground plane, the lift decreased due to reduced upwash effects. Eventually, the lift increased again and settled steadily after the airfoil fully entered the static ground conditions. The flowfield evolution during these phases is shown in Fig. 1.10. While this provides some parallels, it's important to note that blade crossover is a coupled event where changes in loads on one blade affect the other. The detailed effects of these coupled interactions have not been extensively studied.

From this literature survey, it becomes clear that to study blade crossover, it's crucial to conduct measurements in an environment where these interactions can be isolated from other complex effects, such as three-dimensional and rotational effects. The experimental facility should be capable of measuring the loads and flowfield during the blade crossover event. Then, the problem's non-dimensional parameters must be established, followed by a parametric study to determine their impact. The contribution of the unsteady effects on the total excursions during the blade crossover also needs to be determined to augment the predicting capabilities

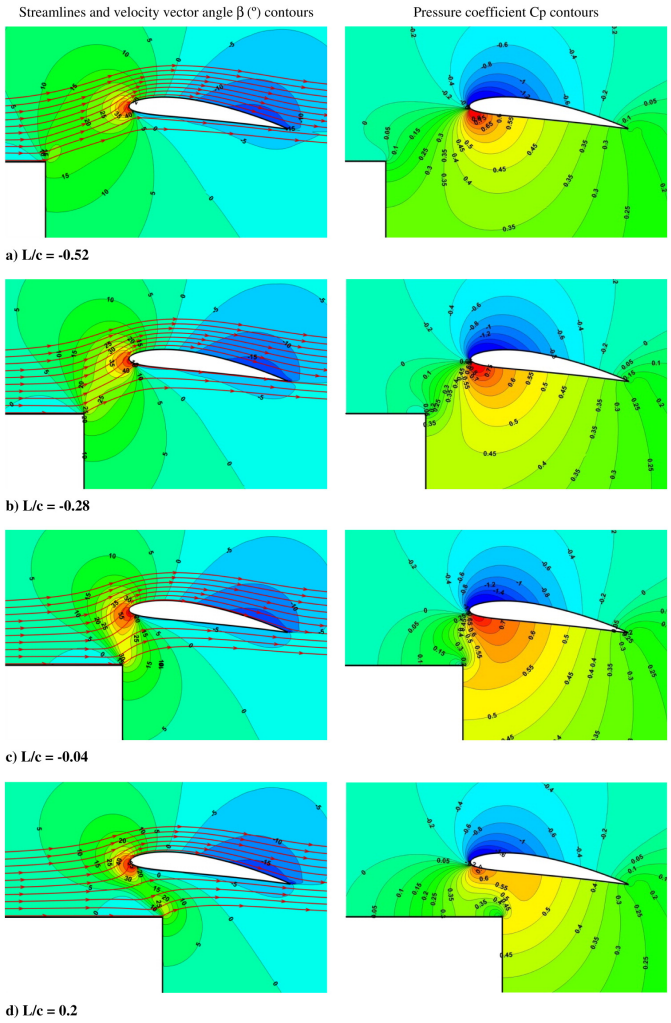

Figure 1.10: Streamlines, velocity vector angle contours, and pressure contours while landing onto a mutating ground. The figure is taken from a study by Qu [9].

of existing models. The effects of blade crossover at high angles of attack also need attention to study the non-linear effects due to flow separation.

1.3.4 Literature review summary

The summary of the current literature review is provided in Fig. 1.11. The literature review highlights the effects of rotor-on-rotor interaction on the performance of the CCR and its individual rotors in out-of-ground conditions (OGE) have been well-characterized. While the effects of blade-on-blade interactions have been reported in some studies, a fundamental understanding of the blade crossover effects on the rotor load still needs to be explored due to the associated experimental challenge of load measurements at the blade during rotor operation.

Similarly, the competitive effects of rotor-on-rotor and rotor-ground interactions on the CCR performance in IGE have not been explored. The key scientific questions that remain to be answered are as follows:

1. How will the CCR and its individual rotors behave when operating in ground proximity where rotor-on-rotor and rotor-ground interactional effects dominate?

2. What non-dimensional parameters dictate the load characteristics during the blade crossover?

3. What is the contribution of unsteadiness effects during the blade crossover event?

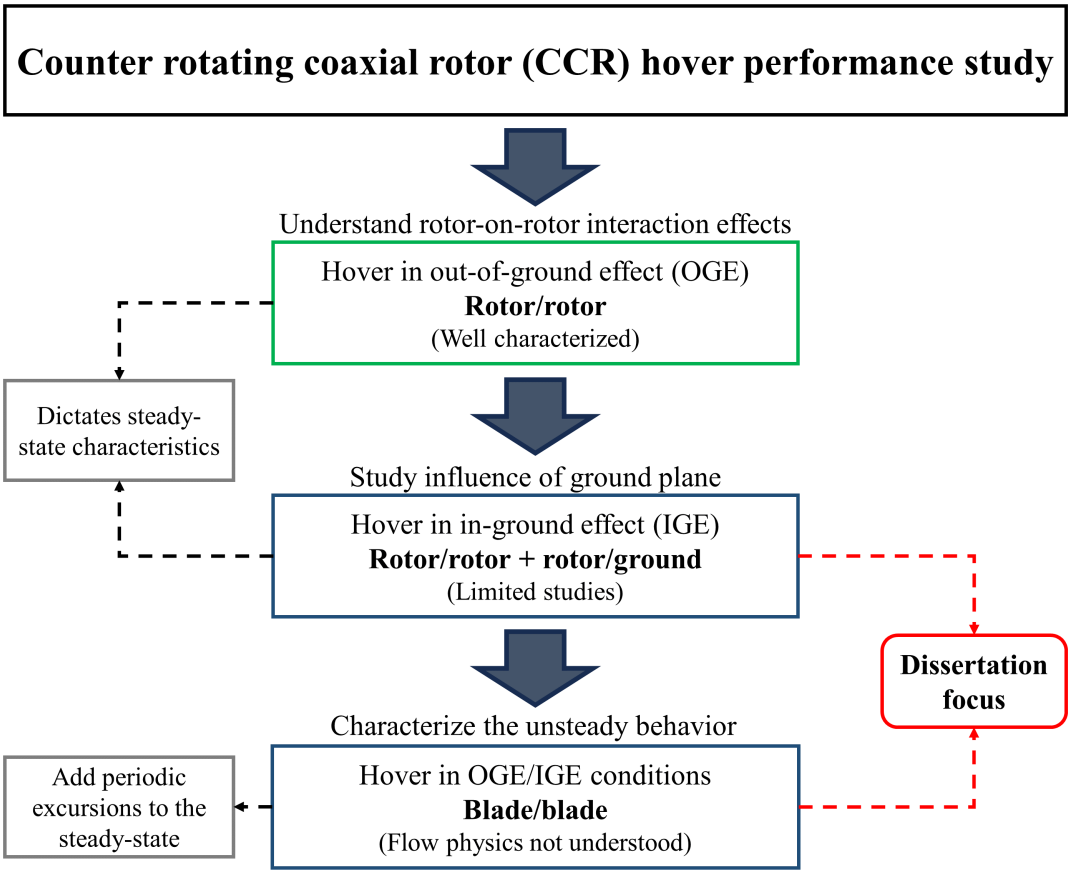

Figure 1.11: Summary of literature review

1.4 Motivation and objectives

The current dissertation will address the identified scientific questions through an experimental approach. The overall goal of this dissertation will be to study the effects of rotor-on-rotor,

rotor-ground, and blade-on-blade interactions on the performance and flowfield of the CCR and its individual rotors during hover. The motivation for conducting these studies is summarized below:

1. Understanding the CCR behavior in IGE is required to develop and validate lower-order predictive tools.

2. Characterizing the performance characteristics of individual rotors in CCR configurations during IGE is crucial, especially since yaw trimming relies on balancing torque between the upper and lower rotors. This knowledge can contribute to developing effective control strategies to prevent loss of vehicle control resulting from torque imbalances between the two rotors in ground effect.

3. Conducting a fundamental study on blade crossover effects is essential to comprehensively understanding the underlying flow physics. This knowledge will be crucial in enhancing the predictive capabilities of tools developed for the lower rotor.

To facilitate a systematic investigation of these aerodynamic interactions in CCR, the research plan for this dissertation is divided into two aims, which are discussed below:

1.4.1 Aim 1: Performance characteristics of counter-rotating coaxial rotors hovering in ground effect

The aerodynamic interactions between the rotors and the ground plane are highly non-linear, and the physics behind this phenomenon has not been understood. As such, the lower-order prediction tools do not account for the aerodynamic interactional effects. Thus, a fundamental understanding of the rotor-ground interactions is required to improve the efficacy of the available prediction tools. The experimental database for validating the computational models to predict the CCR performance behavior in IGE is also scarce. Aim 1 of this thesis focuses on understanding the physics behind the complex aerodynamic interactions between the CCR individual rotors and the ground plane through experimental measures. The data collected are also valuable for validating the current and future computational models. The specific objectives to achieve this goal are listed below:

Facility development and validation

1. Develop a thrust-scaled aerodynamic coaxial rotor thrust stand.
2. Establish baseline characteristics of the individual rotors in single rotor configuration under out-of-ground (OGE) conditions.
3. Conduct performance and flowfield measurement of CCR in OGE conditions to compare with literature.

CCR performance characterization in IGE conditions

1. Perform CCR IGE experiments at different rotor spacing and rotor heights.
2. Compare the performance of CCR and its individual rotors with a single rotor.
3. Assess the influence of ground proximity on the rotor-on-rotor interactions.

1.4.2 Aim 2: Quantify the influence of blade crossover on unsteady loading of counter-rotating coaxial rotors

The blade crossover event in CCR is a transient effect contributing to blade vibrations and modifications to the vehicle's acoustic signature. Studies on the blade crossover event have been scarce and are limited to a few numerical studies. Even so, the effects of different non-dimensional parameters on the blade passage effects have not been established. Additionally, the contribution of the unsteady effects during the blade crossover has not been determined. A fundamental understanding of these flow physics is required to develop accurate prediction tools. This will also be crucial for minimizing and/or modifying the CCR acoustic signatures. As such, Aim 2 of this dissertation focuses on studying the fundamental flow physics behind the blade crossover to augment our current understanding of the blade crossover effects. The specific objectives followed for achieving this goal are presented as follows:

Facility development and validation

1. Develop a hydrodynamic towing tank facility to measure loads and flowfield during the blade crossover event.

2. Validate the efficacy of the facility by conducting baseline performance and flowfield measurements for a single blade.

3. Compare the single-blade performance characteristics to existing literature.

Blade load characteristics during blade crossover

1. Establish the relevant non-dimensional parameters dictating the problem.

2. Conduct a parametric study to quantify the importance of the established non-dimensional parameters.

3. Perform flowfield measurements to quantify the contributions of the unsteady effects.

1.5 Framework

The objectives of this research were pursued through experimental means involving the construction of specialized facilities equipped with instrumentation for load and flowfield measurements. A detailed description of these facilities can be found in Chapter 2. The validation of the aerodynamic coaxial rotor thrust stand designed to achieve the first aim of this dissertation was presented in Chapter 3. Subsequently, Chapter 4 provided an in-depth discussion on the performance study of counter-rotating coaxial rotors (CCR) in in-ground effect (IGE) conditions using this thrust stand.

The dissertation's focus then shifted toward achieving the second aim, for which a hydrodynamic towing tank facility was employed. Chapter 5 is dedicated to validating this towing tank facility. Results and discussions related to blade crossover are extensively covered in Chapter 6. Finally, the last chapter, Chapter 7, summarizes key conclusions drawn from this dissertation, discusses their implications, and highlights directions for future work.

Chapter 2

Methodology

Aim 1 of this dissertation focuses on the performance characterization of counter-rotating coaxial rotor (CCR) in ground proximity. A static blade characterization rig and an aerodynamic coaxial rotor thrust stand were developed to conduct this study. Aim 2 of this dissertation focused on studying blade-on-blade interactions during blade crossover. A hydrodynamic towing tank facility was developed for Aim 2, and a control volume approach was used to analyze the results. The details of these facilities and techniques are described in this chapter.

2.1 Static blade characterization rig

This rig was developed to characterize the static performance of the blades used in the CCR performance study. The blade was untwisted with NACA0012 airfoil section, and the chord length was $0.036\ m$. It was mounted between two transparent end plates, as shown in Fig. 2.1. The distance between the end plate and the blade tip in the free end was maintained below $0.002m\ (\leq 0.05c)$ to avoid any tip effects. Two single-axis strain gauge-based loadcells with a capacity of $10N$ were used to measure lift and drag forces simultaneously. The loadcell signal was amplified using Tacuna amplifiers (EMBSGB200), and the data were acquired using an NI USB-6341.

Flow visualization was also carried out at the wing mid-span. The images were captured using a 4MP (Vision Research VEO 640S) camera. The system was placed inside an open circuit wind tunnel with 0.61m $\times$ 0.61m test section in the Aerodynamics Laboratory at Auburn University. The wind tunnel was operated at the speed of $20\ m/s$, which resulted in the Reynolds number of $Re = 46,000$. The speeds were limited to $20\ m/s$ for the current study as

the blades experienced structural vibrations when the airspeed was further increased inside the test section. The air velocity inside the test section was calculated by measuring static pressures at the wind tunnel settling chamber and the test section. Bernoulli's equation was then used to calculate the air velocity in the test section.

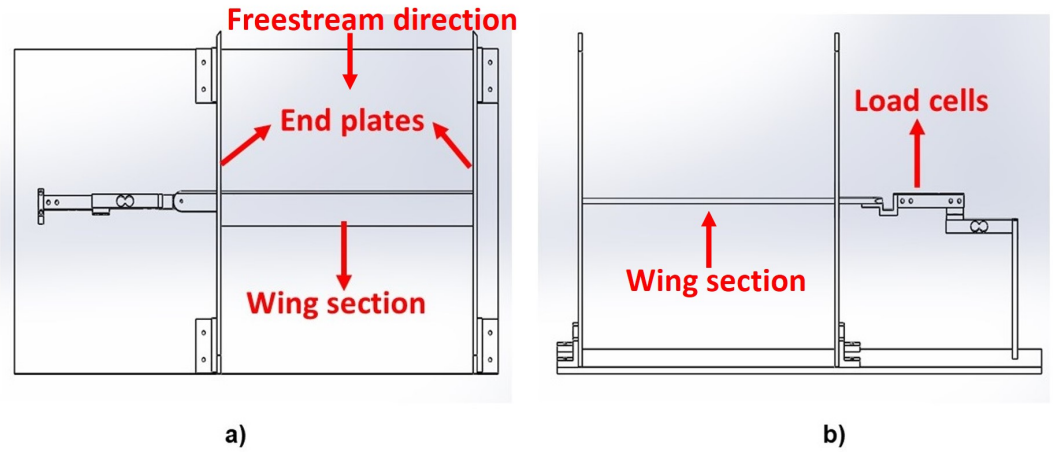

Figure 2.1: Schematic representation of the static blade characterization rig, a)Front view, b)Top view

2.2 Aerodynamic coaxial rotor thrust stand

The aerodynamic coaxial rotor thrust stand was developed to be modular and easily configurable to transition between different multi-rotor configurations, as shown in Fig. 2.2. The thrust stand was designed over a robust and rigid base frame and was reinforced with additional struts to ensure high stability across different operational parameters. The continuous adjustment of the axial (d) and lateral (d_r) separation distance between the rotor centers was ensured through vertical and horizontal t-slotted aluminum frames (Fig. 2.2b). The current full-scale, operational coaxial rotorcrafts have axial separation distance between $0.1 \leq d/R \leq 0.2$ ([6]) and the lateral separation distance (d) between the rotors for the full-scale operational side-by-side rotor is $d_r/R \sim 2.4$ [65]. Thus, the current thrust stand is designed to be configured in this range.

The thrust stand consisted of two identical rotors mounted at the end of a cantilevered t-slotted framing. The cantilevered beam was further reinforced (Fig. 2.2a) to reduce the degrees of freedom and avoid any vibration during operations. In addition, the rotors were placed

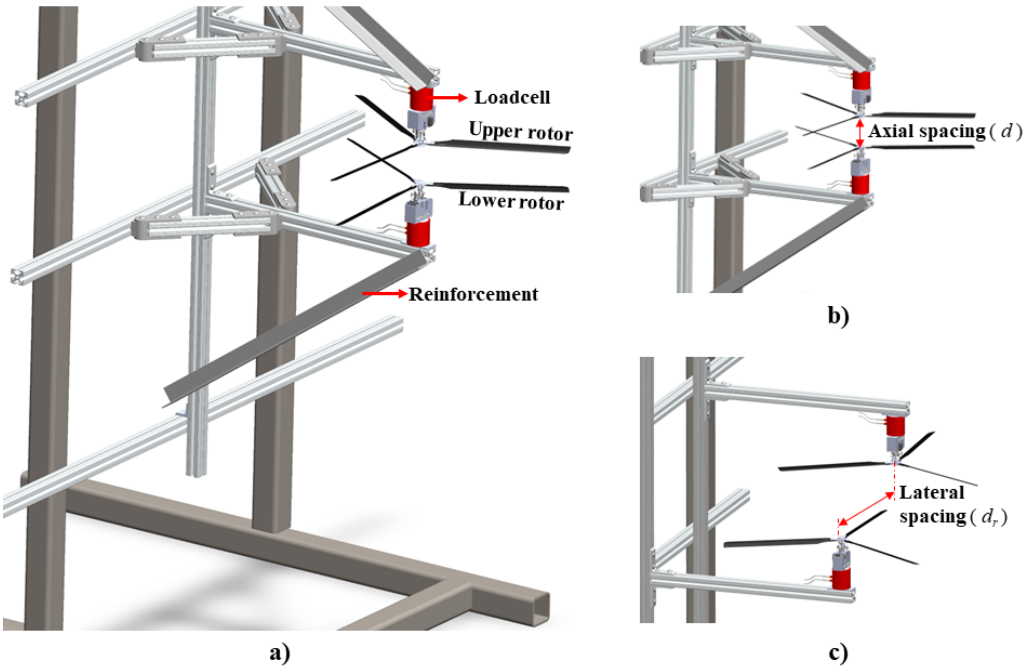

Figure 2.2: Modular and reconfigurable multi-rotor thrust stand: a) isometric view, b) coaxial, and c) tandem configurations. d and d_r are axial and lateral separation distances between rotor centers

on top of Sorbothane to dampen the rotor vibrations, primarily due to the natural frequency resonance of the system, which was observed to be around $1000Hz$. The three-bladed rotors had a disc diameter of $0.79\ m$, a hub diameter of $0.105\ m$, and a root cutout of $0.133D$. Each rectangular blade had a chord length (c) of $0.036\ m$ and a span b of $0.36\ m$ with zero-twist and a NACA0012 airfoil section. The specifications of the single rotor setup are summarized in Table 2.1.

The rotor consisted of a three-point swashplate, which enabled both the rotor blades' collective and cyclic pitch control. The swashplate was controlled by three servo motors (torque of $2.1\ kg-cm$ at $4.8V$) through connecting rods, and signals to the servo motors were supplied through ARDUINO MEGA interfaced with LabVIEW on a laptop computer. As the current study is focused on the hover operating conditions, only the collective pitch was varied without introducing a cyclic pitch. To calibrate and trim the servo motors, an empirical relationship was developed between the angle input to the computer and the observed collective pitch of the blades, shown in Fig.2.3a. After the calibration, the collective pitch angle for each blade was measured using a digital pitch angle gauge with respect to the hub. The collective pitch angle

Table 2.1: Specifications of a single rotor

Parameter	Value	Units
Rotor radius, R	0.395	m
Number of blades, N_b	3	
Blade span, b	0.36	m
Blade chord, c	0.036	m
Rotor solidity, σ	0.087	
Root cutout,	$0.133D$	
Blade airfoil profile	NACA0012	

was measured at three azimuth angles of 120° apart for collective pitch angle input of 2°, 4° and 6° and is summarized in Fig.2.3b, a maximum deviation of less than 0.2° was observed in all the measurements across three different azimuthal angles.

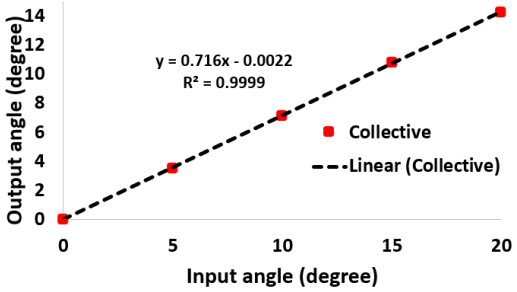

a)

	Collective Output (degree)		
Collective input (degree)	Blade 1	Blade 2	Blade 3
2°	2.10 ± 0.10	1.97 ± 0.21	2.1 ± 0.17
4°	3.96 ± 0.06	3.83 ± 0.06	3.93 ± 0.06
6°	5.97 ± 0.15	5.86 ±0.12	6.07 ± 0.15

b)

Figure 2.3: Servo calibration curve and summary of collective output after the calibration

The operating thrust and torque conditions for the experiments in this thesis were achieved by adjusting the collective pitch of each rotor using three servo motors. A digital pitch gauge with a resolution of 0.1° was used to measure the collective pitch setting of each blade at static conditions. The thrust and torque exerted by each rotor were measured simultaneously using a combined thrust and torque load cell (FUTEK MBA500). The loadcells were factory calibrated to $F_z = 45N$ and $T_z = 1.13N - m$ with an $R^2 \sim 0.99$. The calibrations were confirmed in the laboratory settings as well.

The aerodynamic loads and RPM data were collected using LabVIEW software and an NI USB-6341 acquisition device. Since the loadcell signals were in the millivolt range, they were amplified using FUTEK amplifiers (IAA 200) before being connected to the analog input of the NI USB-6341. The rotational speed of the rotors was measured using a Digiten Hall NPN proximity sensor, which generates digital impulses when a magnet passes close by. A magnet

was attached to the gearhead to capture these pulses, and the proximity sensor was placed just below the gearhead on the rotor head. This setup provided digital signals with one pulse per revolution resolution. The analog output from the proximity sensor was connected to the analog input of the NI USB-6341, and the pulses were counted during post-processing to determine the exact rotor rotating frequency. For a visual representation of the circuit diagram used in the aerodynamic coaxial rotor thrust stand, please refer to Fig. 2.4.

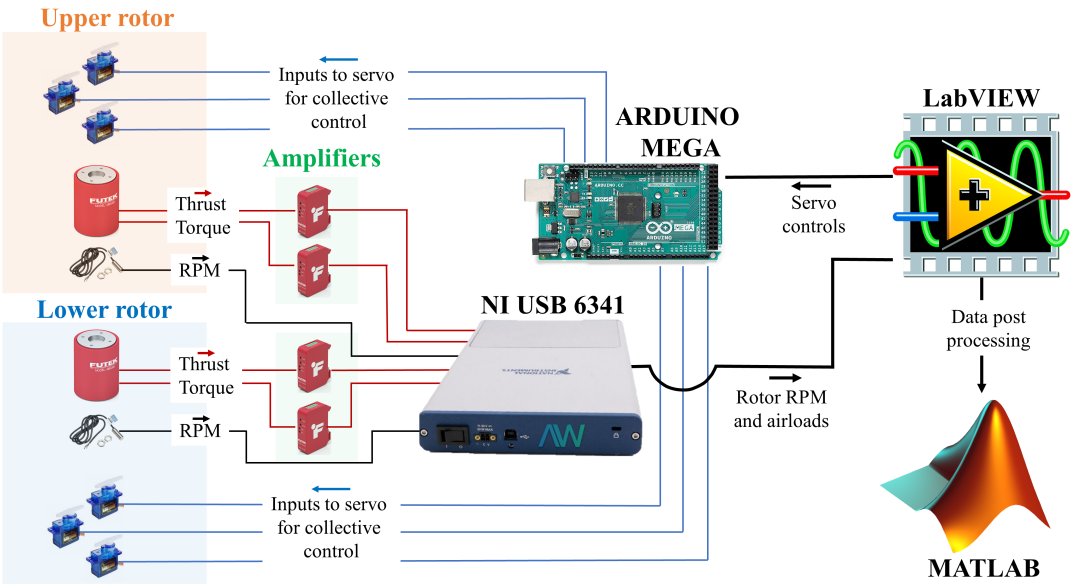

Figure 2.4: Wiring diagram for the aerodynamic coaxial rotor thrust stand instrumentation. Arrows represent the direction of the signals.

After acquiring the load and RPM measurements from LabVIEW, the data were post-processed in MATLAB. The post-processing involved applying the calibration factor to the raw data originally acquired in Volts. The data were then averaged over 40 seconds to remove the temporal effects and analyze the steady-state rotor characteristics. For calculating the non-dimensional rotor performance metrics (discussed in the later section), the tip Reynolds number was calculated using the blade chord, and the rotor tip rotational speed as determined from the RPM measurements.

2.3 Hydrodynamic towing tank facility

The experiments for the second aim of this dissertation were conducted in a hydrodynamic towing tank facility with a $2.4 \times 0.6 \times 0.6\ m$ dimension. The facility consisted of two identical

linear actuators (actuation length – $1m$) that were mechanically coupled and were driven by a single AC servo motor (ECMA-C20807RS), as shown in Fig. 2.5. The AC servo motor was controlled using a Delta servo motor controller (Delta ASD-B2-0721-B). The servo motor and the controller were placed on a common ground to reduce electromagnetic interference on the instrumentation.

The linear actuators were mechanically coupled using a bevel gear arrangement with a $1:1$ gear ratio to achieve the opposite translation motion of the two blades at the same speed. The blades were attached to the linear translation stage platform through an interface that housed multi-axis loadcells for measuring the blade load (lift, drag, and pitching moment). The detailed CAD drawing of the wing and the wing-loadcell adapter is shown in Fig. 2.5. The facility had a bottom and a top plate at a separation distance equal to the blade span to avoid three-dimensional and surface wave effects. To accommodate changing the spacing between the blades, the top plate included multiple slots, each with a length of $1\ m$ and width of $0.015\ m$.

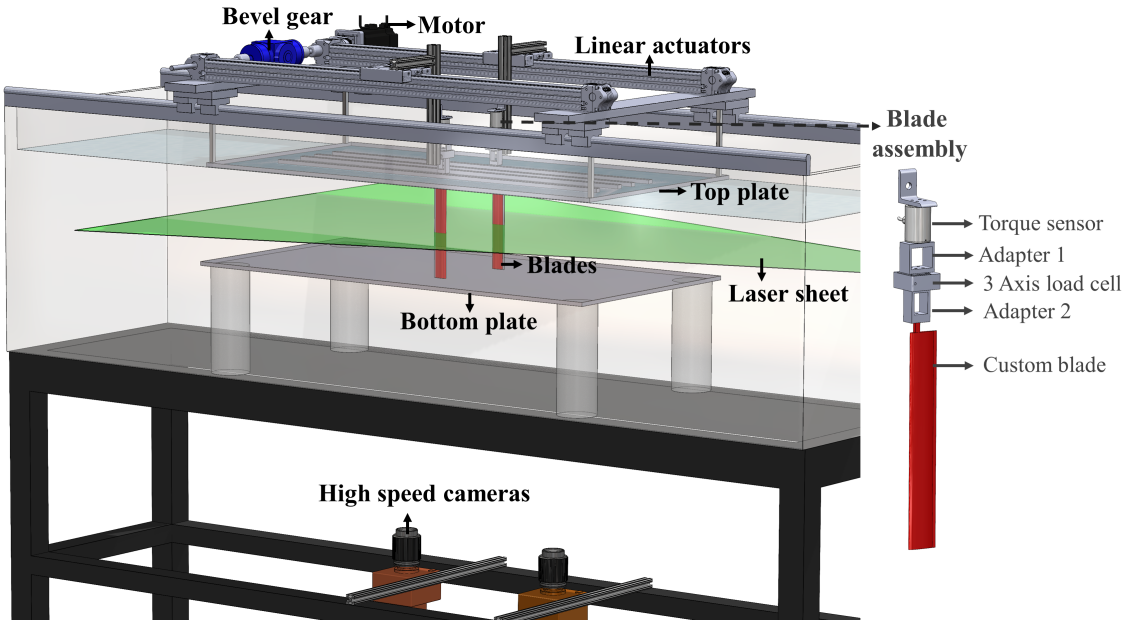

Figure 2.5: CAD representation of the hydrodynamic towing tank facility.

The lift and drag were measured using a multi-axis force loadcell calibrated to $10N$. Similarly, the pitching moment was measured using a single-axis moment sensor calibrated to $0.12\ N-m$. These loadcells had a sensitivity of $0.2\ mV/V$. The loadcells were connected to Tacuna EMBSGB200 amplifiers, which filtered, amplified, and converted the millivolt signal

into $(0 - 5)\ V$ output range. In addition to measuring the loads experienced by the blades, the position of the wing was also measured. This was achieved through an encoder that was embedded in the servo motor. The encoder had a resolution of 17 bits, which provided 131,072 discrete positions per revolution. However, the signal from this encoder had high-frequency noise due to electromagnetic interference. Thus, the data wes filtered using a first-order low-pass filter.

An additional limit switch was also placed at the cross-over location to confirm further and quantify the exact location of the cross-over between the two wing sections. The cross-over location was defined as where the wing's quarter-chord location was aligned perpendicular to the translation direction. The loadcell and encoder data were acquired through analog and digital modules attached to a cDAQ-9174 chassis. The loadcell data was acquired through an NI-9239 analog input module, while the encoder data was acquired through an NI-9401 digital module. The schematic representation of the wiring diagram for the instrumentation of this hydrodynamic towing tank facility is summarized in Fig. 2.6.

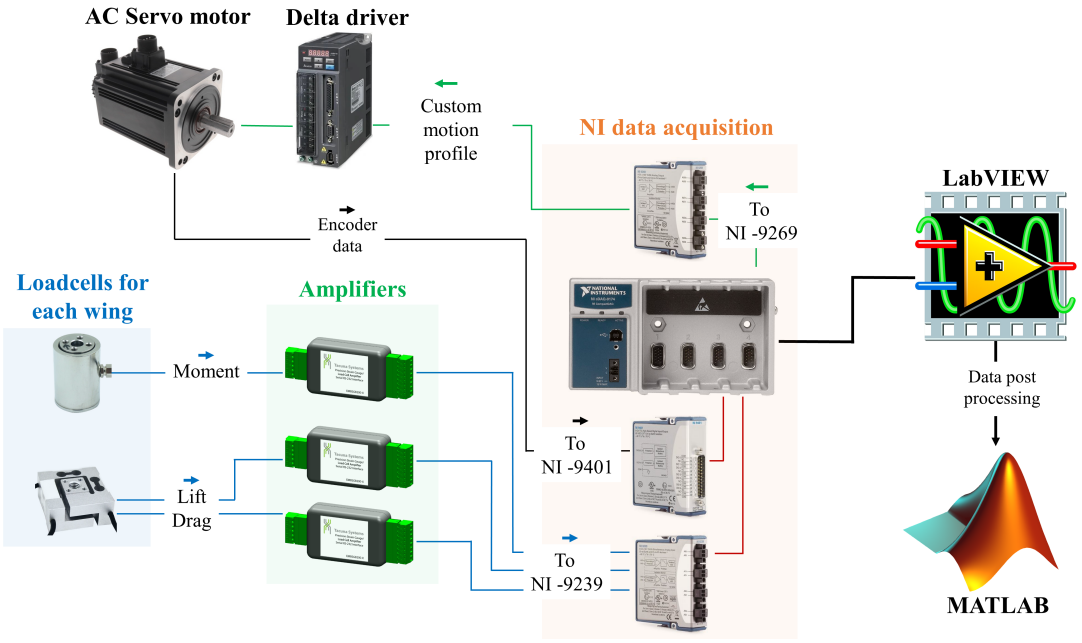

Figure 2.6: Wiring diagram for the hydrodynamic towing tank facility instrumentation. Arrows represent the direction of the signals.

The servo drive's speed control mode controlled the translation stage with analog command input. The desired motion profile was expressed as a waveform in the $(\pm 10)\ V$ voltage

range, which was generated using a NI-9269 analog output module. The servo drive translated the instantaneous voltage to a speed command and adjusted the motor's speed through a closed control loop. A sinusoidal velocity profile was fed into the drive to validate the system's ability to replicate the intended motion. The actual velocity of the translation stage was measured using the motor's encoder. Fig. 2.7 compares the input and actual velocity profiles. The results affirm a close match between the two velocity profiles, showcasing the system's capability to faithfully realize the desired motion profile using the analog speed control mode.

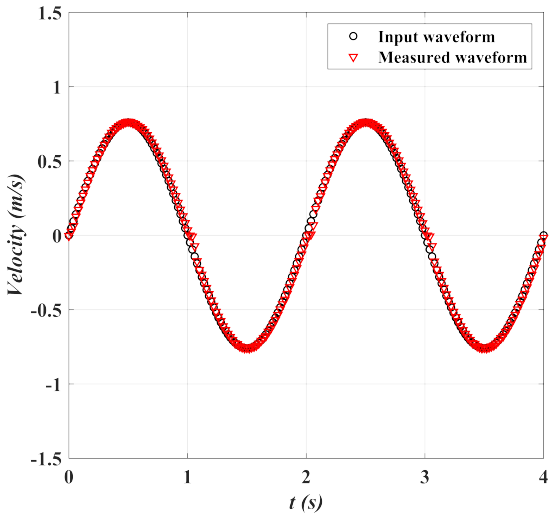

Figure 2.7: Sinusoidal velocity profile fed into the servo motor drive.

The data obtained from the loadcells and the encoder underwent post-processing using MATLAB. The first step involved applying calibration to the raw data initially acquired in Volts. Subsequently, phase averaging and filtering were performed on the data. These processes were particularly important for the current setup due to significant noise in the loadcell readings caused by inherent system vibrations. These vibrations could be attributed to various sources such as the motor, bevel gear, the translation belt in the linear actuator, or a combination of these factors.

The noise from vibrations was most noticeable at lower angles of attack, primarily because of the lower signal-to-noise ratio in these conditions. Fortunately, the vibrations typically occurred at higher frequencies ($> 50Hz$) than the frequencies of interest ($< 30Hz$). A digital low-pass filter with a cutoff frequency of less than 30 Hz and zero phase lag was applied to all

the data obtained from the experimental setup to address this issue. This application of the low-pass filter effectively improved the signal-to-noise ratio and produced meaningful and reliable results.

2.4 Performance metrics

The lift, drag, and moment of the wings are presented in non-dimensional form as the lift coefficient (C_L), drag coefficient (C_D), and coefficient of moment (C_M) given by

$$C_L = \frac{L}{0.5\rho(v)^2 A_b} \qquad C_D = \frac{D}{0.5\rho(v)^2 A_b} \qquad C_M = \frac{M}{0.5\rho(v)^2 A_b c} \tag{2.1}$$

where, ρ in the fluid density, v in the freestream velocity, A_b is the blade area, and c is the blade chord length.

The thrust and torque data for the individual rotors and the CCR as a whole are presented in non-dimensional form as thrust coefficient (C_T) and torque coefficient (C_Q) given by

$$C_T = \frac{T}{\rho(\Omega R)^2 A_d} \qquad C_Q = \frac{Q}{\rho(\Omega R)^2 R A_d} \tag{2.2}$$

where, ρ is the density of air, Ω is the rotation rate of the rotors, R is the rotor disk radius, A_d is the rotor disk area given by πR^2. The performance of the individual rotors was quantified using the figure of merit (FM), which represents the ratio of actual power (torque) to the ideal induced power, as given by the following expression

$$FM = \frac{(C_T)^{3/2}}{\sqrt{2}C_Q} \tag{2.3}$$

where the C_T and C_Q are the thrust and torque coefficients for the specific individual rotors. The performance of the whole CCR system was quantified using a modified definition of figure of merit (FM_{CCR}) as suggested by Leishman [36], given below

$$FM_{CCR} = \frac{({C_{T_u}}^{3/2} + {C_{T_l}}^{3/2})}{\sqrt{2}(C_{Q_u} + C_{Q_l})} \tag{2.4}$$

where C_{T_u}, C_{Q_u}, C_{T_l}, and C_{Q_l} are the thrust and torque coefficients of the upper and lower rotor, respectively.

2.5 Flow diagnostics

In the current research, flow measurements were a crucial aspect of both the aerodynamic coaxial rotor thrust stand and the hydrodynamic towing tank facility studies. Planar Particle Image Velocimetry (PIV) was employed for time-resolved flow measurements. A dual-head Nd: YLF laser with a wavelength of $527nm$ and an energy output of $30mJ$ per pulse at $1kHz$ was used to achieve proper illumination for PIV. High-speed cameras of the VEO 640L series, capable of capturing images at 1400 frames per second (fps) with a resolution of 2560×1600 pixels, were employed to record the flowfield images. A fixed focal length lens with a $50mm$ focal length and an aperture setting of f/1.8 was utilized for the cameras. Data acquisition for PIV was performed using DaVis software provided by LaVision Inc., and precise timing control was achieved through a Programmable Timing Unit (PTU X) also provided by LaVision Inc.

For synchronization, external triggers from NI-DAQ devices were used to initiate data acquisition via the PTU X. The wiring diagram for PIV, depicting the setup used for synchronization, is illustrated in Fig. 2.8. Additionally, the current research accounted for the uncertainties associated with the flow measurements conducted using PIV. These uncertainties were evaluated for experiments conducted in both the aerodynamic coaxial rotor thrust stand and the hydrodynamic towing tank facility. The method employed for uncertainty quantification followed the approach described by Weineke [66].

In this technique, the uncertainty is proportional to the residual positional disparity between the matched correlation peaks, and it's a standard feature within the DaVis software. Weineke [66] argued that various error sources, such as particle image size and shape, camera noise, seeding density, illumination intensity variation, particle motion, and image interrogation, are encoded in the images themselves, and quantifying these sources provides insight into the associated uncertainties. However, it's important to note that the method proposed by Weineke [66, 67] doesn't account for uncertainties linked to tracer particle response, perspective errors, and calibration errors. As such, the current research also evaluated these errors for

each experimental condition to provide a comprehensive assessment of measurement uncertainties.

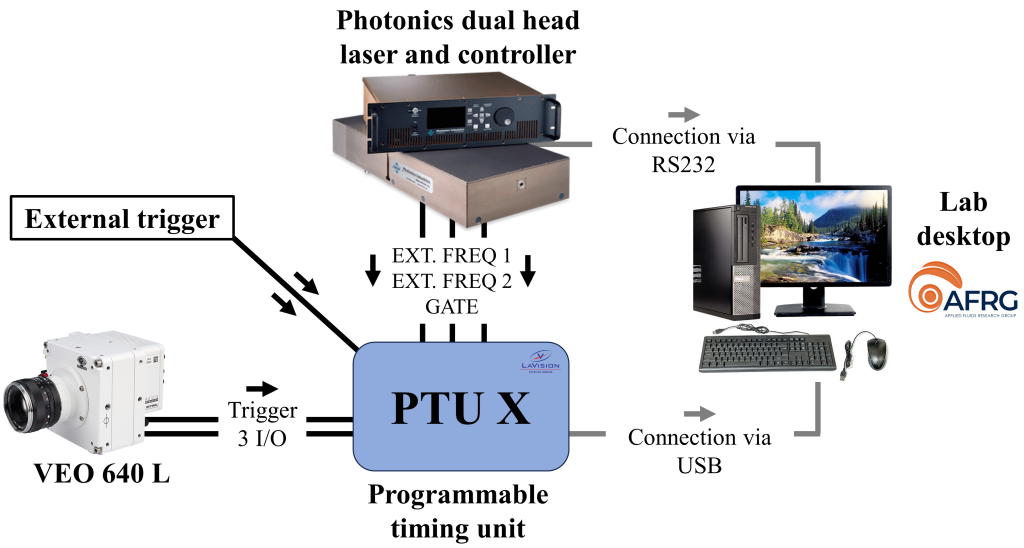

Figure 2.8: Wiring diagram for the particle image velocimetry system. Arrows represent the direction of the signals.

2.5.1 Aerodynamic coaxial rotor thrust stand

The flow measurements here were carried out in air with smoke particles used as a seeding material. The size of the particles varied between $2 - 10\ \mu m$. The particle Stokes number was quantified to determine the potential *lead/lag* error in the measurements due to the current particle size. First, the relaxation time (τ_p) for the maximum particle size was determined. The particle relaxation time provides a measure for the settling time of the particle to a sudden change in the fluid medium. The relaxation time is given as:

$$\tau_p = \frac{{d_p}^2(\rho_p - \rho_f)}{18\mu_f} \tag{2.5}$$

where d_p is the maximum particle size considered, i.e., $10\ \mu m$, ρ_p is the particle density, i.e., $1000\ kg/m^3$, ρ_f is the fluid density, i.e., $1\ kg/m^3$, and μ_f is the dynamic viscosity of air, i.e., $1.81e-5kg/(m.s)$. The particle relaxation time was calculated to be $\tau_p = 0.0005s$. The characteristic time scale for the particle in the velocity field has been determined to be

$\tau_{flow} = 0.037s$ from the measured velocity field. The particle Stokes number is then given as:

$$S_k = \frac{\tau_p}{\tau_{flow}} \tag{2.6}$$

The particle Stokes number was calculated to be $S_k = 0.013$, much less than the recommended limit for negligible lead/lag error, i.e., $S \leq 0.05$ [68]. This calculation suggests that these measurements' lead/lag error is minimal.

Another potential source of error is peak locking. This occurs when the particle image is small compared to the pixel size, i.e., a particle image covering less than one pixel. In this scenario, the particle displacement biases towards an integer value and results in either underestimation or overestimation of the particle displacement [69]. The occurrence of errors due to *peak locking* was also checked by monitoring the probability distribution of the pixel shift. No biasing was observed in the histogram, suggesting the peak locking did not occur for the current measurements.

The near wake flowfield was measured using planar PIV with the 4MP (Vision Research VEO 640S with 1400 fps) camera viewing approximately $(0.45 \times 0.28)m$, i.e., $(1.12R \times 0.7R)$ of the field of view. Two thousand image pairs were acquired in frame-straddled mode at14 the rate of $700Hz$ with an optimized time difference (δt) between the frames for each experiment. A standard calibration plate provided by LaVision was used to calibrate the field of view. The resulting reprojection error for the calibration process was < 0.4 pixel for all the experimental acquisitions.

The raw PIV images were acquired and processed using DaVis 10.0.3. Image processing included background noise reduction by subtracting the sliding average from the raw image. The velocity fields were then obtained by processing the images using the multi-grid, multi-pass cross-correlation technique with an initial and final interrogation window of size 64×64 pixels and 32×32 pixels, respectively, each with an overlap of 14%. The vector fields were post-processed to remove spurious vectors, which were then stitched together to obtain the final flowfield with a $1.19mm$ $(0.0015D)$ vector spacing resolution. The uncertainties in the velocity measurements were quantified using the correlation statistics method [66]. The

resulting uncertainty in the velocity across the flowfield for all cases was $\leq 1\%$ of the average velocity in the flow field.

2.5.2 Hydrodynamic towing tank facility

The blade flowfield was measured using time-resolved particle image velocimetry (PIV). The laser sheet was located mid-span of the blade and was parallel to the translation direction. The cameras were placed below the towing tank, as shown in Fig. 2.5. VEO 640L high-speed cameras, which can capture the images at $1400\ fps$ at 2560×1600 pixels, were used to capture the flowfield images. These cameras were placed side-by-side to maximize the field of view (FOV). Each camera covered a FOV of $(10.4 \times 6.5)c$, and with an overlap of 14% between the FOV of the two cameras, the resultant FOV was $(18.2 \times 6.5)c$. The calibration for PIV measurements was carried out simultaneously for both cameras with the same calibration plate that covered the entire field of view. Each case's magnification and calibration factors were around 0.068 and $6.85\ pixel/mm$, respectively. The reprojection error for the calibration process using the custom calibration plate was ≤ 0.4 pixel for all the cases.

The current study used polyamide spheres with a mean particle diameter of $55\ \mu m$ as seeding particles. The relaxation time (τ_p) for these particles in water was calculated to be $\tau_p = 0.43s$ using Eq. 2.5. Similarly, the time scale of the fluid was determined to be $\tau_{flow} = 12s$ by evaluating the flowfield. The particle Stokes number then comes out to be $St_k = 0.035$, less than the recommended value of $S_k \leq 0.05$. This confirms that the lead/lag error did not exist in the current measurements. The occurrence of errors due to peak locking was also checked by monitoring the probability distribution of the pixel shift. No biasing was observed in the histogram, suggesting the peak locking did not occur for the measurements in the hydrodynamic towing tank.

The raw PIV images were acquired and processed using DaVis 10.2. The flowfield data was acquired at $400\ Hz$ in time-series mode. The velocity fields were then obtained by processing the images using the multi-grid, multi-pass sliding sum-of-correlation cross-correlation technique with an initial and final interrogation window of size 64×64 pixels and 24×24 pixels, respectively, each with an overlap of 50%. The filter length for the sliding sum-of-correlation

was set to 4. The vector fields were post-processed to remove spurious vectors, which were then stitched together to obtain the final flowfield with a $1.75\ mm$ $(0.048\ c)$ vector spacing resolution. The uncertainties in the velocity measurements were quantified using the correlation statistics method [66]. The resulting uncertainty in the velocity across the flowfield for all cases was observed to be $\leq 1\%$ of the average velocity in the flow field.

2.6 Control volume analysis

The contributions of the non-circulatory and circulatory effects on a body submerged in a fluid medium can be determined by evaluating the temporal and convective acceleration terms in the Navier-Stokes equation. A control volume (CV) (refer to Fig. 2.9) approach has been used to extract blade load from the velocity field obtained from the PIV measurements. The total force acting on a body($F_B = F_{B1} + F_{B2}$) immersed in an incompressible flow is given by the integral form of the N-S equation:

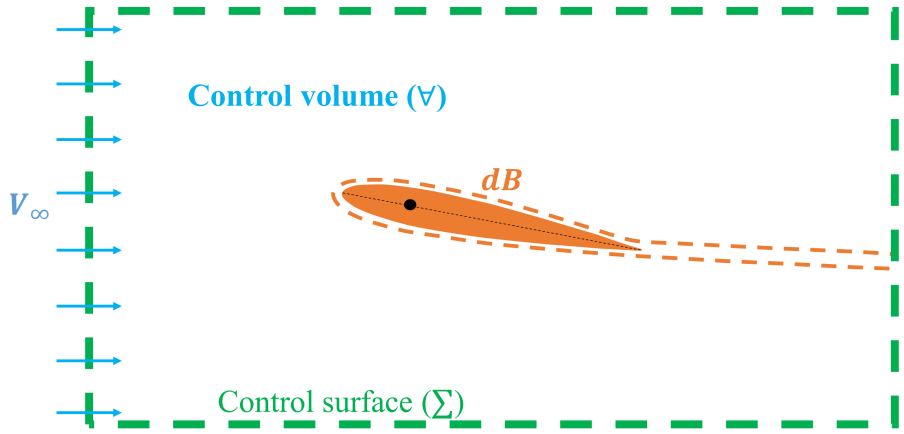

Figure 2.9: Graphical representation of the control volume approach to analyze load on a body submerged in a fluid medium.

$$\underbrace{F_B}_{\text{Load cell}} = \underbrace{-\rho \iiint_{\forall} \frac{\partial}{\partial t}(\mathbf{u}) d\forall}_{\text{Temporal acceleration}} \underbrace{- \iint_{\sum} \mathbf{u}(\mathbf{u}\cdot\mathbf{n})\, dS}_{\text{Convective acceleration}} - \iint_{\sum} (p\mathbf{n}) ds + \iint_{\sum} (\bar{\bar{\tau}}\cdot\mathbf{n}) ds \tag{2.7}$$

where p is the pressure, τ is the surface shear stress, $\mathbf{u}$ is the velocity, and $\mathbf{n}$ is the normal vector to the control surfaces. The inertial and pressure term in the above equation from the PIV data can be evaluated through the derivative moment transformation (DMT) formulation, which

transforms these components to the surface integral of the spatial derivatives of the velocity along the control surface ($\sum$). The DMT formulation has been used in multiple studies to evaluate the unsteady forces experienced by a single body undergoing an unsteady motion when immersed in an incompressible fluid [70, 71]. From the DMT formulation and Leibniz integral theorem, the first term can be transformed as:

$$\rho \iiint_{\forall} \frac{\partial}{\partial t}(\mathbf{u}) d\forall = \rho \frac{\partial}{\partial t} \left(\cancelto{0}{\iiint_{\forall} \mathbf{x}(\nabla \cdot \mathbf{u})\, d\forall} + \iint_{\sum} \mathbf{x}(\mathbf{u} \cdot \mathbf{n}) ds \right) \tag{2.8}$$

where, $\mathbf{x}$ is the position vector measured from any fixed origin. Similarly, the pressure term in Equation 2.7 can be replaced by the acceleration term using the DMT identity and the local momentum balance, which are given below:

$$\iint_{\sum} (p\mathbf{n}) dS = -\frac{1}{n-1} \iint_{\sum} \mathbf{x} \times (\mathbf{n} \times \nabla p) dS, \quad \nabla p = -\rho \mathbf{a} - \mu \nabla \times \omega \tag{2.9}$$

where, n is the spatial dimension and ω in the vorticity. Now, Equation 2.7 can be written as:

$$\begin{aligned} \underbrace{F_B}_{\text{Load cell}} = & \underbrace{-\rho \frac{\partial}{\partial t} \iint_{\sum} (\mathbf{x})(\mathbf{u} \cdot \mathbf{n}) dS}_{\text{Temporal acceleration}} \underbrace{- \iint_{\sum} \mathbf{u}(\mathbf{u} \cdot \mathbf{n})\, dS}_{\text{Convective acceleration}} + \\ & \frac{1}{n-1} \iint_{\sum} \mathbf{x} \times (\mathbf{n} \times (-\rho \mathbf{a} - \mu \nabla \times \omega)) ds + \iint_{\sum} (\bar{\bar{\tau}} \cdot \mathbf{n}) ds \end{aligned} \tag{2.10}$$

Here, all the components on the right-hand side have been expressed in terms of the surface integral of the spatial derivatives of the velocity along the control surface. This allows us to evaluate the contribution of temporal and convective components on the blade airload from the PIV measurements.

Chapter 3

Characterization of the aerodynamic coaxial rotor thrust stand

The coaxial rotor thrust stand utilized modified rotors originally sourced from a commercially available unmanned aerial vehicle, the Blade 360. These rotors were equipped with symmetric airfoil profile section blades. On the thrust stand, these rotors were outfitted with instrumentation to measure critical operational parameters, including rotational speed, thrust, and torque. To initiate the research process, it was imperative first to evaluate and compare the performance characteristics of the commercially available symmetric blade and the modified rotors. This comparative analysis was essential to ensure the system could conduct rigorous scientific investigations in line with established literature. Moreover, assessing and recording the flowfield characteristics near the rotor was necessary. This step was crucial to establish the thrust stand's competence for executing scientific inquiries effectively. This chapter presents the results from the performance and flowfield measurements to validate the aerodynamic coaxial rotor thrust stand.

3.1 Objectives

The objectives of this study are summarized below:

1. To characterize the static performance of the blades used in the aerodynamic coaxial rotor thrust stand rotors and compare with the literature.

2. To measure the performance and flowfield behavior of the rotor in the single rotor and CCR configuration and compare with the literature.

3.2 Approach

The static blade characteristics were investigated using the static blade characterization rig, the development of which is detailed in Section 2.1. This involved measuring the blade coefficient of lift (C_L) and coefficient of drag (C_D) variation with changes in the blade's angle of attack. The data was then compared with existing literature for validation. Similarly, the performance of the individual rotors was methodically assessed within the aerodynamic coaxial rotor thrust stand, the specifics of which can be found in Section 2.2. Key performance metrics such as the rotor coefficient of thrust (C_T), coefficient of torque (C_Q), and figure of merit (FM), as outlined in Section 2.4, were employed for rotor characterization. These metrics were subsequently compared with data available in relevant literature. Moreover, the performance characteristics of the CCR were measured under varying rotor spacings, with findings compared to previous research conducted by Ramasamy [6]. The time-averaged flowfield characteristics in the CCR near wake were also analyzed. The flow field measurements were carried out in thrust-matched conditions to isolate the effects of rotor spacing in the near wake characteristics.

3.3 Operating conditions

This section describes the operating conditions for the performance and flowfield measurement of CCR under out-of-ground conditions (OGE).

3.3.1 Performance measurements

The aerodynamic characteristics (lift and drag) of the blades used in the rotor were measured at an angle of attack (AOA) ranging from 0° to 12° for Reynolds number of 46,000 with an increment of 2° (Table 3.1). Smoke flow visualization was also carried out to substantiate the observations from the airload measurements. The out-of-ground (OGE) hover performance of each rotor currently used in the aerodynamic coaxial rotor thrust stand was characterized in single rotor configuration for three different Re_{tip} of $64000, 84000,$ and 98000 corresponding to RPMs of $650, 850,$ and 1000 respectively. The blade collective pitch was varied from 0° to 12° at an increment of 2° (Table 3.1).

Table 3.1: Experimental matrix for validation of the aerodynamic coaxial rotor thrust stand

Measurements	Test	α or $\theta_\circ$	Re_{tip}	d/R
Performance	Static blade	$\alpha = (0° - 12°)$	46000	-
	Single rotor	$\theta_\circ = (0° - 12°)$	64000, 84000, 98000	-
	CCR	$\theta_\circ$ (Upper rotor) = $6°, 10°$	64000, 84000, 98000	0.52, 0.42, 0.32, 0.23, 0.14
Flowfield	Single rotor ($C_T = 0.006$)	-	64000	
	Thrust-matched CCR ($(C_T)_{CCR} = 0.012$)	-	64000	0.352, 0.24, 0.14

After the characterization of the single rotor, the OGE hover characteristics of counter-rotating coaxial rotor (CCR) were studied at different axial separation distances of $d/R = 0.52, 0.42, 0.32, 0.23, 0.14$. The non-dimensional axial separation distance of $d/R = 0.14$ corresponds to the current full-scale operational coaxial rotor helicopter spacing. The Reynolds number effect was studied by varying the tip Reynolds number as $Re = 64000, 84000$, and 98000. The experiments for these spacings and Reynolds number were carried out for high and low thrust settings by adjusting the rotor collective. Torque-matched trim condition at the same RPM was imposed for the CCR study, and the trim condition was achieved by setting the upper rotor collective pitch constant and changing that of the lower rotor to match the torque. The operating conditions for this study are summarized in Table 3.1. The thrust and torque were acquired at the rate of 1KHz using a USB-6341 data acquisition device through LabVIEW software for all cases. Data were taken and averaged for over 40 seconds for a time-averaged study.

3.3.2 Flowfield measurements

The near wake flowfield was studied using PIV in thrust-matched trim condition at tip Reynolds number (Re_{tip}) $\sim$ 64,000. Each rotor was operated at a thrust coefficient (C_T) of 0.006 within a 5% uncertainty between the rotors for all cases. For comparison, single-rotor experiments were also carried out with the single rotor's thrust coefficient matched that of the individual rotors in CCR, i.e., $C_T = 0.006$. The operating conditions for this study are summarized in Table 3.1. It

should be noted that the CCR, in reality, operates in thrust-offset, torque-matched conditions for yaw trimming. However, the difference in thrust between the upper and lower rotor results in varying inflow distribution and tip vortex strengths. Matching the thrust between the upper and lower rotor ensured the production of tip vortices with equal strength. The thrust-matched trim condition also allows for comparing the inflow distribution with the single rotor. Any difference in the inflow can then be attributed to the interactional effects in CCR configuration. For these studies, the axial separation distance between the rotors was set at $d/R = 0.352, 0.24, 0.14$. The lower rotor was taken as a reference plane while changing the rotor spacing.

The near wake flowfield was measured using planar PIV with the 4MP (Vision Research VEO 640S with 1400 fps) camera viewing approximately $(0.45 \times 0.28)m$, i.e., $(1.12R \times 0.7R)$ of the field of view. As shown in Fig. 3.1, the field of view was kept constant for all the cases. A Photonics dual head laser (527 nm wavelength with pulse energy of 30mJ/pulse at 1kHz) operating in peer mode was used to produce the laser sheet by combining a collimator and cylindrical lenses. A total of 2000 images were acquired at 700Hz, and the time difference (δt) between the pulses was optimized for each case. A standard calibration plate provided by LaVision was used to calibrate the field of view, and the images were processed in DaVis 10 software, also provided by LaVision.

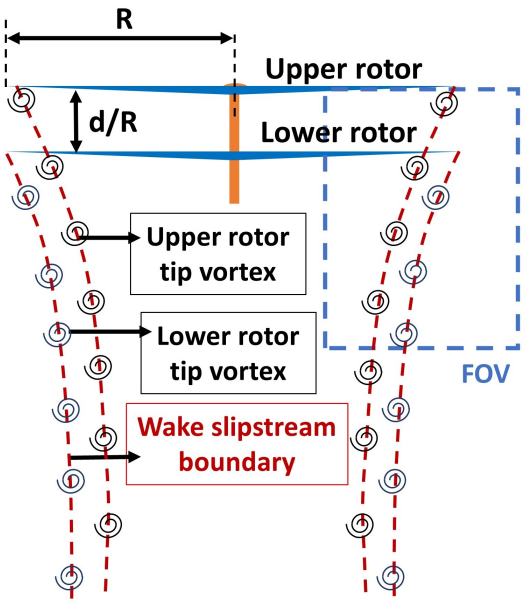

Figure 3.1: Hypothesized flowfield for coaxial rotor configuration in hover.

3.4 Results and Discussion

First, the results from the static blade characterization study are discussed. Then, the time-averaged performance characteristics of the rotors are presented, followed by the unsteady airload rotor characteristics.

3.4.1 Static blade performance characterization

The static blade performance characterization results are summarized in Fig. 3.2. From the figure, the lift produced by the blade was observed to follow the thin airfoil theory lift-curve slope, with blade stall marked at a nominally lower angle of attack of 7.5°. Flow visualization at an AOA of 5°, (Fig. 3.2a) showed no signs of separation, with the smoke trail observed to follow the airfoil curvature. At an AOA of 7.5°, (Fig. 3.2b), the separation was close to the leading edge, and at an AOA of 10°, (Fig. 3.2c), the flow was separated which further confirmed the airload measurements.

The findings from this study were also compared with a similar investigation conducted by Wang [72]. Wang's research examined NACA0012 airfoil sectioned blades at a low Reynolds number of 20,000. In Wang's study, the blades were observed to stall at approximately 13° with a maximum coefficient of lift (C_L) of 0.95. In contrast, the blades used in this study exhibited stalling at a lower angle of attack and achieved a lower C_{Lmax} value. This divergence in results is likely attributed to variations in the freestream turbulence intensity, with Wang [72] reporting a higher value of 0.6%, whereas measurements in the wind tunnel at Auburn University yielded turbulence intensities in the range of 0.1-0.2%. Furthermore, the drag coefficient obtained in the current research was marginally lower when compared to Wang [72]. Specifically, Wang reported a drag coefficient of around 0.15 at 10° for a Reynolds number of 20,000. At the same time, the measurements conducted in this study indicated a value of 0.12 for a Reynolds number of 46,000 at the same angle of attack.

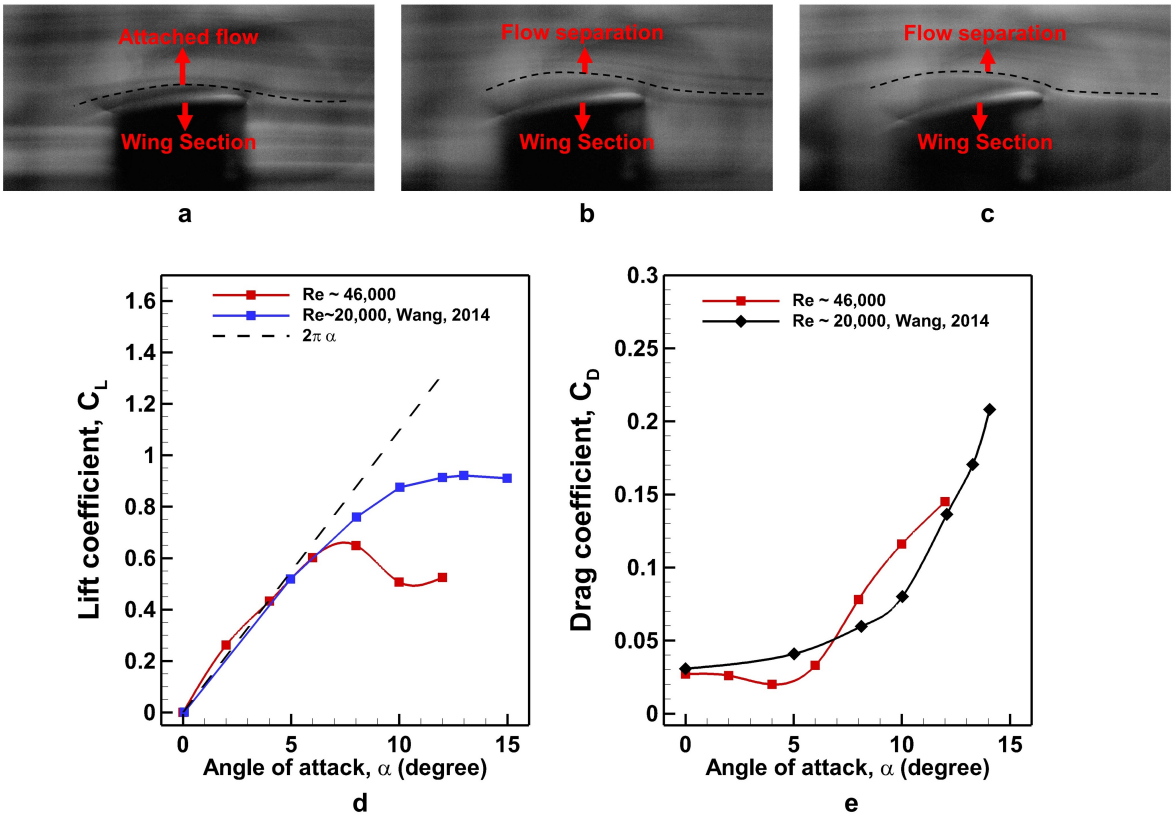

Figure 3.2: Performance characterization of the blade in static condition, Flow visualization for (a) $\alpha = 5°$, (b) $\alpha = 7.5°$, (c) $\alpha = 10°$, (d)Variation of lift coefficient, C_L with an angle of attack, α, (e)Variation of drag coefficient, C_D with an angle of attack, α.

3.4.2 Single rotor performance characteristics

As the rotor blades consisted of NACA0012 symmetric airfoil, both the rotors produced zero thrusts at $0°$ collective pitch (see Fig. 3.3). The torque at zero thrusts corresponds to the rotor profile power. The torque loading (C_Q/σ) at zero thrusts was observed to be slightly higher for Re_{tip} of 64000 when compared to the higher Re_{tip} of 84000 and 98000. The higher viscous induced profile drag at low speed (low Reynolds number) could be attributed to the observed variation in the torque loading.

The performance of the individual upper and lower rotors was evaluated using the Figure of Merit (FM) to assess their hover capabilities. A comparative analysis of the two rotors' performance is presented in Fig. 3.4. It was observed that the upper rotor's performance closely resembled that of the lower rotor across all Reynolds numbers tested. Furthermore, both the upper and lower rotors exhibited stalling behavior at angles of attack ranging from $8°$ to $10°$

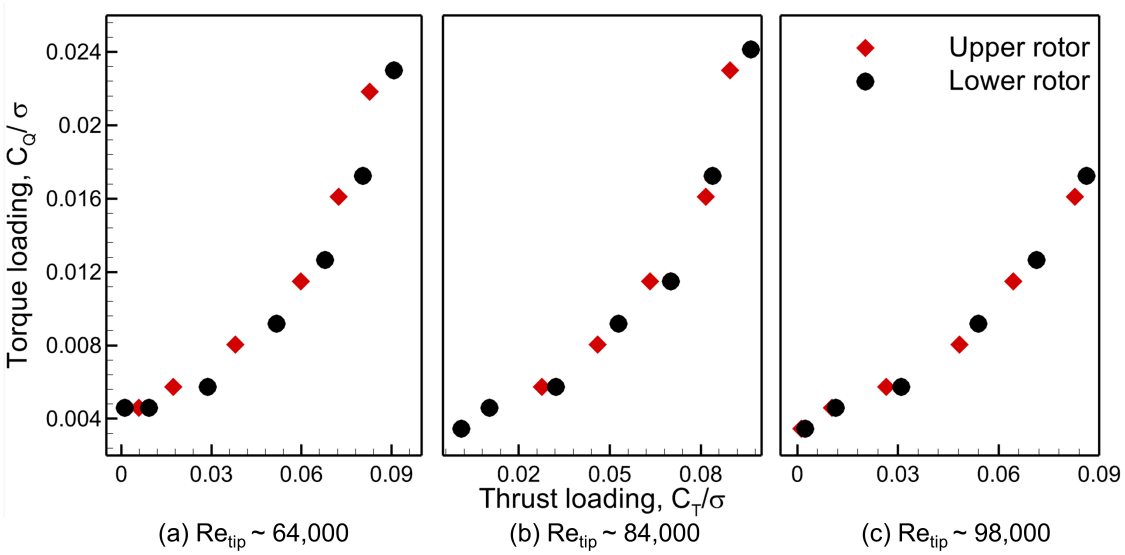

Figure 3.3: Performance characterization of the upper and lower rotor in single rotor configuration, C_T vs. C_Q, (a) Re_{tip} 64000, (b)Re_{tip} 84000, (c) Re_{tip} 98000

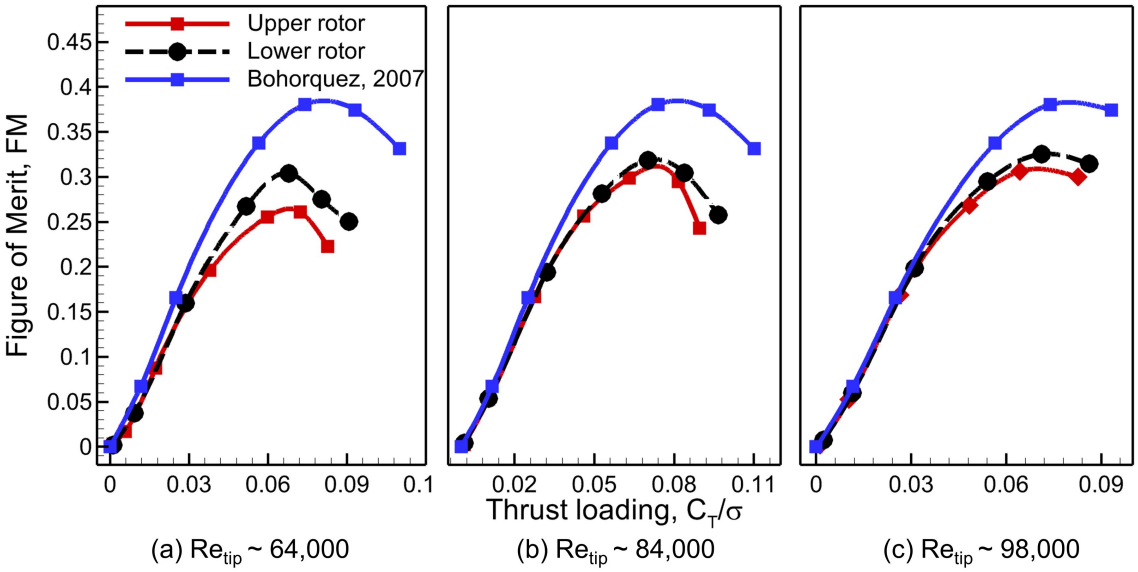

Figure 3.4: Performance characterization of the upper and lower rotor in single rotor configuration, C_T vs. FM, compared with Bohorquez [10] at Re_{tip} 27000 (a) Re_{tip} 64000, (b)Re_{tip} 84000, (c) Re_{tip} 98000

across all Reynolds number cases. These results confirm the identical nature of the two rotors used in the aerodynamic coaxial rotor thrust stand.

The obtained performance curves were also compared to data reported by Bohorquez [10], where a double-bladed rotor with NACA0012 airfoil profiles was employed. Bohorquez's study showed that the maximum FM reached approximately 0.36 at a tip Reynolds number of 27000, as depicted in Fig. 3.4. In contrast, the maximum FM observed in the present study at the

lowest Reynolds number, most similar to Bohorquez's conditions, was around 0.3. At higher Reynolds numbers (with tip Reynolds numbers of 84000 and 98000), the maximum FM did increase to approximately 0.34 but remained lower than Bohorquez's findings.

The disparity in the number of blades used in the two studies (2 blades in the current study vs. 3 blades in Bohorquez's study) could contribute to the observed differences in the maximum FM. The additional blade in the present study introduced added profile drag, reducing rotor efficiency. After assessing the performance of each independent rotor in out-of-ground (OGE) hover conditions, further investigations were conducted to analyze their performance in a counter-rotating coaxial rotor configuration. The study explored the effects of varying axial separation distance, Reynolds number, and thrust conditions and compared the results with existing literature.

3.4.3 Time-averaged coaxial rotor performance characteristics

The effects of axial separation distance and tip Reynolds number on the performance of counter-rotating coaxial rotors were studied at two different thrust conditions. The collective pitch of the upper rotor was fixed at 10° for the higher thrust setting and was set at 6° for the lower thrust setting. The collective of the lower rotor was adjusted to achieve torque matching between the two rotors. The thrust and torque data were measured at the rate of 1kHz and averaged over 40 seconds for this time-averaged study.

Performance characterization of the rotor at low thrust settings

The upper rotor was set at a collective pitch of 6°, corresponding to the average C_T of 0.0038 at a single rotor configuration. The axial separation distance was changed from $d/R = (0.52R - 0.14R)$ at three Re_{tip} of $64000, 84000,$ and 98000. The results are summarized in Fig. 3.5 and Fig. 3.6, which illustrate the variation of thrust loading coefficient and figure of merit for the CCR as a function of axial separation distance (d/R).

The impact of reducing the axial separation distance on rotor performance was investigated across various Reynolds number cases, revealing highly non-linear changes, as illustrated in Figure 3.6. As the rotor spacing was reduced from $d/R = 0.52$ to $d/R = 0.32$, the lower

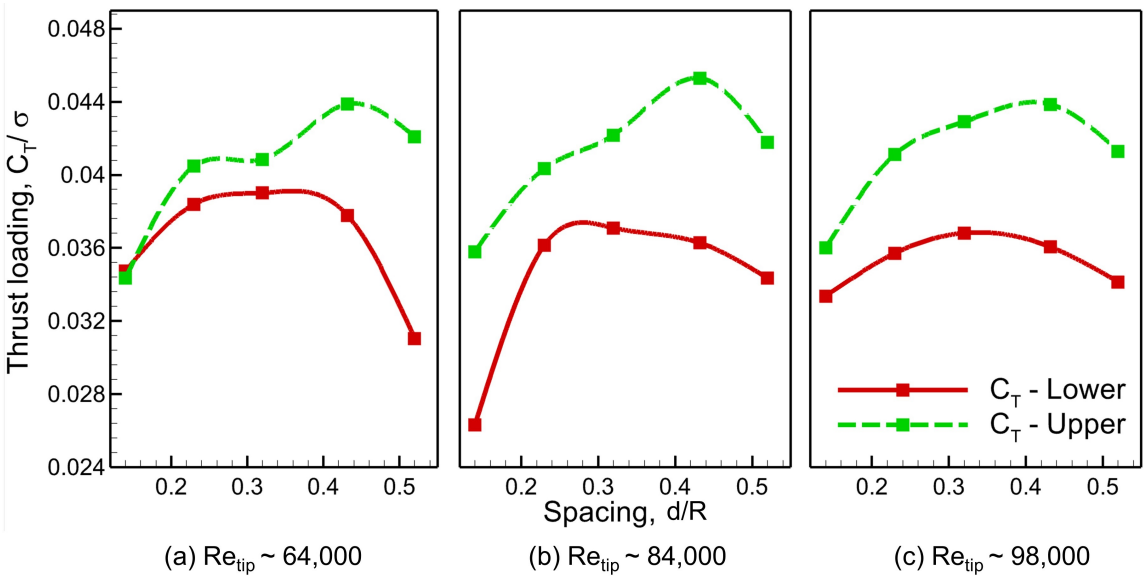

Figure 3.5: Variation of thrust coefficient, C_T with respect to axial separation distance at low thrust settings, (a) Re_{tip} 64000, (b)Re_{tip} 84000, (c) Re_{tip} 98000

rotor's performance exhibited a notable increase, with gains of 19.9%, 9.5%, and 8% observed for Re_{tip} values of $64000, 84000,$ and 98000, respectively. Conversely, when the rotor spacing was further reduced from $d/R = 0.32$ to $d/R = 0.14$, the lower rotor's performance experienced declines of 6%, 4.2%, and 3.4% for $Re_{tip} = 64000, 84000,$ and 98000, respectively. In summary, the overall performance of the lower rotor was enhanced as the spacing was reduced from $d/R = 0.52$ to $d/R = 0.14$, resulting in performance increases of 16%, 5%, and 4.7% for Re_{tip} values of $64000, 84000,$ and 98000, respectively.

For the upper rotor, a decreasing trend in the performance was observed with the decrease in the axial separation distance for all Re_{tip}. This suggests an increasing effect of the lower rotor on the upper rotor, which is consistent with the observations made by Ramasamy [6]. The upper rotor performance initially increased by 5.7% for Re_{tip} of 84000 and by 3.7% for Re_{tip} of 98000 but remained almost identical for Re_{tip} of 64000 when the rotor spacing was reduced from $d/R = 0.52$ to $d/R = 0.432$. The upper rotor's performance decreased when spacing was below $0.864R$ for all Re_{tip}. The upper rotor's overall performance reduced with a decreased axial separation distance from $d/R = 0.52$ to $d/R = 0.14$. The reduction in FM was measured to be 23%, 16.5%, and 12.5% for $Re_{tip} = 64000, 84000,$ and $98000,$ respectively.

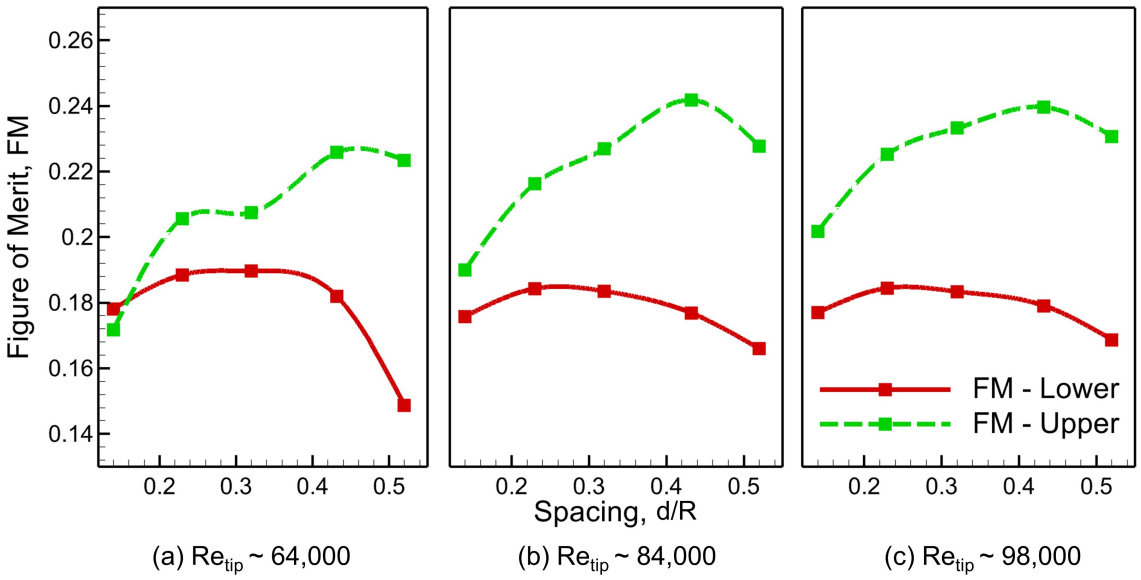

Figure 3.6: Variation of Figure of Merit, FM with respect to axial separation distance at low thrust settings, (a) Re_{tip} 64000, (b)Re_{tip} 84000, (c) Re_{tip} 98000

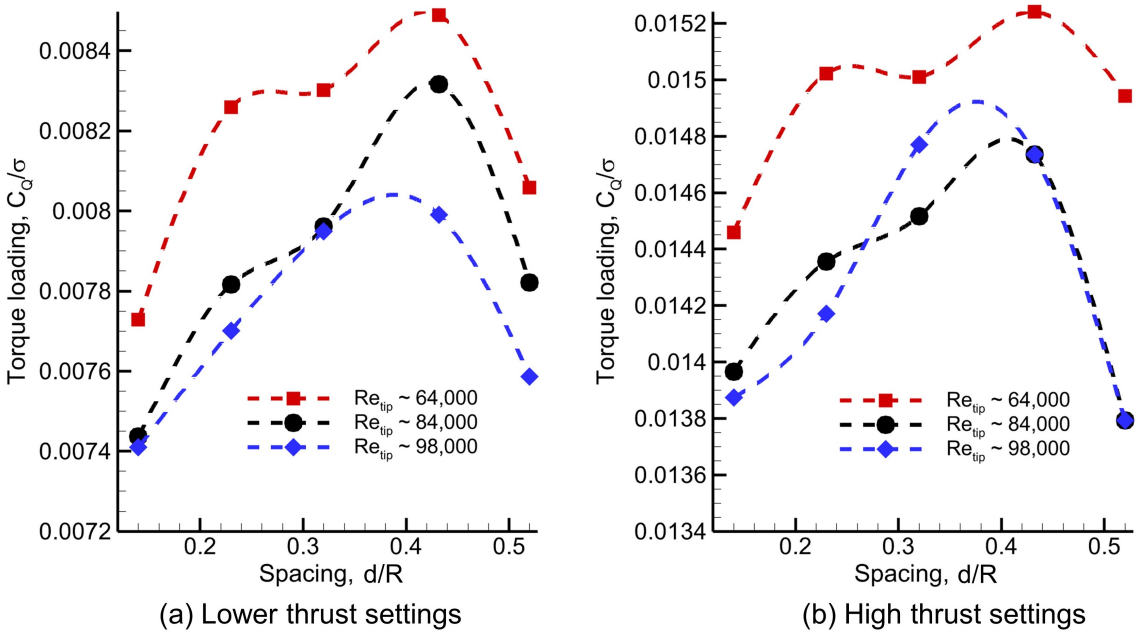

Figure 3.7: Change in torque coefficient of the upper rotor with respect to axial separation distance, (a)At low thrust conditions with a collective pitch of upper rotor at 6°, (b)At high thrust conditions with a collective pitch of upper rotor at 10°.

Blade Element Momentum Theory (BEMT) was used by Ramasamy [6] to explain the increasing and decreasing trend of the lower and upper rotor performance, respectively, with decreasing axial separation distance. The BEMT assumes that each blade section acts as a quasi-2D airfoil to produce sectional aerodynamic forces and moments [73]. The schematic

representation of the sectional blade profile with the incident velocities and associated flow angles are shown in Fig. 1.8 where U is the resultant velocity at the blade element, ϕ is the inflow angle and, dL and dD are lift and drag per unit span. U is given as:

$$U = \sqrt{{U_T}^2 + {U_P}^2} \tag{3.1}$$

where U_T is the velocity component tangential to the tip path plane due to blade rotation and U_P is the velocity component normal to the tip path plane due to induced inflow. ϕ is given as:

$$\alpha = \theta_\circ - \phi \qquad \text{where} \qquad \phi = \tan^{-1}\left(\frac{U_P}{U_T}\right) \approx \frac{U_P}{U_T} \text{ for small angle} \tag{3.2}$$

The effective angle of attack, α, then defines the sectional lift and drag force as

$$dL = \frac{1}{2}\rho U^2 c C_l(\alpha) dy \qquad\qquad dD = \frac{1}{2}\rho U^2 c C_d(\alpha) dy \tag{3.3}$$

With reducing axial separation distance, the lower rotor induces higher inflow (U_P) on the upper rotor, which reduces the effective angle of attack of the upper rotor (α). Thus, the upper rotor lift (and hence, upper rotor thrust) decreases, and the induced upper rotor torque increases for a fixed collective pitch ($\theta_\circ$)—the reduction in the upper rotor thrust results in reduced downwash velocity. The decrease in the downwash velocity implies that the induced angle of the lower rotor is reduced, and the effective angle of attack increases. As such, the lower rotor thrust increases with reduced induced torque for a fixed collective pitch.

The non-linear variations in upper rotor torque at different rotor spacings, as depicted in Fig. 3.7a, provide valuable insights into the rotor performance. Initially, there is an increase in torque from a spacing of $d/R = 0.52$ to $d/R = 0.432$, consistent with Blade Element Momentum Theory (BEMT). However, as the axial separation distance falls below $d/R = 0.432$, a decrease in torque exerted by the upper rotor is observed. This intriguing behavior can be attributed to the torque-matched trim condition established between the upper and lower rotors in this study. To achieve this trim condition, the collective pitch of the upper rotor was set as a constant, and the collective pitch of the lower rotor was adjusted to match the

torque with that of the upper rotor. Consequently, as the rotor spacing decreased, the collective pitch of the lower rotor was reduced to minimize the induced inflow on the upper rotor, as evidenced in Fig. 3.5a, b, and c, where the lower rotor's thrust decreased within the spacing range of $d/R = 0.23$ to $d/R = 0.14$. As the lower rotor's collective pitch (and, by extension, its thrust) decreased, the induced inflow on the upper rotor also decreased, ultimately leading to the observed torque reduction in the upper rotor as the axial separation distance decreased. This complex interplay between rotor spacing, collective pitch adjustments, and induced inflow highlights the intricate dynamics of coaxial rotor systems.

Performance characterization of the rotor at high thrust settings

The upper rotor was set at a collective pitch of $10°$, corresponding to the average C_T of 0.0068 at single rotor configuration for the three given Re_{tip}. The collective pitch of the lower rotor was varied to match the torque between the two rotors. The spacing was changed from $d/R = 0.52$ to $d/R = 0.14$, and the results are summarized in C_T vs. C_Q plots in Fig. 3.8 and C_T vs. FM plots in Fig. 3.9. Like the low thrust conditions, the upper rotor performance decreased while the lower rotor increased with reducing axial separation distance.

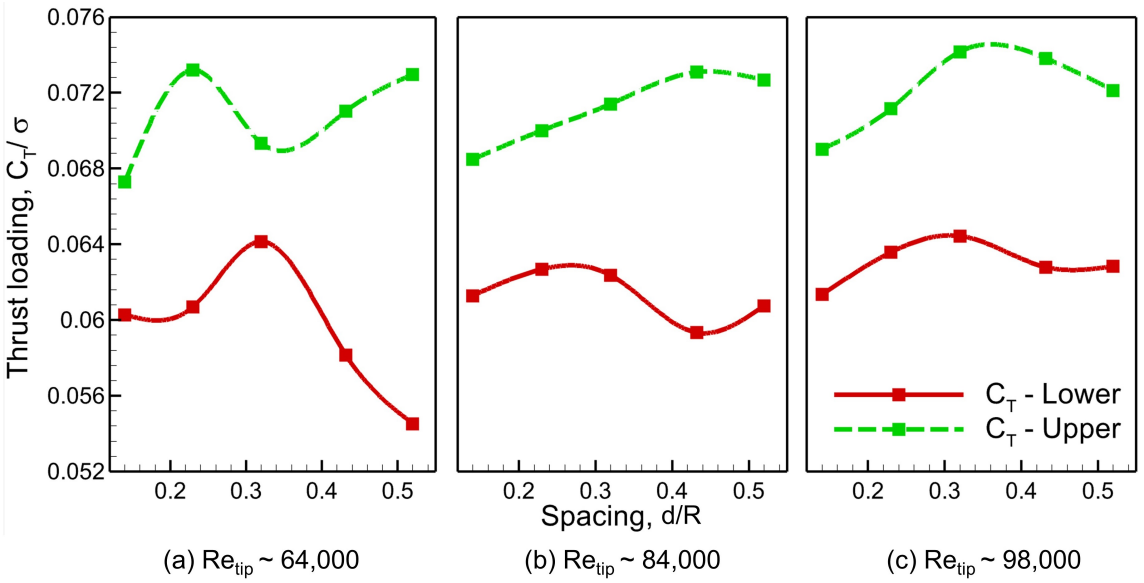

Figure 3.8: Variation of thrust coefficient, C_T with respect to axial separation distance at high thrust settings, (a) Re_{tip} 64000, (b)Re_{tip} 84000, (c) Re_{tip} 98000

For the case with $Re_{tip} = 64,000$, changing the axial separation distance from $d/R = 0.52$ to $d/R = 0.32$ increased the performance of the lower rotor. Subsequently, a decrease in performance was observed for the spacing of $0.23R$, followed by another increase for the spacing of $d/R = 0.14$. Conversely, a similar but mirrored trend was observed for the upper rotor at this thrust setting and $Re_{tip} = 64000$. In contrast, the lower rotor's performance increased for higher Re_{tip} values of 84000 and 98000, while that of the upper rotor gradually decreased as the axial separation distance was reduced. Specifically, the figure of merit (FM) for the lower rotor decreased by 8.4% for the case with $Re_{tip} = 84000$ and by 4.3% for the case with $Re_{tip} = 98000$ when the spacing was reduced from $d/R = 0.52$ to $d/R = 0.14$. Furthermore, the performance trend observed for the lower rotor exhibited more similarities between the cases with Re_{tip} values of 84,000 and 98,000 compared to that of the $Re_{tip} = 64000$ case. This result is consistent with the observation made for low thrust setting.

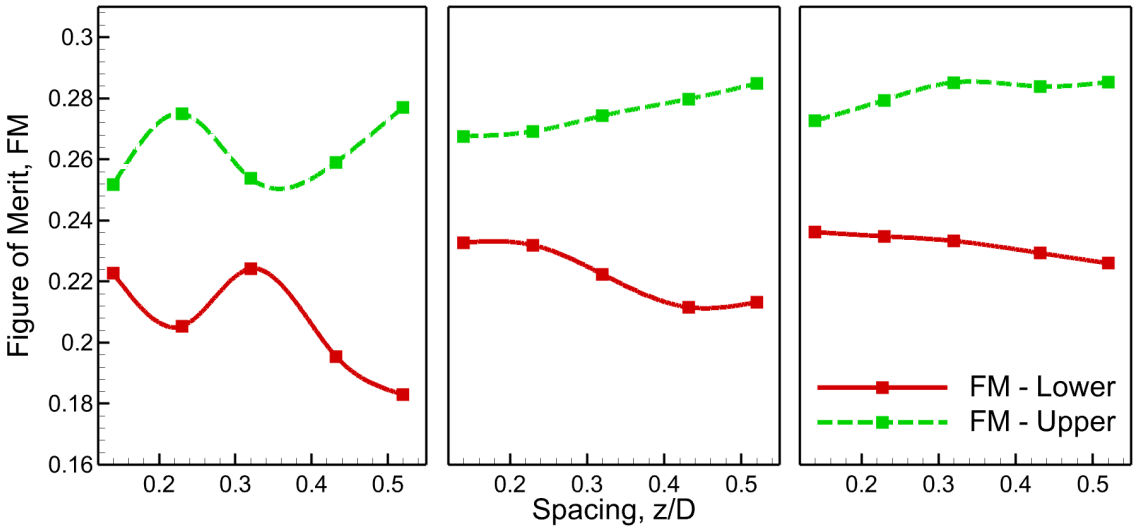

Figure 3.9: Variation of Figure of Merit, FM with respect to axial separation distance at high thrust settings, (a) Re_{tip} 64000, (b)Re_{tip} 84000, (c) Re_{tip} 98000

The performance of the upper rotor exhibited a consistent gradual decrease in FM when the rotor spacing was reduced, for Re_{tip} values of 84000 and 98000. This trend was more pronounced and similar between the cases with Re_{tip} of 84000 and 98000 compared to that with $Re_{tip} = 64,000$. Specifically, a reduction in FM of 6% and 4.4% was observed for the upper rotor for cases with Re_{tip} of 84000 and 98000, respectively, when the spacing was decreased from $d/R = 0.52$ to $d/R = 0.14$.

Notably, for low thrust conditions, the FM exhibited a slight increase for the upper rotor within the spacing range of $d/R = 0.52$ to $d/R = 0.432$, a trend not observed for higher thrust settings. However, the variation in torque (C_Q) with respect to axial separation distance for higher thrust conditions suggested that the upper rotor's torque followed a trend similar to that of low thrust conditions. Initially, the torque increased for spacing from $d/R = 0.52$ to $d/R = 0.432$ and gradually decreased with a further reduction in axial separation distance. This behavior is attributed to the imposed torque-matched trim condition, as discussed in the previous section.

3.4.4 Time-averaged flowfield study

After the performance characterization of the rotors, the time-averaged and temporal characteristics of the CCR and single rotor were characterized. The single and CCR flowfields were averaged over 30 rotor revolutions for the time average study. Fig. 3.10a shows the time average flowfield for the CCR with rotor spacing of d/R = 0.14. The radial and axial distances were normalized using the rotor diameter (D), and the velocities were normalized using the hover-induced velocity calculated for C_T of 0.006, which is given by:

$$V_h = D\Omega\sqrt{\frac{C_T}{8}} \tag{3.4}$$

The rotor rotational axis of the lower rotor was taken as the reference center for normalizing the distances. The black solid line in Fig. 3.10a represents the two rotor planes. The time-averaged inflow was extracted from the time-averaged velocity field to study the effect of rotor spacing on the inflow velocity. The velocity distribution was studied at the axial location of $0.02D$ below the rotor plane for both the upper and lower rotor, represented by the red dashed line in Fig. 3.10a. The inflow velocities below the upper and lower rotor are illustrated in Fig. 3.10b & c. The inflow distribution below the rotor plane for the single rotor, as seen in Fig. 3.10b, exhibits triangular distribution with axial velocity increasing with the radial distance. A similar observation for the inflow distribution was made by Shukla [30] in his studies of multi-rotors operating at low Reynolds numbers. The axial velocity was observed to quickly reduce to zero

near the tip due to the tip effects. The inflow velocity distribution observed in the current study is atypical to the sectional blade loading distribution for untwisted blade geometry ([74]).

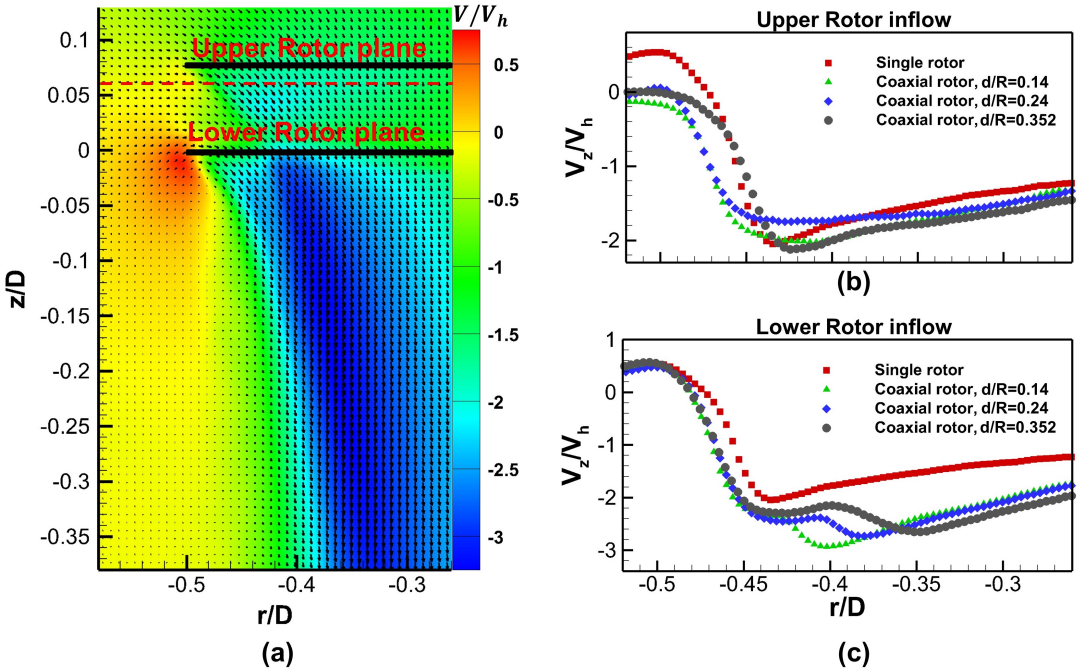

Figure 3.10: a. Time-averaged velocity field for coaxial rotor with rotor spacing $d/R = 0.14$, b. Inflow velocity for the upper rotor, c. Inflow velocity for the lower rotor.

Upper rotor inflow: The inflow velocity distribution for the upper rotor at different rotor spacings was compared with that of the single rotor as illustrated in Fig. 3.10b. Although the magnitude of the peak axial velocities was observed to be different for single and coaxial rotor configurations, the variation in the overall inflow (integrated over the span of the blade) was quantified (and summarized in Table 3.2) to understand the effects of the lower rotor on the upper rotor. The overall inflow for a single rotor had the lowest value when compared to any of the coaxial rotor configurations, with overall inflow increasing by 13% for larger rotor spacing (0.176D and 0.12D) and by 20% for smaller rotor spacing (0.07D). It is to be noted that both rotors were operating in thrust-matched conditions ($C_T = 0.006$). Thus, it would be expected that the sectional integration of the inflow velocity for all the cases is equal as given by the Blade Element Momentum Theory (BEMT) for a single rotor (Johnson [74]) given by the Eq. 3.5 below:

$$C_{T_{BEMT}} = \int 4F\lambda(r)^2 r dr \tag{3.5}$$

Table 3.2: Radial integration of the inflow velocity for the upper rotor

Rotor configuration	Integrated inflow
Single	-0.3096
Coaxial, d/R = 0.352	-0.3570
Coaxial, d/R = 0.24	-0.3554
Coaxial, d/R = 0.14	-0.389

where F is the Prandtl tip-loss function and λ is the non-dimensional inflow velocity. However, the BEMT model does not account for the additional inflow that the upper rotor experiences due to the presence of the lower rotor. Compared to the single-rotor configuration, the upper rotor in the coaxial configuration requires higher power to produce the same thrust. The torque coefficient, as given by BEMT, is shown by the equation below:

$$C_{Q_{BEMT}} = \int \lambda(r) dC_T \tag{3.6}$$

The above equation suggests that for the same thrust condition, the coaxial upper rotor's inflow velocity should be higher than the single rotor (agreeing with the PIV measurements), especially because the torque for the coaxial upper rotor is higher. Table 3.2 shows that the integrated inflow for the coaxial rotor at rotor spacing of 0.07D is higher when compared to that of 0.12D and 0.176D. This is not surprising; as the axial separation distance between the rotors reduces, the influence of the lower rotor on the upper increases.

Lower rotor inflow: The inflow velocity distribution below the lower rotor at different rotor spacing was also compared with that of the single rotor shown in Fig. 3.10c. The lower rotor is operating under the inflow of the upper rotor, which reduces the performance of the lower rotor [6]. Thus, the wake below the lower rotor consists of the inflow from both the upper and the lower rotor. The influence of the upper rotor and the rotor spacing was apparent in the inflow velocity distribution below the lower rotor, with inflow velocity being higher for the lower rotor than that of the single rotor configuration (Fig. 3.10c). As opposed to the single rotor velocity distribution, which only had one peak, the velocity distribution for the coaxial lower rotor was observed to have two peaks. Although the second velocity peak in the inflow distribution was observed around the same radial location of 0.44D for both single and coaxial

lower rotors, the location of the first velocity peak with respect to the rotor rotational axis varied. Since the upper rotor wake contracts before it impinges on the lower rotor plane with the contraction ratio dependent on the rotor spacing, the additional peak observed in the inflow velocity distribution at the lower rotor plane is due to the upper rotor inflow. These observations from the flowfield study clearly demonstrate that the current results are on par with the literature and corroborate well with the blade element momentum theory.

3.5 Chapter summary

The motivation of this study was to validate the rotors used in the aerodynamic coaxial rotor thrust stand for conducting a scientific investigation of CCR performance. The lift and drag characteristics of the rotor blade were studied in a wind tunnel and were compared with the literature. Flow visualization was also carried out to substantiate the airload measurements. The hover performance characteristics of the individual rotors were also measured under out-of-ground conditions for varying collective pitch at different Reynolds numbers. The current rotor performance was compared with the literature. The performance of the CCR was also carried out by varying the axial separation distance at three Reynolds numbers for high and low thrust loading conditions. Time-averaged and instantaneous data analysis was carried out to study the characteristics of the rotors in CCR configuration. The near-wake flowfield characteristics of the CCR were also measured and compared with the literature.

The findings from this study are summarized below:

1. The current blades stalled at an angle of attack of 8° at the Reynolds number of 46,000, as evident from the wind tunnel experiments. The rotors also showed stall characteristics at a collective pitch of around 8°.

2. The overall performance of the upper rotor in CCR was reduced. In contrast, that of the lower rotor in CCR increased with the reduction in the rotor spacing, consistent with the observations made in the literature.

3. Time-averaged flow measurements showed that the upper rotor required higher torque to produce the same thrust as the single rotor. The torque requirement increased with reducing rotor spacing.

4. The observations show that the current results are on par with the literature and confirm the efficacy of the aerodynamic coaxial rotor thrust stand to conduct further studies.

Chapter 4

Performance characteristics of counter-rotating coaxial rotors hovering in ground effect

Aim 1 of this dissertation focuses on quantifying the performance characteristics of the counter-rotating coaxial rotor (CCR) and its rotors when operating in in-ground effect (IGE) conditions. The performance of CCR and its rotors in IGE is dictated by two major effects: rotor-on-rotor interactions and rotor-ground interactions. The literature on single rotors in IGE shows that the rotor-ground interactions improve the rotor performance, with the effect increasing with closer ground proximity. This is attributed to the reduction in the rotor-induced inflow due to ground effects resulting in improved rotor performance. Similarly, the rotor-on-rotor interactions reduce the rotor performance as the rotors induce additional inflow onto each other. The presence of these two competitive effects could result in CCR experiencing reduced improvement in its performance when compared to the single rotor. This chapter presents a parametric study on the performance characteristics of CCR when hovering in ground proximity.

4.1 Objectives

The competitive effects of rotor-on-rotor interactions vs. rotor-ground interactions on the CCR performance during IGE operation are studied through the following objectives:

1. Quantify the competitive influence of rotor-on-rotor interactions and rotor-ground interactions on the performance of the CCR and its rotors.
2. Compare the CCR performance with the isolated single rotor operating at similar thrust and IGE conditions.

4.2 Approach

The IGE effects on the CCR performance in hover were studied by varying the axial distance between the CCR and the ground plane, referred to as rotor heights. The experiments were carried out using the aerodynamic coaxial rotor thrust stand (Section 2.2), where thrust and torque produced by individual rotors were measured. The literature on CCR in out-of-ground (OGE) conditions has shown that the interactional effects between the upper and lower rotor strongly depend on the rotor spacing [6]. As such, the axial spacing between the two rotors was also varied. As a control case, the IGE characteristics of a single rotor were also measured and compared with those of the CCR and its individual rotors. These comparisons provided insights into the effects of aerodynamic interactions on CCR performance in IGE compared to that of a single rotor.

Experiments were carried out in untrimmed and trimmed conditions. Untrimmed experiments emulate the single rotor fixed-collective experimental condition [38]. Here, the upper and lower rotors in CCR were set to a torque-matched trim condition in OGE by varying the rotor collectives. Then, the collective pitch of the rotors was held constant, and the distance between the rotors and the ground plane was reduced. As the collective pitch of the rotors did not change, the variation in the rotor performance was mainly due to the change in induced angles. As such, this experimental setting provided insights into the change in induced effects at different rotor heights.

For trimmed experiments, the total thrust of the CCR system is held constant, in addition to matching the upper and lower rotor torques for all rotor heights by adjusting the rotor collective pitch. While the untrimmed conditions provide insights into the change in induced effects in IGE, the total thrust of the CCR also changes, resulting in modification of the aerodynamic environment at different rotor heights. Holding the total CCR thrust constant ensures that the changes in the rotor-on-rotor interactions are due to the IGE effects and not because of the change in rotor thrust conditions. The coupled analysis of the results from the untrimmed and trimmed conditions provides an overall understanding of the CCR performance behavior in IGE conditions.

The effects of rotor-on-rotor interactions on CCR individual rotor performance were quantified by conducting thrust-matched single-rotor experiments. Here, the single rotor was placed at the rotor height and trimmed to produce the same thrust as the CCR upper rotor. The difference in torque requirement to produce the same thrust between the upper rotor in CCR and a single rotor provided the quantitative measure of the rotor-on-rotor interactions in IGE.

4.3 Operating conditions

The influence of IGE conditions was studied for CCR at tip Reynolds number of $Re_{tip} = \Omega Rc/\nu \sim 1.52 \times 10^5$ and tip Mach number of $M_{tip} \sim 0.19$ at ambient room temperature ($T_a = 293K$) corresponding to a rotor operating speed of 1,500 RPM. The IGE conditions were achieved using the square, smooth, plane ground of side length $4.36R$ such that the rotor axis passed through the center of the square. The square ground itself was at an elevated position from the actual laboratory ground. The experimental arrangement has schematically shown in Fig. 4.1a. The CCR lower rotor was placed at the rotor height of $(z/R)_l = z/R$ above the ground plane, and the upper rotor was placed at the distance of d/R above the lower rotor resulting in the rotor height for the upper rotor of $(z/R)_u = z/R + d/R$. Similarly, the normalized rotor height for CCR has been defined as $(z/R)_{CCR}$ which is the distance between the ground plane and the center between the CCR upper and lower rotor (Fig. 4.1a) and is given as $(z/R)_{CCR} = z/R + 0.5d/R$.

The rotor height conditions for the current study have been varied between $z/R = 0.82 - 3.16$ (summarized in Table 4.1). The current experimental set-up allowed the highest ground height of $z/R = 3.16$. This was assumed to be sufficient to be considered an OGE condition. This is a reasonable approximation since it has been reported in Leishman [73] that the effects of the ground plane are negligible for rotor height greater than three rotor radii. Furthermore, analytical models such as Cheesemann & Bennett [43] and Hayden [45] show that the difference in rotor thrust for constant torque between the rotor height of $z/R = 3$ and a nominally larger value of $z/R = 8$ is 0.6% and 1.4% respectively. The observed differences are within the expected experimental error, and thus, the rotor height of $z/R = 3.16$ is acceptable as OGE for this study.

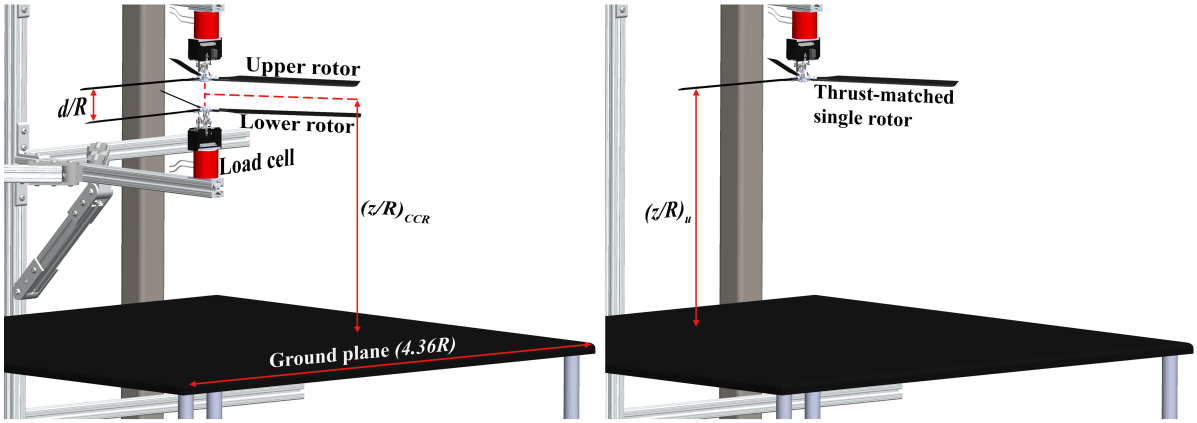

(a) (b)

Figure 4.1: Schematic of the experimental setup (a) CCR system, (b) Single rotor at same effective height and thrust-matched with the CCR upper rotor.

The axial spacing between the upper and lower rotor was varied to study the effects of rotor-to-rotor interactions and their combined interactions with the ground plane. Two axial spacing conditions were chosen as $d/R = 0.14$, similar to Sikorsky X2 technology demonstrator [6], and a higher value of $d/R = 0.34$, representative of a larger coaxial helicopter. The experiments for both rotor spacing were carried out under untrimmed and trimmed conditions similar to the single rotor tests. These experimental conditions differ from McAlister's [26] case where only torque-match trim condition between the upper and lower rotor was imposed at different rotor heights by adjusting the lower rotor collective for a fixed upper rotor collective. As a result, the total thrust of the CCR varied with the change in rotor height during McAlister's [26] experiments.

For the current study, trimmed experiments were carried out to maintain the same total CCR thrust ($C_T = 0.0081$) at all rotor heights while also matching the torque between the upper and lower rotor by adjusting the rotor collective pitch. Maintaining constant CCR total thrust ensures a similar aerodynamic environment between the rotors at different rotor heights, providing better insights into the interactional aerodynamics between the CCR individual rotors. Similarly, untrimmed experiments were conducted by fixing the collective pitch for both rotors corresponding to the OGE torque-balance trim at $C_T = 0.0081$. In this case, the torque balance trim condition was not imposed, and the thrust was allowed to increase due to IGE,

similar to an untrimmed single rotor. With this combination of untrimmed and trimmed experiments, this study aims to provide a comprehensive, physics-based understanding of the CCR behavior in IGE.

Table 4.1: Summary of the operating conditions for the IGE experiments

Condition	Configuration	d/R	Rotor height	z/R	Thrust-matched single rotor
Untrimmed	Single	-	Single = z/R	0.82, 1.03, 1.3, 1.56, 1.76, 1.92, 3.16	
	Coaxial	0.14, 0.34	Lower, $(z/R)_l = z/R$		
Trimmed	Single	-	Upper, $(z/R)_u = z/R + d/R$		$0.82 + d/R$
	Coaxial	0.14, 0.34	$(z/R)_{CCR} = z/R + 0.5d/R$		$3.16 + d/R$

Single rotor experiments were carried out for untrimmed and trimmed conditions as a control case to compare IGE performance with the CCR and its individual rotors. Since the single rotor's solidity is half that of the CCR, the single rotor was set at the same blade loading ($C_T/\sigma = 0.046$) as that of the CCR to facilitate the performance comparison between rotors of different solidity [73]. For the trimmed experiments, the rotor thrust was set to $C_T = 0.00405$. The collective pitch was held constant at the OGE trimmed value for the untrimmed experiments. The rotor height was varied between $z/R = 3.16$ and $z/R = 0.82$, similar to the lower rotor in CCR.

Additional single-rotor experiments were also carried out to understand better the interaction of the lower rotor on the upper rotor. This was done by setting the single rotor at the same height from the ground and trimming it to the same thrust as the upper rotor in the CCR configuration as illustrated in Fig. 4.1b. These experiments were performed at the extreme rotor heights: one closest to the ground and the other farthest, corresponding to OGE. The upper rotor position differed for the two rotor separation cases, corresponding to $z/R + d/R$. These experiments used torque measurements to understand the influence of the lower rotor on the upper rotor during IGE operations.

The experiments for each condition summarized in Table 4.1 were performed six times to ensure repeatability. The tests were performed as two sets of three instances, with a two-week interval between the sets. During each set, the system was shut down for 15 minutes and reset before repeating each experiment. A similar procedure was repeated after two weeks for the

second set of experiments. All the results presented in this paper have been averaged over these six runs, with the symbols in the plot denoting the mean value and the error bar denoting the standard deviation across these six runs.

4.4 Results and Discussion

First, the performance of the single rotor under OGE and IGE is presented. Second, the performance behavior of the CCR under untrimmed and trimmed conditions during IGE operation is evaluated and compared with the single rotor. Third, the discussion on the performance of the CCR individual rotors under untrimmed and trimmed conditions is presented. For all these discussions, the influence of rotor spacing on the performance of the CCR and individual rotors is also assessed.

4.4.1 Single rotor performance

For a baseline comparison, the performance of a single rotor was quantified in OGE by varying the rotor collective pitch from $\theta_\circ = 0^\circ$ to $\theta_\circ = 10^\circ$. The currently available power supply limited the settings for the maximum collective pitch to $\theta_\circ = 10^\circ$ for the rotor RPM of 1500. Similarly, the performance of the single rotor was also measured during IGE operations for both untrimmed and trimmed cases. These results are shown in two forms in Fig. 4.2. Figure. 4.2a shows the FM as a function of rotor thrust, and Fig. 4.2b shows the FM as a function of rotor height from the ground starting from the OGE case with $\theta_\circ = 6.2^\circ$ and $C_T = 0.00405$. The collective pitch was held constant for the untrimmed case, whereas for the trimmed case, the collective pitch was adjusted to maintain a constant thrust coefficient.

Equation 2.3 can provide insight into the observed FM behavior in Fig. 4.2a. The total rotor torque, C_Q, comprises induced torque (due to lift/thrust) and profile torque (due to drag). The profile torque is nearly constant at lower collectives, similar to the airfoil drag at low angles of attack, whereas the induced torque increases somewhat linearly. As a result, the FM increases monotonically at low thrusts and appears to reach a maximum at the highest thrust value, in this case at $\theta_\circ = 10^\circ$. If the collective increases, the FM will decrease as parts of the rotor blade sections experience stall.

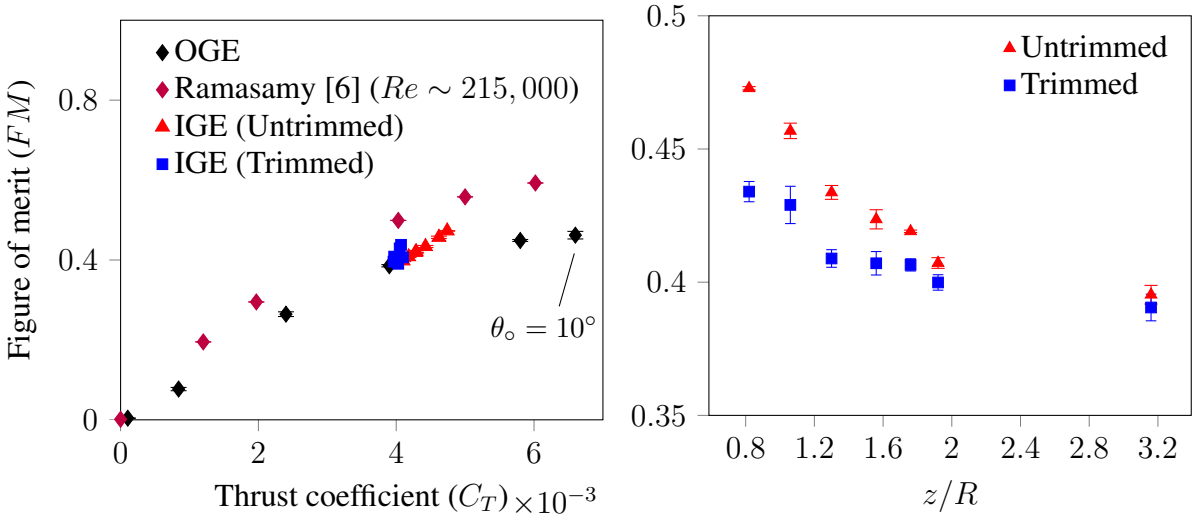

(a) FM variation at different thrust conditions

(b) FM variation at different rotor heights

Figure 4.2: Single rotor baseline performance.

The current rotor behavior resembles the three-bladed rotor used by Ramasamy [6] for his coaxial rotor studies. However, the rotors used by Ramasamy [6] had higher performance than the current rotors. The differences can be attributed to the difference in the tip Reynolds number between the two studies. The Reynolds number for the current study was set to $Re_{tip} = 150,000$, while for Ramasamy's case, it was set to $Re_{tip} \sim 215,000$. The lower Reynolds number for the current case could result in higher profile drag and lower rotor performance compared to Ramasamy's case. The measurements also suggest that the rotor does not exhibit stall characteristics until $\theta_\circ = 10°$. Thus, the IGE investigation was conducted at lower collective values to avoid stall effects on rotor performance.

Similarly, the rotor FM variation with the rotor height (Fig. 4.2b) showed that the rotor performance increased with a reduction in rotor height, which is attributed to the reduced rotor inflow due to ground proximity. The reduction in the rotor inflow in IGE results from modifications in the rotor wake and tip vortex characteristics due to the proximity of the ground. Light [41], in his experiments, showed that the axial vortex spacing in IGE is larger compared to OGE case (Fig. 4.3), which resulted in reduced induced inflow at the rotor plane in IGE. The effects of this reduction in induced rotor inflow on the rotor performance can be explained using Blade Element Theory (BET) as discussed in Section 3.4.3.

As evident from the formulation, reducing induced inflow due to the proximity of the ground plane will increase the blade sectional effective angle of attack for a fixed rotor collective. Consequently, the blade sectional lift increases and results in increased rotor thrust under similar torque conditions, which explains the observed improvement in single rotor performance under IGE for untrimmed (fixed-collective) conditions (Fig. 4.2b).

Similarly, for the trimmed case, the torque required to produce the same thrust will reduce due to the reduction in rotor inflow, which results in the observed rotor performance improvement (Fig. 4.2b). The differences in the rotor inherent characteristics for untrimmed and trimmed cases are also highlighted in Fig. 4.2a. Here, the thrust and figure of merit for the single rotor increased for the IGE untrimmed case. As the collective pitch for the untrimmed conditions is held constant, the ground effects reduce the rotor inflow and increase the rotor's effective angle of attack, resulting in increased rotor thrust and figure of merit.

On the other hand, only the rotor figure of merit increased for the trimmed IGE case because the collective pitch of the rotors was reduced to maintain the constant total thrust. In addition, the single rotor under trimmed conditions was observed to under-perform (lower FM) compared to the untrimmed case. This is primarily due to the imposed trim condition where the collective pitch angle of the rotor is decreased as the rotor height is reduced, resulting in rotors operating at a lower lift-to-drag ratio.

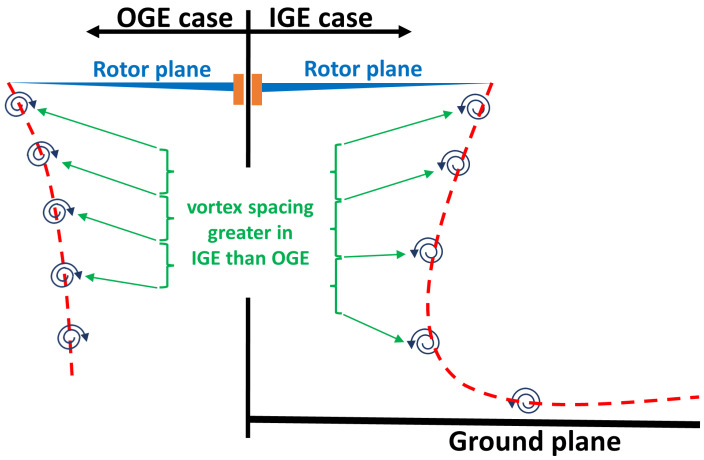

Figure 4.3: Schematic representation of conceptual flowfield comparison between OGE and IGE case.

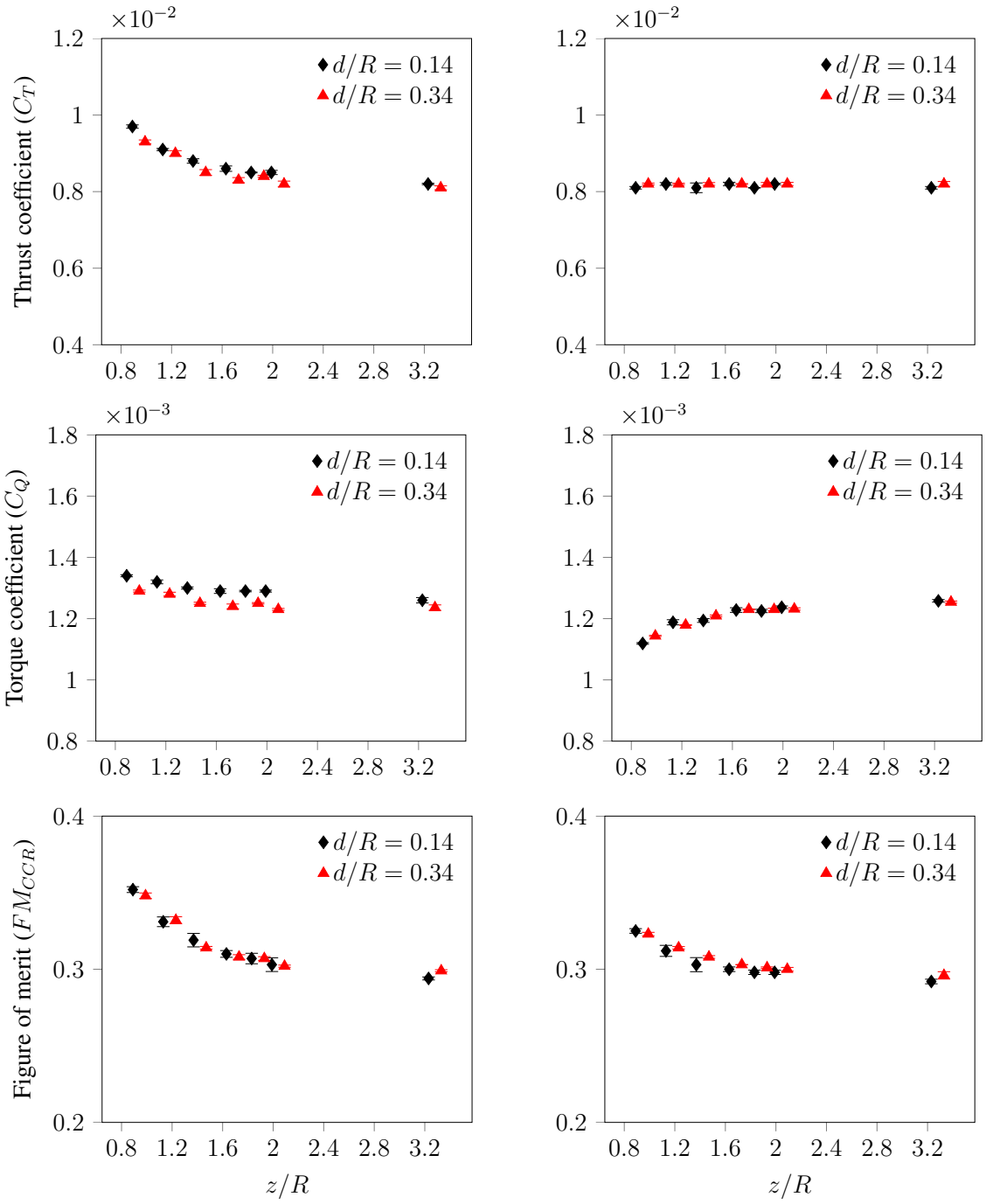

(a) Untrimmed

(b) Trimmed

Figure 4.4: Thrust coefficient, torque coefficient, and figure of merit variation for CCR with CCR rotor height ($(z/R)_{CCR}$).

4.4.2 Counter-rotating coaxial rotor performance

The variation of total CCR thrust and torque with rotor height under untrimmed and trimmed conditions for both rotor spacing of $d/R = 0.14$ & 0.34 is summarized in Fig. 4.4a and 4.4b

respectively. For the trimmed case, the total thrust of the CCR was held constant at $C_T = 0.0081$, and the torque was matched between the upper and lower rotor for all rotor heights and both rotor spacing by trimming the collective pitch angle of the rotors as summarized in Fig. 4.5. Similarly, for the untrimmed case, the total CCR thrust was set at $C_T = 0.0081$, rotors were torque matched at OGE, and rotor height was reduced while maintaining the constant collective pitch of both rotors.

The untrimmed results showed that the total thrust and torque of the CCR for both rotor spacing increased with the reduction in rotor height. However, closest to the ground, the effective increase in torque of 6.4% relative to OGE (in this case $(z/R)_{CCR} = 3.23$) was noticeably lower than that for the CCR thrust (18.2%), suggesting a performance benefit in-ground effect. A similar observation has been reported by Lim [32] where the CCR torque increased for rotor height $(z/R)_{CCR} \lesssim 1.2$. The increase in CCR thrust with reduction of rotor height is expected as the proximity of the ground plane reduces the inflow experienced by the rotors, increasing the rotor thrust for the same collective pitch similar to the single rotor (from BET discussed in Section 3.4.3).

The observed increase in CCR torque for the untrimmed conditions can be attributed to the rise in induced drag associated with increased blade sectional lift due to reduced rotor inflow. Similarly, the trimmed results showed that the torque required to produce the same CCR thrust was reduced at smaller rotor heights. As the IGE conditions reduce the rotor inflow, the collective pitch of the rotors is reduced to maintain the constant total thrust. Reducing rotor inflow also reduces the torque required to produce the same thrust that is observed currently.

The CCR performance was also quantified using the figure of merit (FM_{CCR} given by Equation 2.4) variation at all rotor heights for both rotor spacing of $d/R = 0.14$ & 0.34 under untrimmed and trimmed conditions (Fig. 4.4). Rotor spacing was observed to have minimal influence on FM_{CCR} variation with rotor height under both untrimmed and trimmed experimental conditions. Only the CCR torque for the untrimmed case shows a small effect of rotor spacing in IGE. As discussed by Ramasamy [6], the torque demand for coaxial rotors in out-of-ground effect (OGE) conditions tends to increase with smaller rotor spacing. This aligns with the observations made in the present study, where the torque requirements were higher for CCR

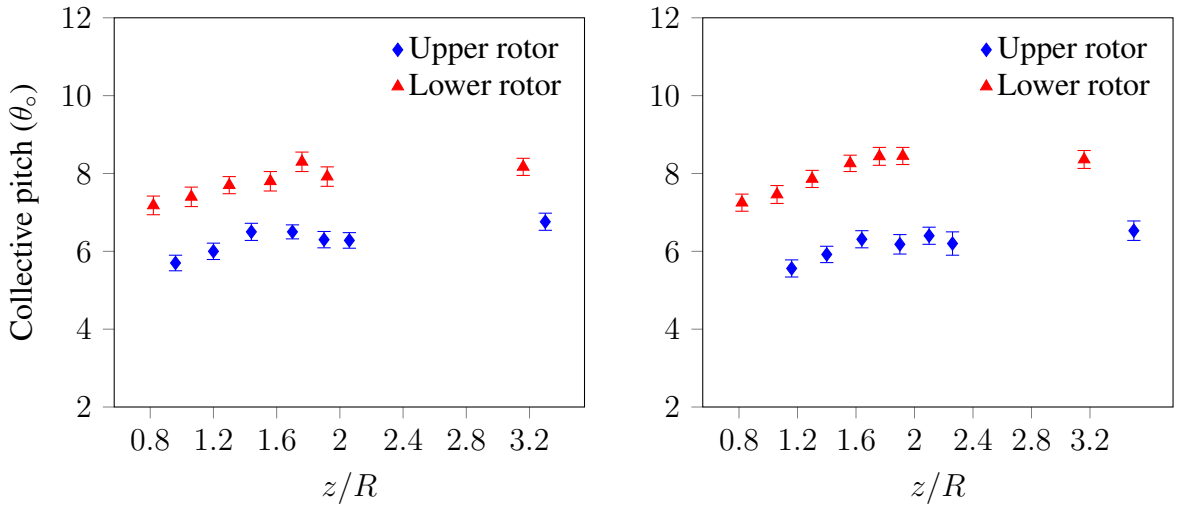

(a) $d/R = 0.14$ (b) $d/R = 0.34$

Figure 4.5: Collective angle for upper and lower rotor for trimmed CCR experiments. Average standard deviation is $\pm 0.22^\circ$.

with smaller spacing. This difference in torque was observed to persist under IGE conditions when the collective pitch of the CCR individual rotors was held constant under untrimmed cases.

Additionally, the CCR was observed to under-perform (lower FM) for the trimmed case when compared to that for untrimmed case (Fig. 4.4), which is primarily due to the imposed trim condition where the collective pitch angle of both the upper and lower rotor is decreased as the rotor height is reduced (Fig. 4.5). As discussed in the previous section, the constant thrust trim condition requires reducing the rotor collective pitch angle. This results in the blades operating at a lower lift-to-drag ratio, leading to a smaller rise in FM_{CCR}.

4.4.3 Comparison with a single rotor

A comparison of performance ratio (IGE-to-OGE) between a single rotor, the CCR, and its individual rotors along with Hayden's [45] empirical model for IGE as a reference is illustrated in Fig. 4.7 for untrimmed or fixed-collective conditions. Hayden's model is a semi-empirical model which gives the ratio (IGE-to-OGE) for the Figure of Merit as:

$$\frac{FM_{IGE}}{FM_{OGE}} = A + 2B\left(\frac{1}{z/R}\right)^2 \tag{4.1}$$

where A and B are empirical constants with values $A = 0.9926$, and $B = 0.0379$. The ratio (IGE-to-OGE) of Figure of Merit accounted for the net effect of IGE on the rotor performance since the ground proximity affects both the rotor thrust and torque for the untrimmed case. The performance ratio for both the single rotor and CCR at both rotor spacing followed Hayden's model closely. This further confirms the previous observation that the effects of rotor spacing on CCR performance under IGE are minimal.

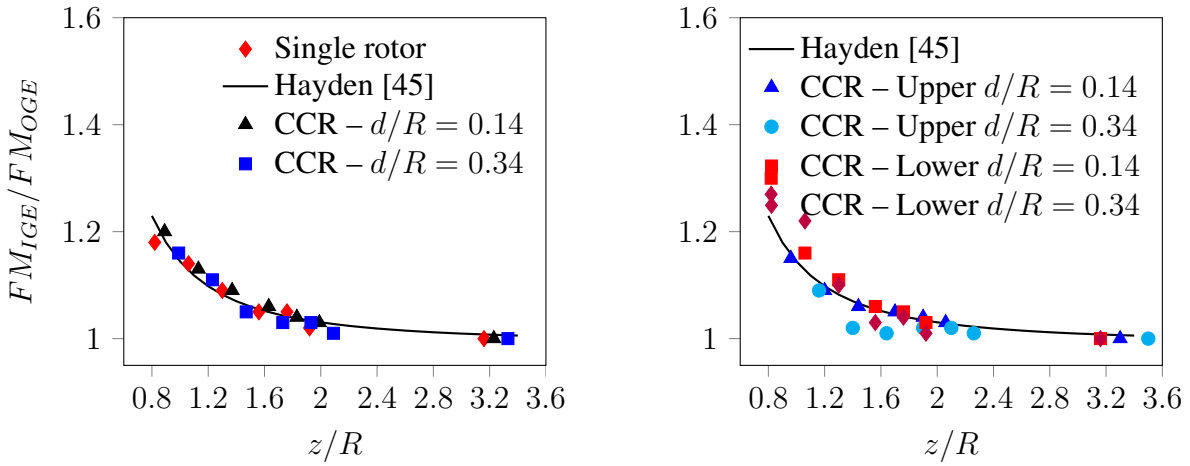

(a) CCR performance

(b) Individual rotor performance

Figure 4.6: Mean performance ratio (IGE-to-OGE) variation for CCR and its individual rotors with their effective height from the ground under untrimmed conditions.

However, the individual performance of the upper and lower rotor in the CCR shows some differences when compared to the single rotor, as seen in Fig. 4.6b. The lower rotor experienced larger gains in its performance than the single rotor for both rotor spacing, with the effect more pronounced at smaller rotor heights. On the other hand, the gain in the upper rotor performance ratio was less when compared to a single rotor for both rotor spacing, with the effect being more pronounced for the higher rotor spacing.

The results for the trimmed experimental conditions are also shown in Fig. 4.7b. As in the untrimmed case, the CCR was observed to follow a single rotor trend closely, and the effects of rotor spacing were not apparent. However, the ratio (IGE-to-OGE) of Figure of Merit for the trimmed case was lower than that predicted by Hayden's model. As discussed earlier, this is due to the imposed trim condition where the collective pitch of the rotors is reduced to maintain constant total thrust. The individual rotors also exhibited similar trends as those observed under

untrimmed conditions. The performance benefits for the lower rotor were larger than the single rotor, and the effects were pronounced with reduced rotor spacing. These results highlight the influence of rotor-to-rotor interactions on the performance of individual rotors of CCR during IGE operations, which has been further explored in the upcoming sections.

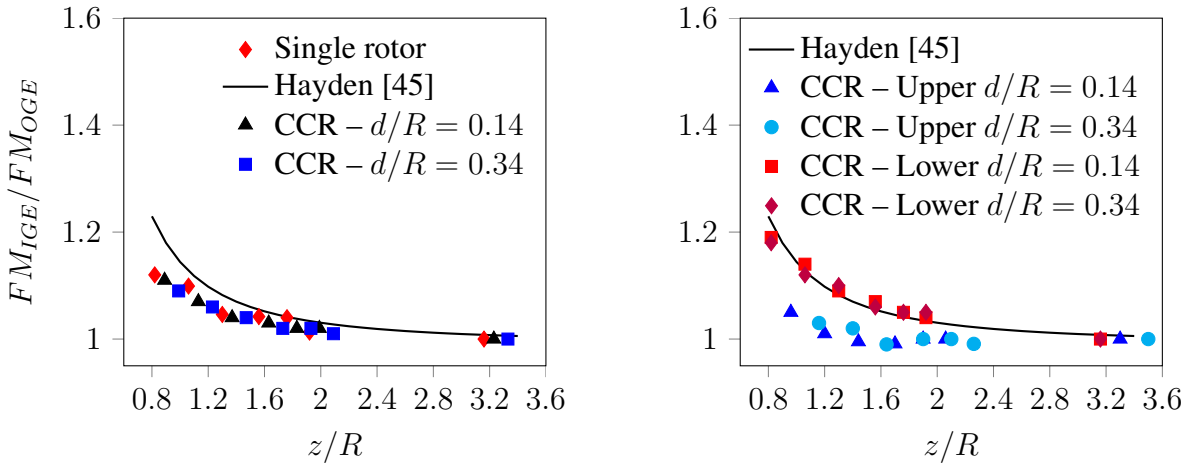

(a) CCR performance

(b) Individual rotor performance

Figure 4.7: Mean performance ratio (IGE-to-OGE) variation for CCR and its individual rotors with their effective height from the ground under trimmed conditions.

4.4.4 Individual rotor performance

This section quantifies upper and lower rotor performance in IGE for untrimmed and trimmed conditions. To decouple the rotor-to-rotor interactions during IGE operations, the influence of the lower rotor on the upper rotor is also quantified and discussed.

Effects of rotor spacing

The individual rotor thrust coefficient, torque coefficient, and figure of merit (FM) variation with respect to rotor height for the untrimmed and trimmed case is presented in Fig. 4.8. At OGE ($z/R = 3.16$), the upper rotor has a larger thrust share than the lower rotor for both untrimmed and trimmed conditions, and this observation has been well documented in the literature [32, 6]. As the rotor height was reduced, the FM of both the rotors for untrimmed and trimmed conditions was observed to increase with a reduction in rotor height due to the influence of the ground.

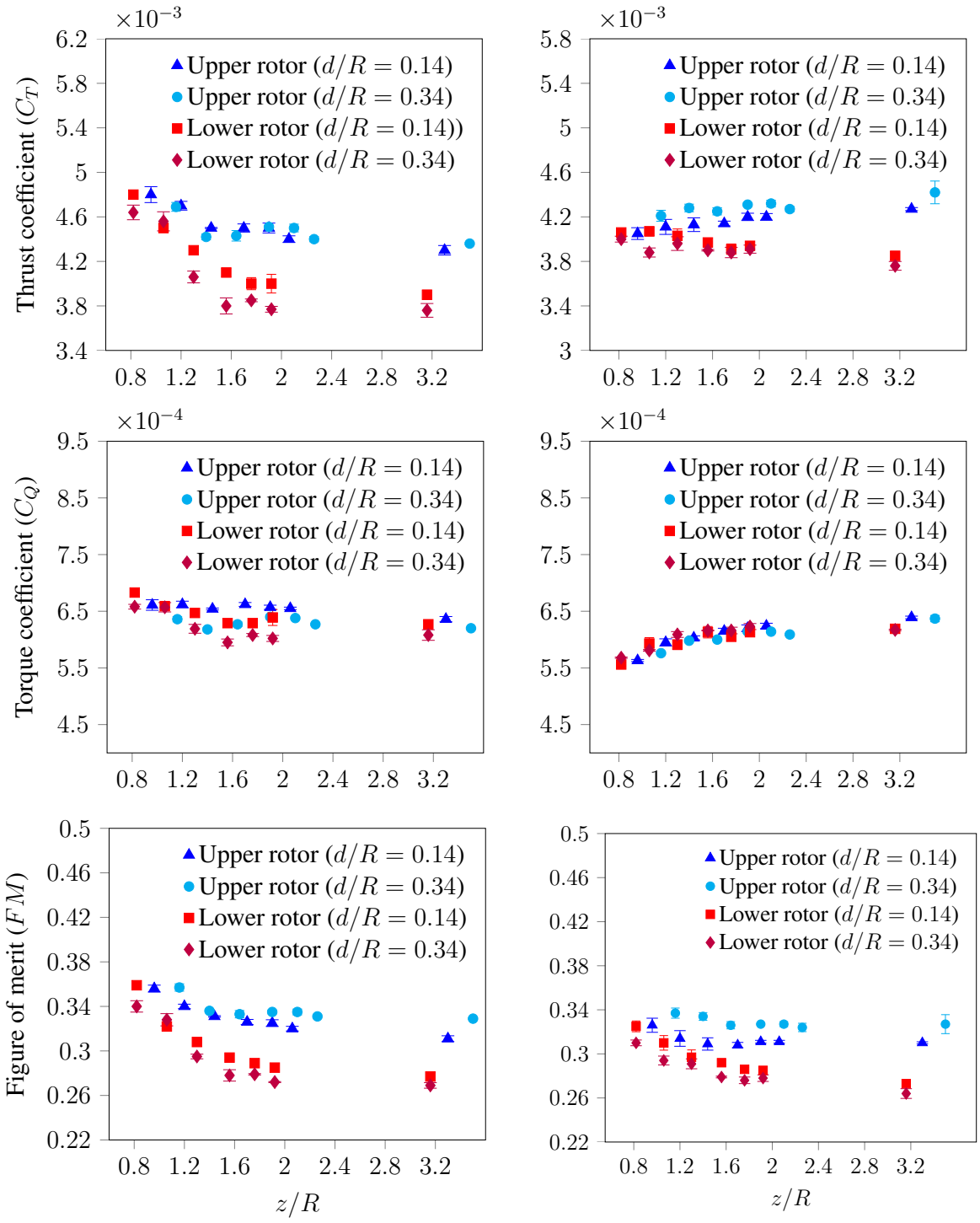

(a) Untrimmed

(b) Trimmed

Figure 4.8: Individual rotor C_T, C_Q, and FM plotted against their height from the ground.

The increase in thrust of the lower rotor with a reduction in rotor height was higher when compared to that of the upper rotor for the untrimmed conditions (Fig. 4.8a). This suggests that the ground has a larger effect on the lower rotor that could be partially attributable to its closer

proximity to the ground. At the same time, the effects of rotor-to-rotor interactions cannot be neglected, as highlighted by the untrimmed results for rotor spacing of $d/R = 0.14$, where the lower rotor showed significant improvement in its performance when its distance from the ground plane was $(z/R)_l \lesssim 1.8$ (Fig. 4.8a).

In contrast, significant improvement in the upper rotor performance was observed only when it was even closer to the ground $(z/R)_u \lesssim 1.44$ (Fig. 4.8a). At the larger rotor spacing of $d/R = 0.34$, a similar behavior was observed, with the lower rotor showing IGE performance improvements at larger heights above ground compared to the upper rotor. These observations suggest that the aerodynamic interactions between the lower and upper rotors are modified as the rotor height is reduced. For the untrimmed case, the total CCR thrust varied with the rotor height, influencing the aerodynamic interactions between the two rotors.

The behavior of individual rotors under trimmed conditions was investigated to further our understanding of CCR rotor-to-rotor interactional effects in IGE. The trimmed experiments showed that the lower rotor thrust increased while the upper rotor thrust decreased with the reduction in rotor height for both rotor spacing (Fig. 4.8b). This is partly because of the larger ground effect experienced by the lower rotor due to its proximity. This phenomenon can be further elucidated through a detailed examination using Blade Element Momentum Theory (BEMT). For a comprehensive understanding, the reader should refer to the accompanying flowchart in Fig. 4.9 for enhanced clarity.

As the lower rotor thrust increases, it induces a higher inflow onto the upper rotor. This results in reduced upper rotor thrust and increased torque requirement for the upper rotor. BEMT dictates that the reduction follows the reduction in the upper rotor thrust in the upper rotor inflow that impinges onto the lower rotor. Consequently, the lower rotor thrust increases even more, and the torque reduces. This cycle continues until equilibrium is reached. To impose the torque-matched trim constant at a constant total CCR thrust, the collective pitch of the lower rotor has to be increased, and that of the upper rotor has to be decreased. The effects get pronounced with the reduction in the rotor heights; thus, we see a decrease in the upper rotor thrust and an increase in the lower rotor thrust with the reduction in the rotor height. This ultimately results in a near-equivalent distribution of thrust between the two rotors closest to the ground

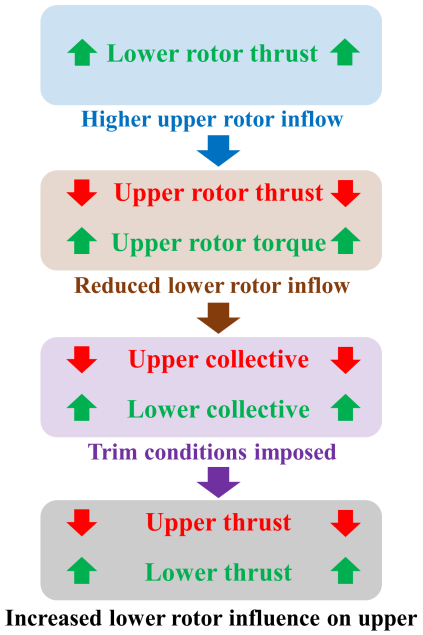

Figure 4.9: Schematic summary explaining the physics behind the observed thrust trend of CCR individual rotor in trimmed experimental conditions.

These observations confirm that the ground has a greater impact on the lower rotor, and the interactions between the two rotors are altered as the lower rotor's influence on the upper rotor is heightened due to their proximity to the ground. Thus, a decoupled measure of the lower rotor influence onto the upper rotor at both the rotor spacing is needed and was studied by comparing to a single rotor at the same effective height and trimmed to the same thrust as the upper rotor in the corresponding CCR configuration (Fig. 4.1b). These experiments were carried out only for the extreme rotor height cases of $z/R = 3.16$ & 0.82, and the results are discussed in the next section.

Effect of the lower rotor on the upper rotor during IGE

The results for the comparison of the torque requirement between the upper rotor in CCR ($d/R = 0.14$) and the equivalent thrust-matched single rotor is summarized in Fig. 4.10 along with the percentage differences in torque computed relative to the single rotor torque. At OGE condition ($z/R = 3.16$), the upper rotor in CCR configuration required 18.9% more torque than the equivalent single rotor to produce the same thrust due to the additional inflow induced by the lower rotor onto the upper rotor. When the rotor height was reduced to $z/R = 0.82$, the torque

requirement of both the upper and single rotor was reduced. In addition, the upper rotor in the CCR configuration still required more torque than the equivalent single rotor to produce the same thrust, which is again due to the influence of the lower rotor on the upper rotor. Still, the difference in magnitude was larger (39.9%).

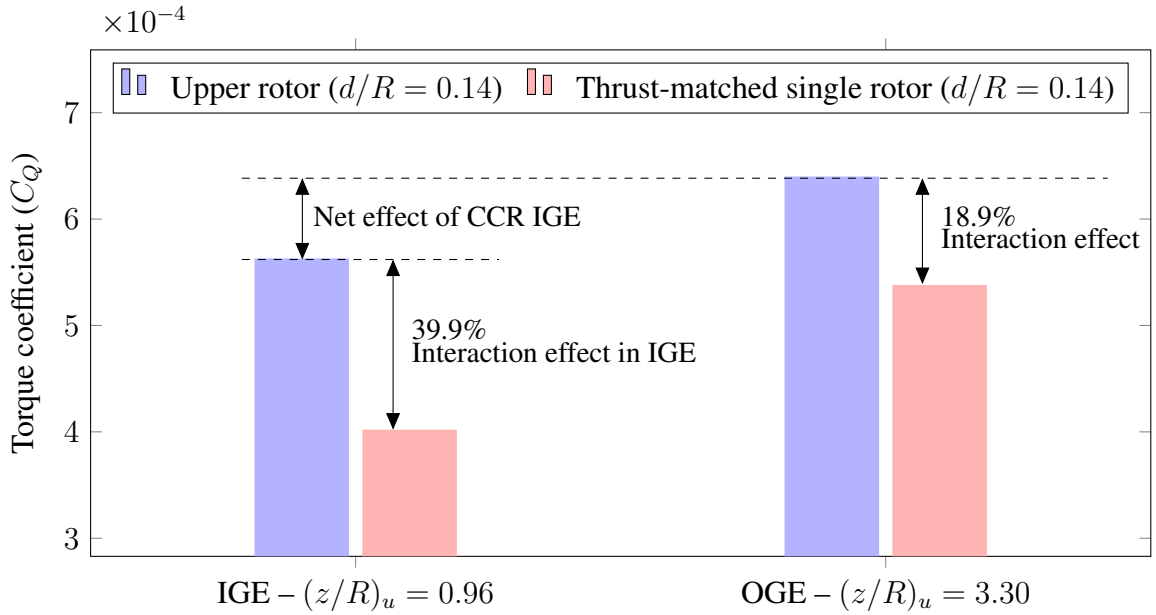

Figure 4.10: Comparison of torque coefficient of the upper and thrust-matched single rotor at the same effective height as the CCR upper rotor for rotor spacing of $d/R = 0.14$.

In other words, the reduction in upper rotor torque when the rotor height was reduced was significantly less than the single rotor, which illustrates that the influence of the lower rotor onto the upper rotor increases with a reduction in rotor height. The increased influence of the lower rotor is because the lower rotor thrust increases drastically with the reduction in rotor height, which induces higher inflow onto the upper rotor compared to the OGE case, thereby negating some beneficial effects of ground proximity. An increase in rotor spacing (from $d/R = 0.14$ to 0.34) resulted in a significantly lesser influence of the lower rotor onto the upper rotor in IGE compared to the smaller rotor spacing case of $d/R = 0.14$. The rotor spacing of $d/R = 0.34$ results are shown in Fig. 4.11. In this case, the performance decrease for the upper lower due to lower rotor interactions was 17.6% OGE and 25.9% IGE. These results are expected as the induced inflow from the lower rotor onto the upper rotor reduces with increasing rotor spacing as dictated by Biot-Savart law.

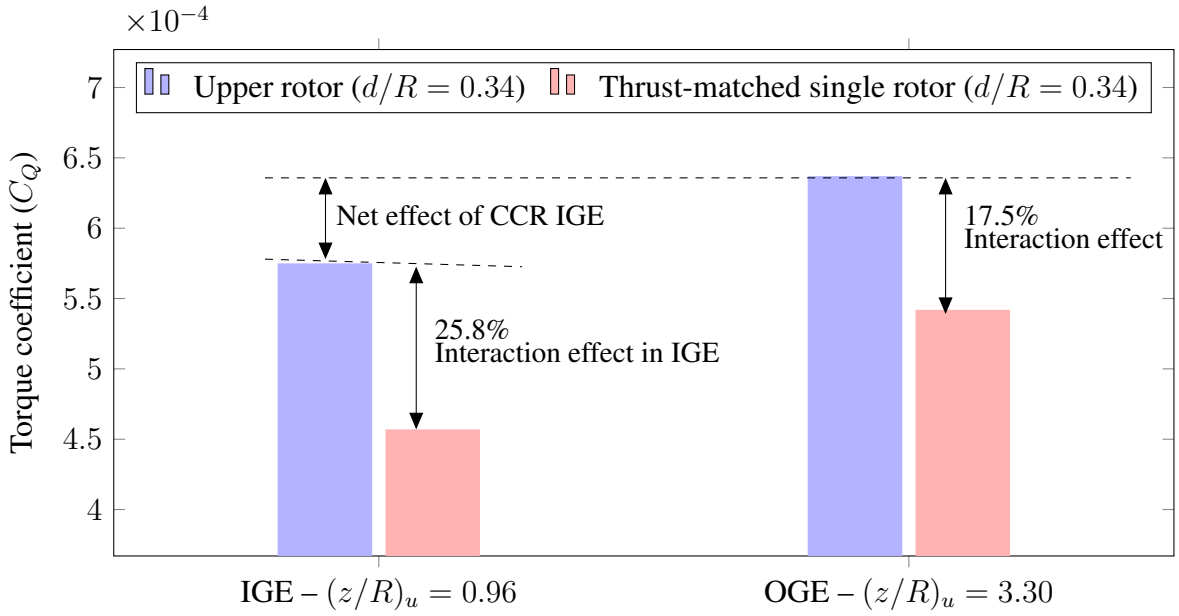

Figure 4.11: Comparison of torque coefficient of the upper and thrust-matched single rotor at the same effective height as the CCR upper rotor for rotor spacing of $d/R = 0.34$.

4.4.5 Summary of rotor-on-rotor interactions

The observations made from the untrimmed experiments showed that, in general, the net thrust of both the upper and lower rotor increased when the rotor height was reduced from $z/R = 3.16$ to 0.82 (Fig. 4.8). However, there are some intricacies in the performance variation as rotor height varies, where the individual rotor thrust shows varying trends. In particular, the upper rotor thrust at different rotor heights can either increase, stay nominally constant, or even decrease with decreasing rotor height. It is important to note that although the intricate variations in individual rotor thrust and torque under IGE are relatively small, they are not simply due to scattering in experimental data. Instead, it is argued that these are physical variations driven by the combination of rotor-to-rotor interactions and ground effect. This section discusses possible physical phenomena contributing to these observed behaviors for the individual rotor thrust and torque with the reduction of the rotor height for untrimmed conditions. The discussion is complimented by a schematic summary with cases corresponding to different ground conditions, as shown in Fig. 4.12.

'Case 1' in Fig. 4.12 corresponds to the OGE case where the rotor-to-rotor interaction effects have a degrading effect on the performance of the individual rotors in CCR as compared

to single rotors [6, 32]. On the other hand, 'Case 3' in Fig. 4.12 corresponds to the extreme case of IGE where the ground effects are the predominant influence on the performance of CCR and the individual rotors. As discussed previously, the ground has an augmenting effect, and a drastic increase in rotor performance is observed, for example, at rotor height of $(z/R)_u \leq 1.44$ for rotor spacing of $d/R = 0.14$ (Fig. 4.8). In between these two extremes, where either rotor-to-rotor interactional effects or ground effects dominate, there exists an aerodynamic regime where these two opposing effects are of a similar order of magnitude leading to intricate variations in individual rotor performance.

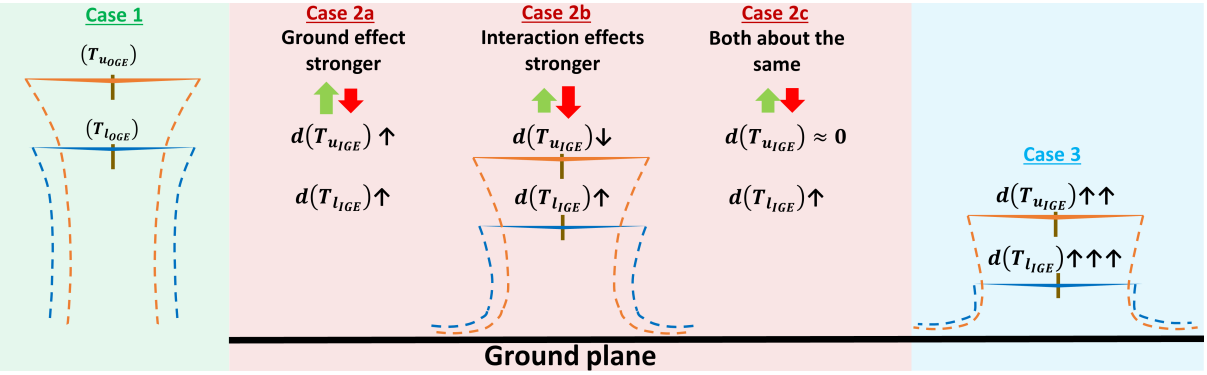

Figure 4.12: Schematic summary explaining the variation of the thrust of a CCR hovering in ground effect for untrimmed conditions.

This regime, called 'Case 2', is where the lower rotor exhibits a slow monotonic increase in thrust with decreasing ground height. The upper rotor, however, shows some interesting variations with its thrust increasing, remaining constant, or even decreasing. These changes in rotor thrust are represented by dT in Fig. 4.12. 'Case 2' is further divided into three subsets:

1. 'Case 2a' in Fig. 4.12 corresponds to an instance where the influence of ground is larger than the interactional effects for the upper rotor. Under these conditions, the upper rotor thrust is expected to increase ($(dT_u)_{IGE} \uparrow$) with the reduction in rotor height, where $(dT_u)_{IGE}$ in Fig. 4.12 denotes the change in upper rotor thrust with respect to reduction in rotor height. Example of this was observed in the experimental data as illustrated in Fig. 4.8 for upper rotor heights of $1.9 \leq (z/R)_u \leq 2.06$ and $2.1 \leq (z/R)_u \leq 2.26$ for rotor spacing of $d/R = 0.14$ & 0.34, respectively.

2. 'Case 2b' corresponds to an instance where the effects of ground on the upper rotor are smaller than that of the interactional effects. Under this scenario, the upper rotor thrust is

expected to reduce with a reduction in rotor height ($(dT_u)_{IGE} \downarrow$). Such a scenario is possible at rotor heights where the lower rotor experiences a larger influence of the ground, resulting in a drastic increase in its thrust compared to the upper rotor. This will induce additional inflow onto the upper rotor, which could result in increased interactional effects that exceed the effects of the ground. These effects can also result in the lower rotor thrust exceeding that of the upper rotor. Such effects were observed experimentally for the rotor spacing of $d/R = 0.34$ at rotor heights of $1.64 \leq (z/R)_u \leq 1.9$ (Fig. 4.8).

3. 'Case 2c' corresponds to an instance where the interactional and ground effects are equal to and negate each other. Under this scenario, the upper rotor thrust is expected to be invariant with the reduction in rotor height ($(dT_u)_{IGE} \approx 0$). Such scenario was observed experimentally for the rotor spacing of $d/R = 0.14$ at rotor heights of $1.44 \leq (z/R)_u \leq 1.9$ (Fig. 4.8).

It should also be noted that depending on the configuration of the CCR and the operating conditions, Cases '2a', '2b', and '2c' may not all be realized or realized in any specific order. There is limited evidence in the measurements that a similar interplay of interaction effects and ground effect is seen on the lower rotor as well, e.g., decreasing dT for $d/R = 0.34$ from $(z/R)_l = 1.76$ to $(z/R)_l = 1.56$ (Fig. 4.8). Finally, from the current experimental data, the specific factors contributing to the individual rotors behaving in such a manner at different rotor heights are still unknown and require additional studies. Simultaneous flowfield measurements would prove to be useful in understanding these behaviors as it is known that the ground proximity modifies the wake characteristics of the rotors, which affects their performance. Different factors, such as the variation in the number of blades, blade profile, and operating thrust conditions, among others, might yield different results, which also need to be explored to gain a more comprehensive understanding of the CCR behavior under the influence of ground.

4.5 Chapter summary

The current work focused on the performance measurements of a counter-rotating coaxial rotor (CCR) operating in the presence of a ground plane. The performance of both CCR as a

system and individual rotors was assessed by varying the rotor height above the ground from $z/R = 3.16$ (approximated as OGE) to $z/R = 0.82$. The effects of rotor spacing on the CCR and individual rotor performance were also studied at $d/R = 0.14$ & 0.34. Untrimmed experiments were conducted where the rotor height was varied at fixed rotor collectives corresponding to OGE trim of equal upper and lower rotor torque and the total CCR thrust coefficient of $C_T = 0.0081$. Trimmed experiments were also carried out with the same trim condition maintained for all rotor heights by adjusting the rotor collectives. To better understand the interplay between rotor-to-rotor interactions and ground effect, single-rotor experiments were carried out where the single rotor was placed at the same height and trimmed to the same thrust as the upper rotor in the CCR configuration. These experiments helped characterize the influence of the lower rotor onto the upper rotor in the presence of ground. The conclusions drawn from this study are summarized below:

1. Comparison of the performance ratio (IGE-to-OGE) of the CCR with the single rotor showed that the ground had a similar influence for both the single rotor and CCR. The difference in CCR performance in IGE between rotor spacing of $d/R = 0.14$ & 0.34 was also minimal.

2. The variation in thrust and torque of individual rotors in CCR exhibited varying trends based on rotor height and the relative magnitude of two competitive effects – the degrading influence of rotor-to-rotor interactions versus the augmenting influence of ground effects. These effects were more pronounced for the upper rotor when compared to that of the lower rotor.

3. The individual rotor data showed that the effects of ground were stronger for the lower rotor when compared to that for the upper rotor, as the lower rotor showed a relatively higher increase in its performance with the reduction of rotor height for both the untrimmed and trimmed conditions. The lower rotor also showed a larger increase in thrust further from the ground than the upper rotor, even after accounting for its relative proximity due to rotor separation.

4. Comparison with the single rotor at the same rotor height and same thrust showed that in the CCR configuration, the influence of the lower rotor on the upper rotor increased with ground proximity. The upper rotor required more power in close IGE than OGE to generate the same thrust as a single rotor due to the increased interference of the lower rotor operating in IGE. A similar observation was made for both the rotor separation distances measured.

Chapter 5

Characterization of the hydrodynamic towing tank facility

A hydrodynamic towing tank facility was developed to address Aim 2 of this dissertation, which aimed to quantify the influence of blade-on-blade interactions, specifically blade passage, on the unsteady loading of counter-rotating coaxial rotors. This facility enables the translation of two blades in opposite directions, effectively creating a single-blade passage event. The blades used in this study were custom-built from aluminum. The facility has load cells and flow field measurement capabilities to assess blade loads during blade passage. Blade loads can also be extracted from flow measurements using a control volume approach [70, 71]. As an initial step, the effectiveness of the facility to conduct scientific studies had to be established. The facility's validation involved studying blade performance characteristics under various motion profiles, including steady translation and surging conditions at varying angles of attack. Performance measurements were complemented with flow measurements to gain insights into the underlying physics of the observed phenomena. Furthermore, verifying the validity of the control volume approach for extracting loads in a translating wing configuration was crucial.

5.1 Objectives

This chapter aims to provide confidence in the capability of the hydrodynamic towing tank facility to perform scientific measurements through experiments involving well-established fluid flow problems. The specific objectives of this chapter are summarized below:

1. To characterize the load characteristics of the blades translating in single wing configuration.

2. To quantify the wake characteristics of the single wing at relevant Reynolds number conditions.

3. To validate the control volume approach to extract blade loads from the flow measurements for a translating wing system.

5.2 Approach

Validation tests were conducted using a NACA0012 airfoil section wing for steady translation and surging wing cases. Flow measurements were used to extract loads via the control volume approach, and these results were compared with load cell measurements and existing literature. The blades were rapidly accelerated to a constant translation speed for the steady translation case, and loads were measured. The impact of initial acceleration on the steady-state characteristics was investigated. The study covered a range of operating Reynolds numbers from $Re = 15000 - 35000$. At these low Reynolds numbers, the formation of laminar separation bubbles and periodic vortex shedding is anticipated, even at low angles of attack [75, 76]. Force and flow field measurements were used to understand and characterize the effects of these low Reynolds number phenomena on blade load characteristics.

The loads were also extracted using a control volume (CV) approach as discussed in Section 2.6. These loads were compared with load cell measurements to validate the CV approach. Furthermore, a blade at a 6° angle of attack, featuring a NACA0012 airfoil section, underwent translation with a sinusoidally varying surging velocity profile. The resulting loads were measured using load cells, extracted using the CV approach, and compared with Greenberg's model [77]. These surging wing experiments provided confidence in the translation system's capability to execute custom motion profiles and affirmed its efficacy in conducting experiments involving unsteady flow conditions.

For the control volume analysis, a two-dimensional control volume centered around the airfoil and having a size of $(6c \times 3c)$ was generated. Mohebbian [71] has shown that the size of the CV does not significantly influence the results. This was verified for the current study by changing the CV from $(4c \times 2c)$ to $(6c \times 3c)$. The current size of the CV was chosen to ensure

the CV is farther away from the edge of the FOV and from the blades such that the viscous effects are not significant. As the fluid is quiescent and the wing is translating, the control volume was also translated with a steady translation velocity, as shown in Fig. 5.1. This results in a moving control volume problem, where the relative velocity between the CV and the blade would equal the perturbations in the steady translation velocities. For example, the relative velocity between the blade and the control volume would be zero for a steady translation case and would equal the perturbations to the base velocity of v_o for surging cases. Equation 5.1 for the moving control volume problem is modified to the form given below:

$$\underbrace{F_B}_{\text{Load cell}} = \underbrace{-\rho\frac{\partial}{\partial t}\iint_{\sum}(\mathbf{x})((\mathbf{u}+\mathbf{U}_\infty)\cdot\mathbf{n})dS}_{\text{Temporal acceleration}} - \underbrace{\iint_{\sum}(\mathbf{u}+\mathbf{U}_\infty)((\mathbf{u}+\mathbf{U}_\infty)\cdot\mathbf{n})\,dS}_{\text{Convective acceleration}} + \frac{1}{n-1}\iint_{\sum}\mathbf{x}\times(\mathbf{n}\times(-\rho\mathbf{a}-\mu\nabla\times\omega))ds + \iint_{\sum}(\bar{\bar{\tau}}\cdot\mathbf{n})ds \tag{5.1}$$

where U_∞ is the steady translation velocity of the control volume.

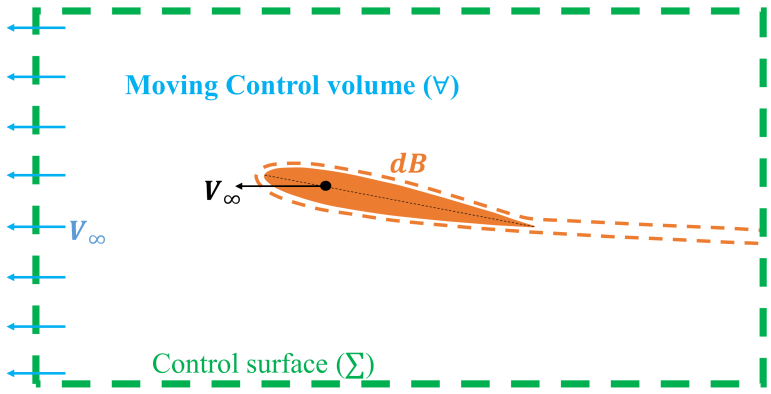

Figure 5.1: Representation of a lifting body immersed in a fluid and bounded by a control volume ($\forall$).

5.3 Operating conditions

The experiments were carried out at low angles of attack (AOA) to establish the benchmark of the current system at regimes before stalling. The blade with the NACA0012 airfoil profile section had a chord length and a span of $0.036\ m$ and $0.254\ m$, respectively. The experiments were carried out at steady translation and surging conditions, and the summary of the operating conditions is provided in Table 5.1. The velocity profiles for the steady translation and surging

Table 5.1: Summary of the operating conditions for the validation of the hydrodynamic towing tank facility

Test conditions	Pitch angle (α)	Reynolds number (Re)	Acceleration distance (s_a)
Steady translation (Fig. 5.2(a)) (NACA0012)	$0°, 2°, 4°, 6°, 8°, 10°, 12°, 14°$	15000, 25000, 35000	$1c, 2c, 4c, 8c$
Surging (Fig. 5.2(b)) (NACA0012)	$6°$	15000	-

cases are shown in Fig. 5.2. Initially, the blade was set to an AOA of $6°$ and was translated with varying initial acceleration distances of $1c, 2c, 4c$, and $8c$ at three Reynolds number conditions of $Re = 15000, 25000$ and 35000. Using a constant acceleration rate, the linear actuator was accelerated to a uniform speed. The effects of this initial acceleration distance on the blade load steady-state characteristics were studied. Then, the steady-state characteristics of each blade were studied by placing them on both translation stages. This arrangement was used to quantify the potential differences between the blades and the translation stages. Here, the AOA of the blades was changed as $0° - 14°$ at an increment of $2°$ and the lift, drag, and moment experienced by the blades were studied. Particle image velocimetry (PIV) was also used to quantify the blade wake characteristics for specific AOA and Reynolds number cases.

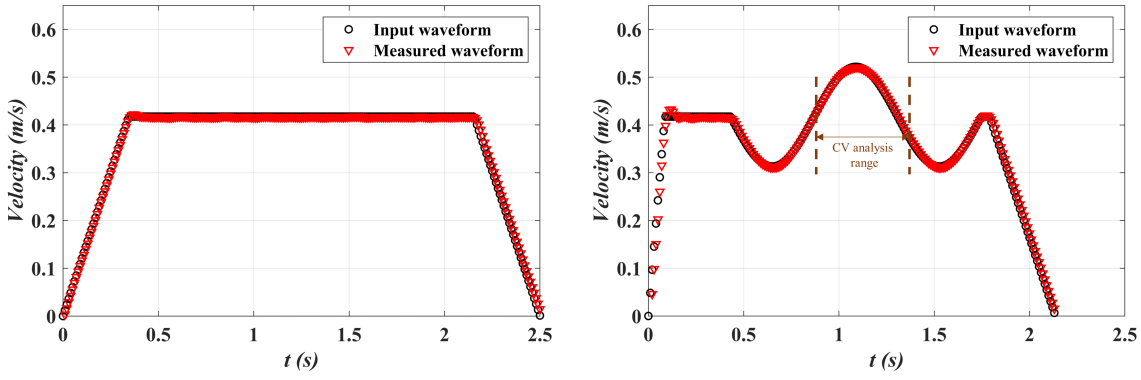

(a) Accelerating (b) Surging

Figure 5.2: Comparison between the input and measured velocity profiles.

After establishing the steady-state characteristics of the blade, the blade load characteristics under surging motion were studied. Here, the blade AOA was set at $6°$ and subjected to the surging motion as shown in Fig. 5.2a. The velocity profile for the surging motion was defined

as:

$$v(t) = v_o \left[1 + \lambda sin\left(\frac{2kv_o}{c}t\right)\right] \tag{5.2}$$

where $v_o = 0.5\ m/s$ is the base velocity, $k = 0.309$ is the reduced velocity, $\lambda = 0.25$ is the amplitude to the sinusoidal expressed as the ratio to the average velocity, and c is the chord length. These values were taken from one of the test cases of a study by Kirk [78].

5.4 Results and Discussion

Initially, the steady-state characteristics of the NACA0012 airfoil profile blade were explored. Here, the effects of initial acceleration on the steady state have been quantified. The steady-state loads were then extracted at three Reynolds number conditions and compared with the literature. The flow field of the blades at these Reynolds numbers was also measured using PIV.

5.4.1 Effects of initial acceleration on the steady-state characteristics

The temporal characteristics of the blade lift coefficient (C_l) at 6° angle of attack were measured. Using a constant acceleration rate, the linear actuator was accelerated to a uniform speed. First, the initial acceleration distance was between $1c - 8c$, and the results are summarized in Fig. 5.3. The data were also compared with Wagner's function, represented by the black dashed line in Fig. 5.3. Wagner's function accounts for the delay in circulation development on an impulsively started flat plate [79]. Jones' [80] approximation provides an expression for lift production by an impulsively started wing with finite aspect ratio (AR) as

$$C_l = 2\pi\alpha\phi\frac{AR}{AR + 2} \tag{5.3}$$

where,

$$\phi = 1.0 - 0.165e^{-0.0455s} - 0.335e^{-0.3s} \tag{5.4}$$

with s being the normalized blade translation distance.

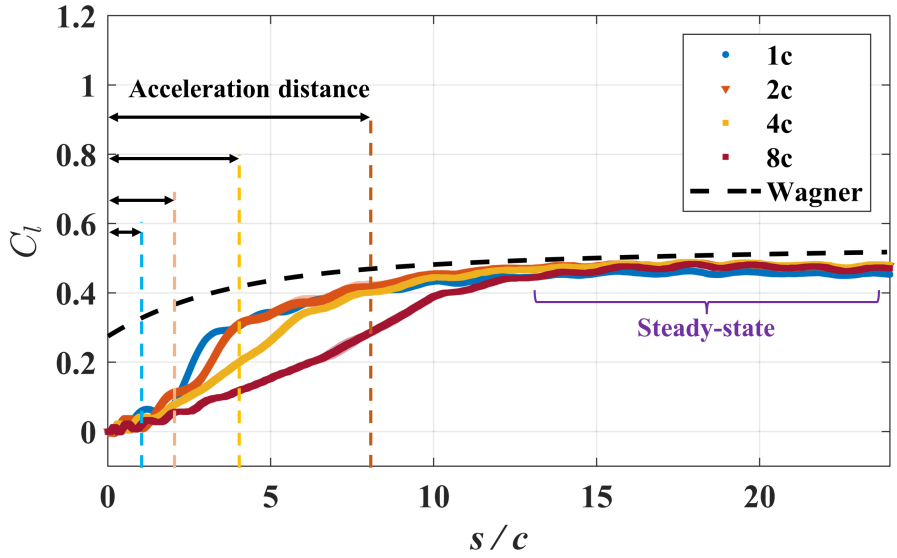

Figure 5.3: Effects of initial acceleration distance on the temporal variation in the coefficient of lift (C_l) for a single wing section at $\alpha = 6°$ and $Re = 25000$.

Figure 5.3 shows the temporal load characteristics for different initial accelerations at the Reynolds number of $Re - 25000$. For the acceleration distance of $8c$, the steady state is only reached after the translation distance of $12c$, which limits the steady translation distance to $11c$. Reducing the initial acceleration distance to $4c, 2c$, and $1c$ resulted in the steady state being reached by $10c$. However, the initial acceleration of $1c$ resulted in a high initial impulse, which can ultimately damage the system. Thus, initial accelerations of $2c$ and $4c$ proved a safe choice for maximizing the steady-state translation length and ensuring safe operations. For current studies, the initial acceleration distance of $2c$ was chosen for characterizing the blade's steady-state behavior.

The effects of the Reynolds number on the temporal load characteristics were also explored by setting the initial acceleration distance to $2c$. The results are shown in Fig. 5.4. Here, the steady state in the lift was achieved within $10c$ for all Reynolds number cases. The steady-state lift characteristics followed a close trend with Wagner's function for all Reynolds numbers. In addition, the experiments were repeated over three runs and were averaged. The shaded region in Fig. 5.4 shows the standard deviation across these three repetitions. The variability between runs was observed to be small, confirming the repeatability of the current measurements.

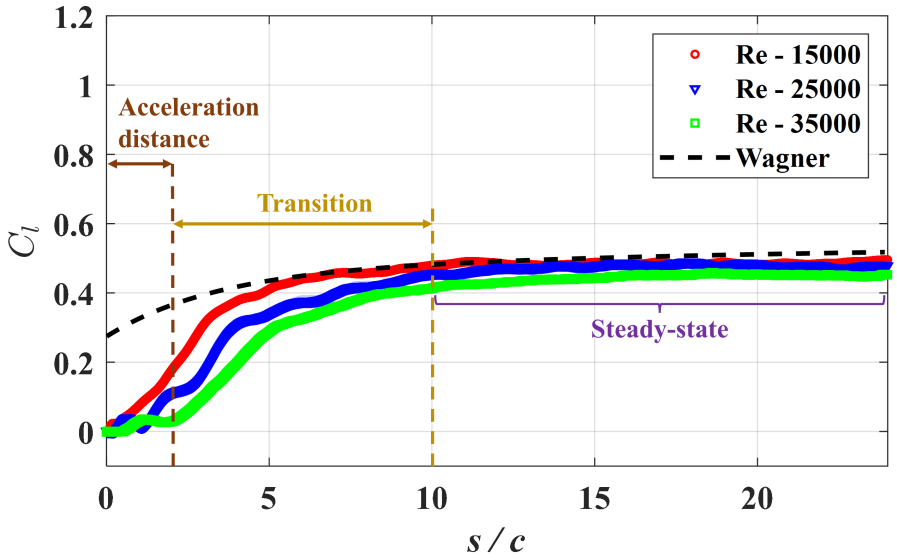

Figure 5.4: Effects of Reynolds number on the temporal variation in the coefficient of lift (C_l) for a single wing section at 6° angle of attack..

5.4.2 Steady-state characteristics of the loads

After studying the blade temporal load behavior, its steady-state characteristics were explored. The loads were averaged between the translation distance of $(10 - 22)c$ to extract the steady-state characteristics. These measurements were again averaged over three repetitions to confirm the repeatability of the measurements. These measurements were carried out for two blades (Blades 1 and 2), each placed in both the translation stages ($T1$ & $T2$). These measurements were carried out to ensure that both the blades and the translation stages were identical in nature.

The variation in the lift coefficient with angles of attack for Blade 1 and Blade 2, placed in positions T1 and T2, is summarized in Fig. 5.5. Additionally, for comparison, results from a study conducted by Ohtake [11] on a NACA0012 airfoil profile wing at a Reynolds number of $Re = 40000$ are also presented. Notably, the coefficient of lift exhibited non-linear behavior even at low pitch angles when compared to the potential flow lift. This observation aligns with findings in the literature [11]. As anticipated, the lift coefficient began to deviate from the potential lift at higher angles of attack, and both wings were observed to stall at an angle of attack of 12°. These consistent results for both the wings and translation stages affirm the identical nature of the blades and translation stages.

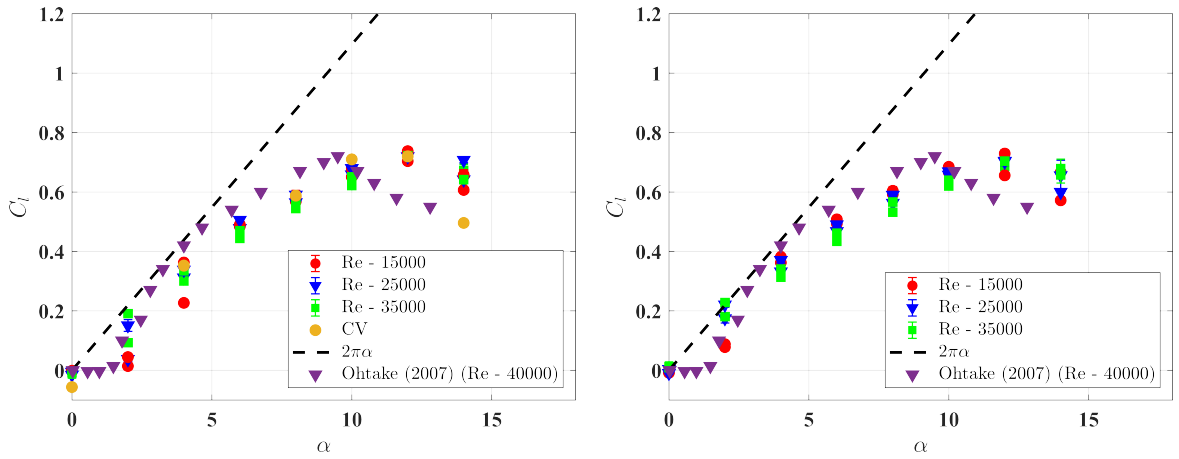

(a) Blade 1 (b) Blade 2

Figure 5.5: Coefficient of lift variation with angle of attack for (a) Blade 1 placed in both translation stages ($T1$ & $T2$), and (b) Blade 2 placed in both translation stages ($T1$ & $T2$). The results are compared with Ohtake [11], where experiments were done at $Re - 40000$ for the NACA0012 airfoil section wing.

The observed non-linearities in the lift characteristics can likely be attributed to the formation of laminar separation bubbles and vortex shedding, primarily due to low Reynolds number effects. Such flow phenomena have been reported in prior literature [75, 76]. A laminar separation bubble occurs when the laminar boundary layer separates from the surface due to an adverse pressure gradient. This separated shear layer eventually transitions into turbulent flow, and the turbulent mixing leads to the reattachment of the flow. The presence of a separation bubble between the separated and reattached flow regions alters the pressure distribution on the suction side, resulting in a reduction in lift. The adverse impact of a laminar separation bubble is more prominent at low Reynolds numbers because the shear layer takes a longer time to transition to turbulent flow, thereby resulting in a larger laminar separation bubble. The occurrence of these separations towards the trailing edge also causes the periodic vortex shedding in the wake.

The onset of these flow phenomena is highly dependent on the Reynolds number, and consequently, variations in the Reynolds number can significantly affect the aerodynamic force behavior. As demonstrated in Fig. 5.5, the influence of Reynolds number conditions on steady-state lift characteristics is clearly noticeable. For instance, the lift coefficient at a pitch angle of $\alpha = 2^{\circ}$ was nearly zero at the Reynolds number case of $Re = 15000$, which suggests the

presence of a laminar separation bubble at these low Reynolds number conditions. In contrast, at higher Reynolds number cases, the lift coefficients were notably higher.

At higher angles of attack, where the lift coefficient appeared similar across the three Reynolds number cases, the effects of the Reynolds number were less apparent. While it's important to note that flowfield measurements were not conducted, the force measurements strongly indicate the presence of these flow phenomena under the current experimental conditions. It's crucial to acknowledge that the potential effects of these low Reynolds number phenomena are encompassed in the results of the blade crossover study presented in the following chapter.

The loadcell measurements have also been compared with the results from the control volume analysis for AOA cases of $\alpha = 0°, 4°, 8°, 10°, 12°$ and $14°$. For brevity, only the results for the Reynolds number case of $Re = 35000$ are shown in Fig. 5.5a. These measurements were only taken for Blade 1 in translation stage T1. The lift coefficient (C_l) from the control volume approach was obtained by averaging the load measurements between the translation distance of $(11 - 16)c$. This range of translation distance was the limitation posed by the current field of view.

The results from the control volume approach followed a close trend with the loadcell measurements at all pitch angles. As the wings were translating at a steady velocity, the expectation is that the contribution of the unsteady term from the CV analysis should be close to zero. To confirm this, the decomposition of the measured loads from the CV approach is shown in Fig 5.6. The decomposition was performed for the pitch angles of $\alpha = 0°, 4°, 8°, 10°, 12°$ and $14°$. For pitch angles below $\alpha = 12°$, the contribution of the unsteady term is close to zero, which is expected.

The pressure term also has negligible contributions as the flow is attached. The contribution from the pressure term is only expected under separated flow conditions with strong shear layers and vortical structures. As a result, the contribution to the total lift is purely from the convective term. For the pitch angle case of $\alpha = 12°$, the unsteady term showed a negative influence on the total lift. These effects are amplified for the post-stall case of $\alpha = 14°$, where both the convective and unsteady terms significantly influence the total lift. This is expected

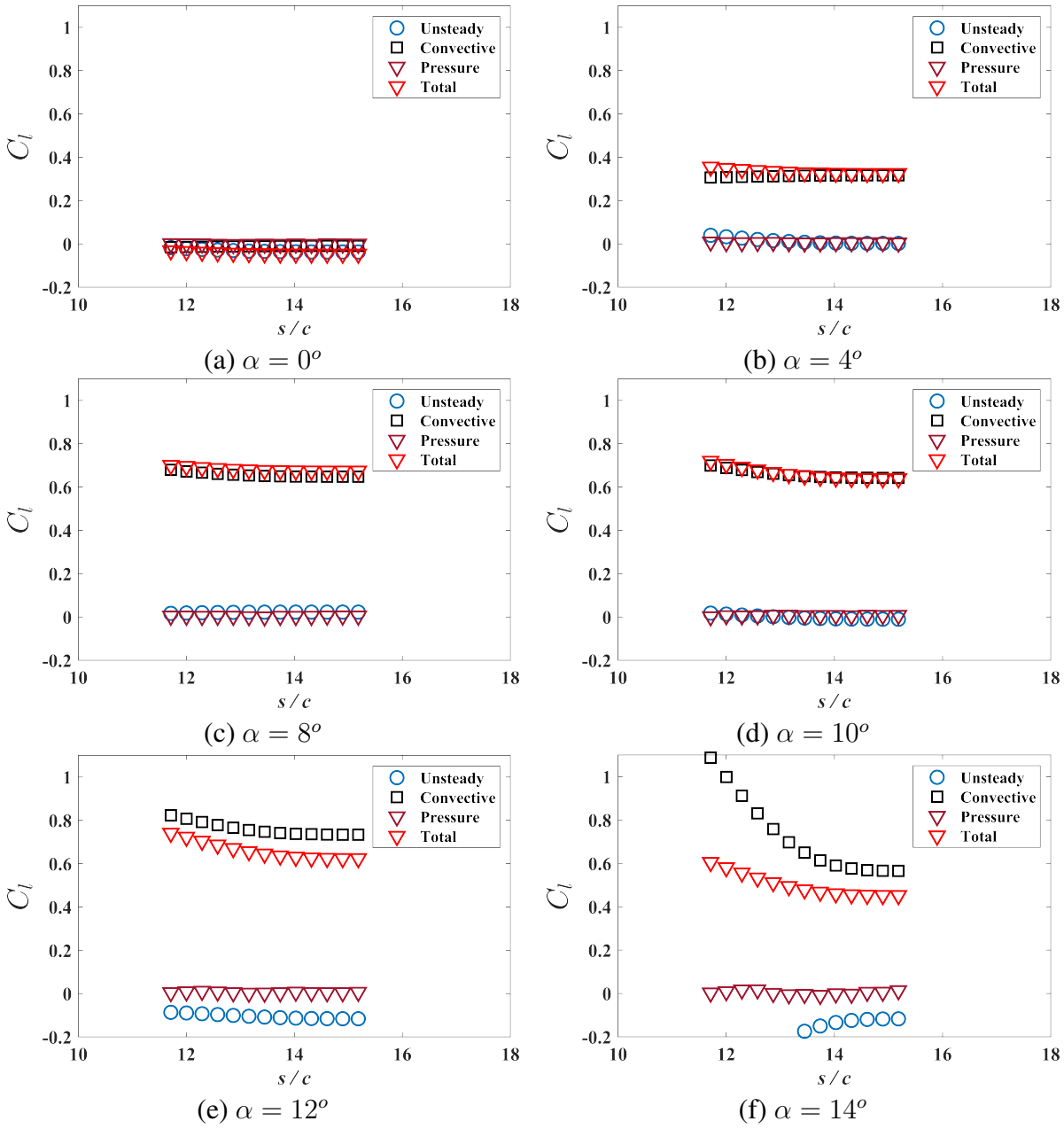

Figure 5.6: Force decomposition using control volume analysis for a steady translation case at the Reynolds number of $Re = 35000$.

as the flow conditions are no longer steady in the separated conditions. These observations provide confidence in the CV approach to studying steady translating wing cases.

The coefficient of drag and moment for Blade 1 is shown in Fig. 5.7. The low Reynolds number case results of $Re = 15000$ were unreliable due to the low signal-to-noise ratio for these small magnitudes of forces. Thus, the results for $Re = 15000$ have not been shown. Similarly, the control volume analysis results are also not shown, as the drag and moment were

not resolved by the control volume approach either. The limited spatial resolution of the PIV measurements could be the limiting factor for the calculations for the drag and moment for a streamlined body at low angles of attack.

The results for the Reynolds number cases of $Re = 25000$ and 35000 follow a close trend with the literature [11]. As expected, the moment coefficient about the quarter chord location was close to zero for a thin symmetric airfoil. The stall characteristics were also apparent as both the drag and moment were observed to show a sudden rise after the AOA of 12^o. An interesting observation was that the drag coefficient decreased when the AOA was increased from 0^o to 4^o. This could result from vortex shedding in the wake due to low Reynolds number flow separation at an AOA of 0^o. With an increase in the AOA to 4^o, the separation point could move towards the trailing edge, reducing the wake deficit and, thus, the drag. The blade wake characteristics have been analyzed using PIV to confirm the differences in wake characteristics at low angles of attack.

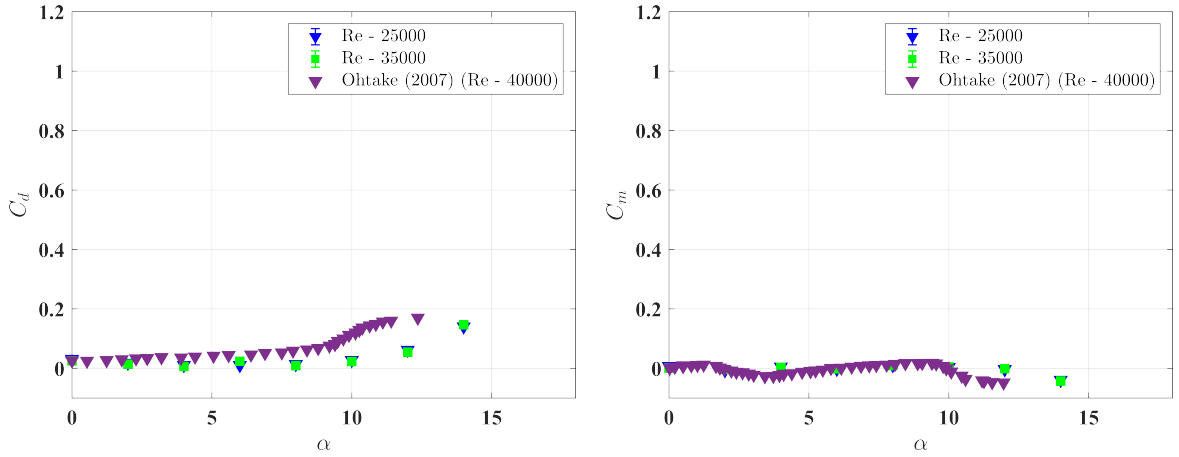

(a) Drag (b) Moment

Figure 5.7: Variation in coefficient of (a) drag and (b) moment with the angle of attack for Blade 1 placed in the translation stage 1 (T1). The results are compared with Ohtake [11], where experiments were done at $Re - 40000$ for the NACA0012 airfoil section wing.

The wake behavior for angles of attack of $\alpha = 0^o,\ 4^o,\ 8^o$ and $\alpha = 10^o$ at the Reynolds number of $Re = 35000$ are shown in Fig. 5.8. All cases show a periodic vortex shedding in the wake, which suggests the presence of laminar separation. However, the vorticity of these vortices reduced when the AOA was increased from $\alpha = 0^o$ and $\alpha = 4^o$. This observation

was consistent over the entire blade translation span for all Reynolds numbers currently tested. These wake measurements show that the minimum drag observed at the AOA of $\alpha = 4^o$ from the force measurements results from a reduction in wake deficit, possibly due to the movement of the separation point towards the trailing edge. As a reference, the wake characteristics of AOA cases of $\alpha = 8^o$ and $\alpha = 10^o$ have also been shown. The data shows an increase in the strength of the shed vortices in the wake with an increase in AOA. This observation is consistent with the force measurements, which also showed an increasing trend in drag beyond AOA of 6^o.

These measurements show that the initial acceleration distance of $2c$ is a safe choice for the current system, and it doesn't affect the steady-state load characteristics of the blades. The results also show that the two translation stages are identical, with minimal manufacturing defects in the used blades. The system's efficacy in accurately measuring the blade loads and flowfield was also established. Next, the surging wing case was explored to establish the facility's capability to conduct unsteady measurements.

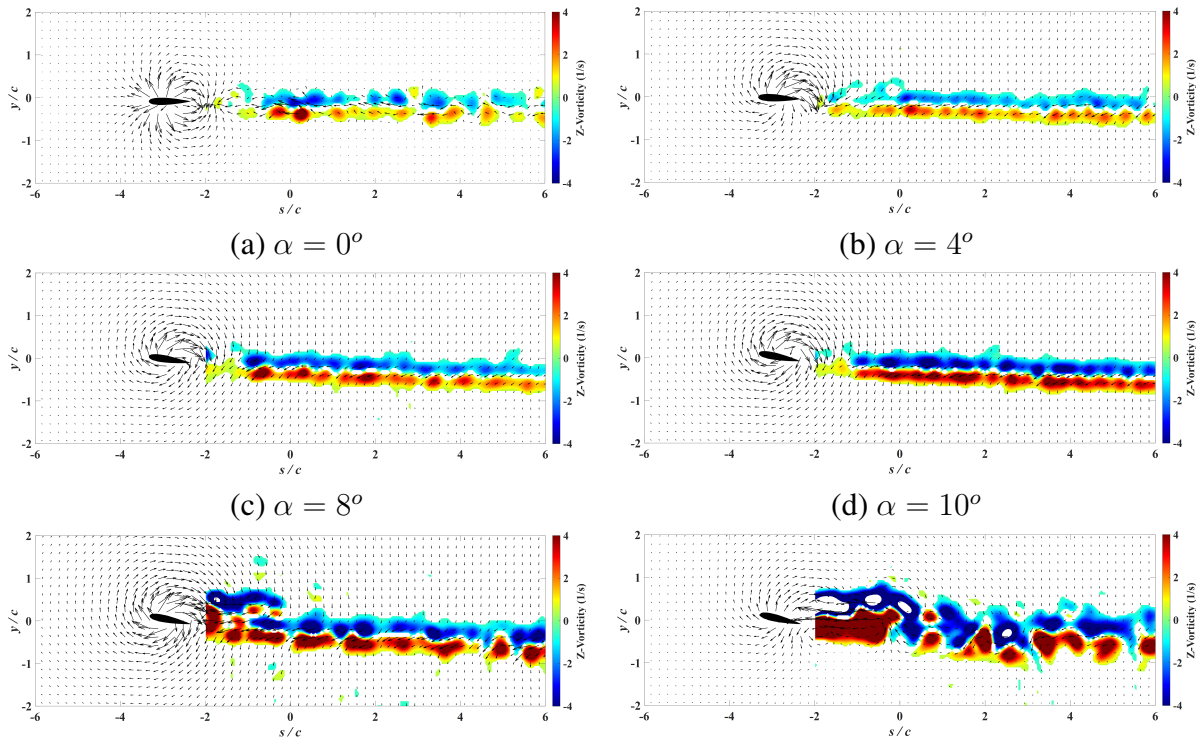

(a) $\alpha = 0^o$ (b) $\alpha = 4^o$

(c) $\alpha = 8^o$ (d) $\alpha = 10^o$

(e) $\alpha = 12^o$ (f) $\alpha = 14^o$

Figure 5.8: Comparison of the Wake characteristics of the blade at Reynolds number of $Re = 35000$. The data were down-sampled for demonstration purposes.

5.4.3 Surging wing case

The NACA0012 airfoil profile wing set at 6° of AOA was translated in a surging velocity profile as shown in Fig. 5.2b. The loads were measured from the loadcell and extracted using the moving CV approach. The results are summarized in Fig. 5.9. As a reference, the dashed black line also shows the result from Greenberg's model [77]. Greenberg's model provides closed-form expressions for the lift and moment of an aerofoil in attached flow undergoing sinusoidal pitch, surge, and plunge. Greenberg's model for the total force per unit span F for a surging wing can be simplified to an expression given below:

$$F = -\frac{c}{2}\pi\rho\alpha\left(\frac{c}{2}\dot{v} + 2vv_o + (2vv_o\lambda)\Re\{C(k)e^{i\omega_v t}\}\right) \tag{5.5}$$

where ω_v is the circular frequency of the velocity cycle and is given as $\omega_v = 2kv_o/c$. The chord length (c), density (ρ), and pitch angle (α) were taken as $0.036\ m$, $1000\ kg/m^3$ and $0.10472\ rad$, respectively. Theodorsen's function, $C(k)$, depends only on reduced frequency. For the reduced frequency of $k = 0.309$, Theodorsen's function is given as $C(k) = \{0.6606 - 0.1781i\}$. These values of pitch reduced frequency and ω were a test case in the gust interaction study by Smith [81]. These specific values were chosen to ensure that a complete cycle of the surging profile can be achieved in the current setup with a limited translation distance.

The C_l was normalized by its steady-state component for the AOA of $\alpha = 6^o$. For Greenberg's model, the steady-state C_l was the value when $\lambda = 0$, i.e., $F = c\pi {v_o}^2\rho\alpha$. The temporal range for analyzing the loadcell measurements is shown in the inset in Fig. 5.9. The results from the CV analysis did not cover the entire measurement range of the loadcell measurements because of the limitation of the total field of view covering the blade motion. The inset in Fig. 5.10 shows the total temporal range for the moving CV analysis. From Fig. 5.9, it is observed that the loadcell measurements and the loads from the moving CV approach follow a close trend with Greenberg's model, with the CV approach showing slightly more deviation. This could possibly be due to the accumulation of errors in the flowfield measurements.

As a next step, the total force obtained from the moving CV approach was further decomposed into the unsteady, convective, and pressure contributions. The results are shown in

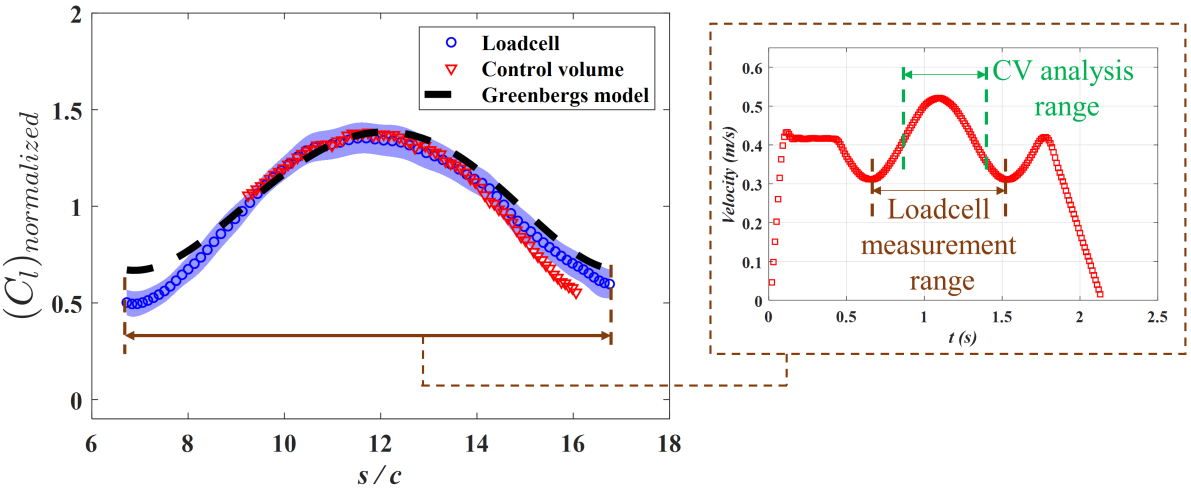

Figure 5.9: Comparison between the coefficient of lift (C_l) obtained from loadcell measurements, moving control volume approach, and Greenberg's model; the C_l normalized by the steady-state value when the $\lambda = 0$. The insets represent the surging wing velocity profile and the temporal range for plotting the loadcell data.

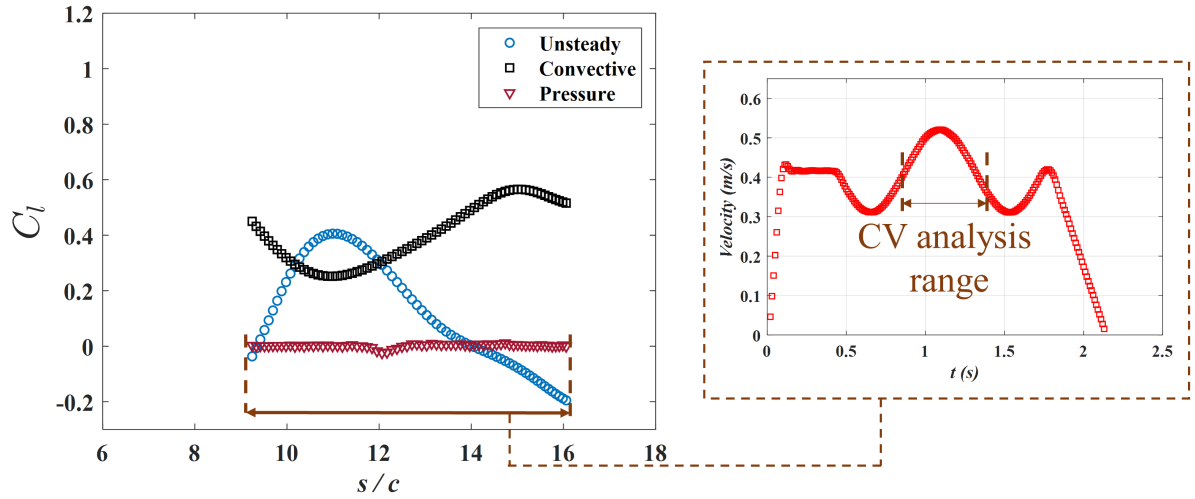

Figure 5.10: Decomposition of the unsteady and convective effects using the control volume approach during surging motion. The insets represent the surging wing velocity profile and show the temporal range over which the control volume analysis was carried out.

Fig. 5.10. The reduced frequency for the current case was chosen to be $k = 0.309$, which falls under a highly unsteady regime ($k > 0.2$) as stated by Lieshman [73]. Here, the total lift is expected to be highly dominated by the unsteady effects.

The results show that the unsteady effects are dominant, with the contribution of the unsteady effects exceeding that of the convective effects during the initial acceleration phase.

Additionally, the contributions from the pressure term were near zero. Mohebbian [71] observed that the contributions from the pressure term were only important when strong leading and trailing edge vortices from a flapping flat plate reached the control surfaces. Here, as the wake is not dominated by strong vortices at these low angles of attack, the contribution from the pressure term is expected to be minimal. Overall, the results from the moving CV approach are encouraging and suggest that this approach can be applied to study the translating wing cases.

5.5 Chapter summary

A translating wing facility was developed to facilitate canonical studies of blade crossover. Two test cases were considered to validate the facility: the steady translation wing and the surging wing. The blade loads were measured, and the results were compared with the literature. Similarly, the flowfield was measured for the steady translation and surging wing cases to explore the efficacy of using a moving control volume approach to extract blade loads from the flowfield measurements of a translating blade. The steady translation experiments were carried out for the NACA0012 profile section blade at Reynolds number ranging from $Re = 15000$ to 35000. The angles of attack were varied from $\alpha = 0^\circ - 14^\circ$ at an increment of 2° for the load measurements. Similarly, the flowfield was measured for the specific angles of attack cases of $\alpha = 0^\circ, 4^\circ, 8^\circ, 10^\circ, 12^\circ$ and 14°. Similarly, the surging wing experiments were carried out for the base Reynolds number of $Re_\circ = 15000$ for an angle of attack of $\alpha = 6^\circ$. Some of the conclusions that can be drawn from this study are summarized below:

1. The lift variation with angle of attack for NACA0012 airfoil blades showed non-linearities due to flow separations at low Reynolds number cases.

2. Minimum drag was observed at an angle of attack of around $\alpha = 4^\circ$ for the blade with symmetric airfoil section of NACA0012. This is attributed to higher pressure drag at 0° due to periodic vortex shedding in the wake.

3. The loads extracted from the moving control volume approach for the steady translating wing matched well with the loadcell measurements, with only the convective term contributing to the total lift.

4. For the surging wing case, the load measurements from the loadcells and the moving control volume approach followed a close trend with Greenberg's model. The unsteady term significantly contributed to the total lift during the accelerating and decelerating phases.

5. The results demonstrate that the proposed moving control volume approach can be applied to studying the unsteady flows for a translating wing.

Chapter 6

Blade load characteristics during blade crossover

The second aim of this dissertation is to understand the intricate physics of blade crossover events. The term ”blade crossover event” denotes a specific phase in operating a counter-rotating coaxial rotor (CCR) system where the blades of the upper and lower rotors intersect during flight. This occurrence introduces transient excursions in the loads experienced by the rotor blades. Although some studies have acknowledged the presence of these temporary fluctuations in blade loads during the crossover event, the precise nature of these changes and the multitude of factors that affect them remain largely unquantified.

Various parameters, including blade profile, spacing, and blade-bound circulation, among others, can substantially impact the characteristics of blade loads. To study the influence of these parameters, a facility capable of conducting a parametric study under different conditions is required. Subsequently, it becomes essential to determine the relevant non-dimensional parameters that influence the problem, followed by experiments that must be conducted to determine their influence. Simultaneous flowfield measurements must also be carried out to understand the underlying physics. Quantifying the influence of these non-dimensional parameters is crucial for understanding the physics of the problem and ultimately developing accurate models to predict load characteristics during blade crossover.

As blade cross-over events are transient in nature, the unsteady effects can also dominate the transient load excursion characteristics. The magnitude of the influence of these unsteady effects also needs to be determined to assist future modeling approaches. This holistic approach is instrumental in improving our understanding of the intricate dynamics of blade crossover events in CCR.

6.1 Objectives

As the problem has not been studied yet, the aim is to establish the relevant non-dimensional parameters that pertain to the problem and identify all the areas that would need detailed investigation to fully comprehend the physics of the problem. The chapter also provides essential considerations that need to be made for existing/future models to improve the accuracy of their predictions. The objectives of the study presented in this chapter can be summarized as below:

1. Determine the relevant non-dimensional parameters that govern the load characteristics during blade crossover.

2. Conduct experiments to understand the influence and importance of each of these non-dimensional parameters.

3. Quantify the unsteady effects on load excursions during blade crossover.

6.2 Approach

The effects of blade crossover were studied in the hydrodynamic towing tank facility (Section 2.3). Two infinite blades were translated in equal and opposite directions to simulate a singular blade crossover event. The load and flowfield characteristics were measured during the blade crossover event. Blade loads were measured using strain gauge load cells and the flow field was measured using particle image velocimetry (PIV).

The relevant non-dimensional parameters influencing the blade crossover problem were determined using Buckingham's π theorem. A total of eight variables with three fundamental dimensions were chosen. The variables considered are: blade chord (c), blade span (b), blade spacing (d), translation speed (U_∞), steady-state lift (L), blade thickness (t_h), fluid density (ρ), speed of sound (c_s) and fluid viscosity (μ). The analysis using Buckingham's π theorem shows that the excursion in the lift coefficient (δC_l) is a function of five known non-dimensional parameters: Reynolds number (Re), blade thickness to chord ratio (β_h), steady-state lift coefficient (C_l), normalized blade spacing (d_N), aspect ratio (AR), and match number (M_∞). The

relationship is defined as:

$$\delta C_l = f(Re, t_h, C_l, d_N, AR, M_\infty) \tag{6.1}$$

where,

$$\delta C_l = \frac{\delta L}{0.5\rho U_\infty^2 cb} \tag{6.2}$$

$$Re = \frac{U_\infty c}{\nu} \tag{6.3}$$

$$\beta_h = \frac{t_h}{c} \tag{6.4}$$

$$C_l = \frac{L}{0.5\rho U_\infty^2 cb} \tag{6.5}$$

$$d_N = \frac{d}{c} \tag{6.6}$$

$$AR = \frac{b}{c} \tag{6.7}$$

$$M_\infty = \frac{U_\infty}{c_s} \tag{6.8}$$

Here, the experiments are done in infinite wing conditions, and thus, the three-dimensional effects can be neglected. As such, the effects of the aspect ratio (AR) do not need to be considered for the current conditions. The effects of Mach number (M_∞) can also be neglected as the experiments were done in incompressible flow conditions. As such, Eq. 6.1 becomes:

$$\delta C_l = f(Re, \beta_h, C_l, d_N) \tag{6.9}$$

Experiments were then carried out to determine the effects of these non-dimensional parameters. Here, it is important to mention that the effects of airfoil shape could also play a significant role in the load characteristics during the blade passage, and thus, the effects of blade curvature were also explored under the same section that discusses the effects of blade thickness effects.

The potential lower-order modeling approach for the blade crossover event was also explored by providing an analogy between the gust interaction problem and the blade crossover problem. The gust induced by a single translating blade at a specific spacing was extracted from the flowfield measurements for this analysis. These extracted velocity profiles were fitted to the Kussner function to model the blade lift response. Kussner function is a modification of Theodorsen's function for pitching, plunging, and surging wings, the analysis of which is based on unsteady linear aerodynamic theory. The Kussner function provides an analytical lift response of a thin airfoil translated through a sharp-edged gust. These functions are used in convolution schemes to model blade interactions with arbitrary gust profiles. The lift buildup to an arbitrary gust is given as:

$$L = \pi \rho U_\infty c \left[w_g(0)\psi(S) + \int_0 S \frac{dw_g(\sigma)}{d\sigma} \psi(S-\sigma) d\sigma \right] \tag{6.10}$$

where $w_g = v/U_\infty$, $S = 2tU_\infty/c$ is the non-dimensional time, i.e., the length traveled in semi-chords from the leading edge, and $\psi(S)$ is the Kussner function approximated as:

$$\psi(S) \approx 1 - 0.5e^{-0.13S} - 0.5e^{-S} \tag{6.11}$$

Further details on the derivation involving the Kussner function are provided in Lieshman [73].

The integral form of the Kussner function in Eq. 6.10 is complicated, as it involves a convolution operation and can be computationally expensive when evaluated over extended periods of time. As such, Zaide [82] identified a parametric model for gust response. Zaide [82] proposed an autoregressive-moving-average (ARMA) model to relate the aerodynamic lift coefficient to the gust input at the current and previous time steps and to the previous time-step values of the lift coefficient. These models were shown to perfectly capture the gust response

under incompressible and inviscid regimes. The ARMA model assumes the following model structure:

$$C_l(n) = -a_1 C_l(n-1) - a_2 C_l(n-2) - ... - a_{n_a} C_l(n-n_a) + \\ b_\circ w_g(n) + b_1 w_g(n-1) + ... + b_{n_b} w_g(n-n_b) \tag{6.12}$$

where $C_l(n)$ is the time-dependent lift coefficient, and $w_g(n)$ is the gust input value at the leading edge at discrete time n. n_a and n_b are model orders determined by the user. a_{n_a} and b_{n_a} are model parameters to be estimated. Zaide [82] states that the Kussner function in Eq. 6.11 can be written as an ARMA model of the order $n_a = 2$, $n_b = 1$ and its parameters a_1, a_2 and $b_\circ, b_1$ can be calculated exactly for various values of discrete time steps, ΔS, as follows:

$$a_1 = -\frac{1.13\Delta S + 2}{0.13\Delta S^2 + 1.13\Delta S + 1} \tag{6.13}$$

$$a_2 = \frac{1}{0.13\Delta S^2 + 1.13\Delta S + 1} \tag{6.14}$$

$$b_\circ = \frac{0.13\Delta S^2 + 0.565\Delta S}{0.13\Delta S^2 + 1.13\Delta S + 1} \tag{6.15}$$

$$b_1 = \frac{0.565\Delta S}{0.13\Delta S^2 + 1.13\Delta S + 1} \tag{6.16}$$

The lift response from this model and that from the experiments were compared to studying the analogy between the blade crossover and gust interaction problem. The unsteady effects were then quantified by applying the moving control volume approach, as discussed in the previous section (Section 5.2). The control volume approach assisted in decomposing the unsteady and convective effects, providing insights into the physics of the problem and better informing the modeling efforts.

6.3 Operating conditions

The experiments were carried out for flat plates and blades with NACA0012 and NACA0018 airfoil profile sections. The two blades under investigation were called Blade 1 and Blade 2. Blade 1 occupied the lower position, while Blade 2 was placed above it. Both blades had a span of 0.254 meters. The chord length was varied for the NACA0012 profile blade sections as $c = 0.036m$ and $c = 0.072m$. For the blade with a smaller chord length, experiments were carried out at translation speeds ranging between $U_\infty = (0.41 - 0.97)m/s$, at pitch angles ranging between $\alpha = 0^\circ - 14^\circ$ and blade spacing ranging between $d/c = 1.4 - 3$. Flowfield measurements were also carried out for some of the specific cases. For blades with larger chord lengths of $c = 0.072m$, experiments were carried out at a fixed blade spacing of $d/c = 1.4$ and a pitch angle of $\alpha = 0^\circ$. The translation speed was varied as $U_\infty = (0.209 - 0.69)m/s$.

For flat plates and blades with NACA0018 airfoil profile, the experiments were carried out at a pitch angle of $\alpha = 0^\circ$, blade spacing of $d/c = 1.4$, and translation speeds ranging as $U_\infty = (0.41 - 0.97)m/s$. For flat plates and NACA0012 airfoil blades, additional experiments were carried out at a pitch angle of $\alpha = 4^\circ$ to develop an analogy to gust interaction studies. In these experiments, the bottom blade (Blade 1) was set at $\alpha = 4^\circ$, and the top blade at $\alpha = 0^\circ$. A detailed summary of these operating conditions is provided in Table 6.1.

6.4 Results and Discussion

The blade crossover event results in transient excursions in the blade loads. The characteristics of the excursions in the loads experienced by each blade during the blade crossover are demonstrated through a test case of blade crossover at a pitch angle of $\alpha = 0^\circ$ for the Reynolds number case of $Re = 25000$. The lift coefficient excursion (δC_l) is plotted against the non-dimensional translation distance (s/c) in Fig. 6.1. The lift coefficient excursion (δC_l) is calculated by subtracting the lift coefficient of a single blade from that undergoing a crossover event. The translation distance of $s/c = 0$ represents a distance when the quarter chord of the two blades is aligned (shown in the inset of Fig. 6.1) and is represented by a gray dashed line in this chapter.

Table 6.1: Experimental matrix for blade crossover study

Blade section	Configuration	Blade spacing (d/c)	α (Blade 1)	α (Blade 2)	Re
NACA0012 (Chord - 0.036m)	Isolated single	-	$\mathbf{0}^\circ, 2^\circ, \mathbf{4}^\circ, 6^\circ, \mathbf{8}^\circ, \mathbf{10}^\circ \mathbf{12}^\circ, \mathbf{14}^\circ$	$0^\circ, 2^\circ, 4^\circ, 6^\circ, 8^\circ, 10^\circ 12^\circ, 14^\circ$	15000, 25000, 35000
	Blade crossover	1.4	$\mathbf{0}^\circ$ 2° $\mathbf{4}^\circ$ 6° $\mathbf{8}^\circ$ $\mathbf{10}^\circ$ $\mathbf{12}^\circ$ $\mathbf{14}^\circ$ 4°	$\mathbf{0}^\circ$ 2° $\mathbf{4}^\circ$ 6° $\mathbf{8}^\circ$ $\mathbf{10}^\circ$ $\mathbf{12}^\circ$ $\mathbf{14}^\circ$ 0°	
		2, 3	0° 8°	0° 8°	
Flat plate (Chord - 0.036m)	Isolated single	-	$\mathbf{0}^\circ, \mathbf{4}^\circ$	0°	
	Blade crossover	1.4	$\mathbf{0}^\circ$ 4°	$\mathbf{0}^\circ$ 0°	
NACA0018 (Chord - 0.036m)	Isolated single	1.4	0°	0°	
	Blade crossover	1.4	$\mathbf{0}^\circ$	$\mathbf{0}^\circ$	
NACA0012 (Chord - 0.072m)	Isolated single	-	0°	0°	15000, 20000, 25000, 30000, 35000, 50000
	Blade crossover	1.4	0°	0°	

When the blades were far apart, the difference between the single blade and those undergoing crossover was zero. As the quarter-chord location of the blades was approximately $1c$ away, the effects of the blade crossover event became evident. The blades began to experience an outward force relative to each other, which peaked slightly before the quarter-chord positions aligned, indicated as $s/c = 0$. Beyond this point, the load excursions decreased rapidly, changed direction, and reached a peak value similar to what was observed before the crossover. As the blades moved farther apart, the loads gradually returned to a value close to zero. The system's response influenced the characteristics of loads post-crossover. An impulse test determined that the current system exhibited an underdamped response with a frequency of approximately $10Hz$. A similar response frequency was observed in the post-crossover behavior of the blades.

Figure 6.2 provides an overview of the flowfield changes during the blade crossover event of a counter-rotating coaxial rotor system. When the rotor blades are initially far apart (Fig. 6.2a), the flowfield surrounding the blades exhibits symmetry, resulting in zero net lift. As

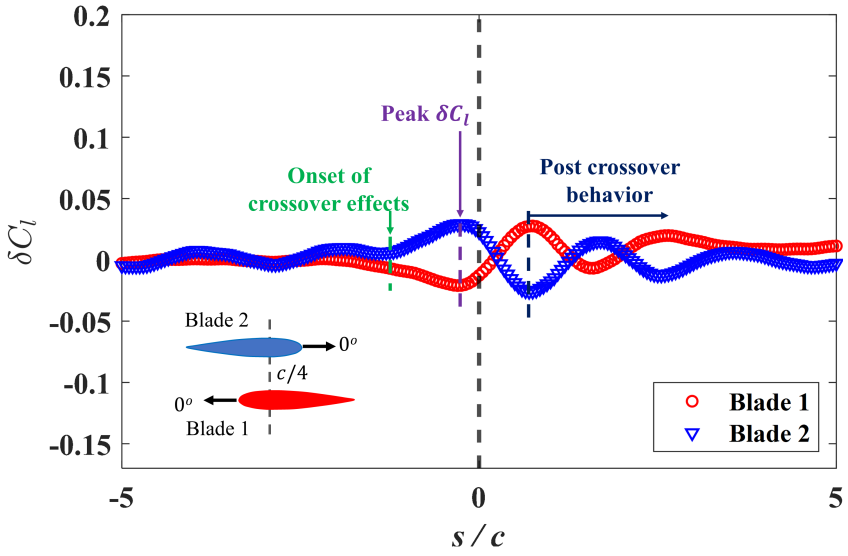

Figure 6.1: Normalized coefficient of lift during blade crossover at $\alpha = 0°$ and Reynolds number case of $Re = 25000$. The data were down-sampled for demonstration purposes.

the blades translated closer to each other (Fig. 6.2b), Blade 1 experiences a downwash caused by Blade 2, while Blade 2 experiences an upwash due to Blade 1, primarily influenced by the thickness of the blades. During this time, the interactions of the flowfield between the two blades resulted in a small region between the blades where the flow was quiescent. This region is termed a stagnation point, contributing to the increased pressure towards the leading edge of the two blades.

The combination of these effects creates an outward force between the blades as they approach each other. This finding aligns with the results reported in studies examining crossovers between two trains [61, 83]. Simulations of train crossovers revealed the formation of a high-pressure region as the trains approached each other, primarily near the trains' noses. Although pressure measurements were not conducted in the present study, the presence of a stagnation point suggests that pressure between the blades might have increased in this area. This supports the observed outward force experienced by the two blades.

As the blades undergo crossover, the stagnation point persists and stays in the same location(Fig. 6.2b, c, and d). Although the formation of a stagnation point results in a local increase in static pressure, it also results in other flow phenomena that contribute to the inward force experienced by each blade after $s/c = 0$. First, the thickness-induced upwash and downwash

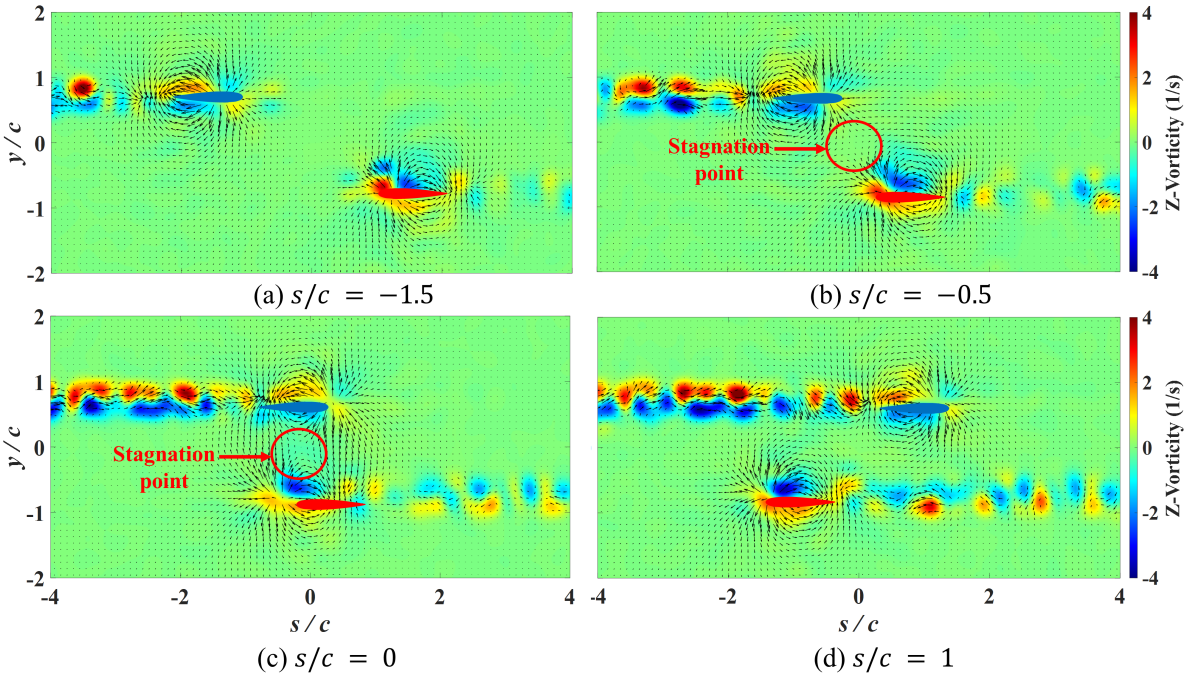

Figure 6.2: Flowfield evolution between the blades during blade crossover event for $\alpha = 0°$ and $Re = 25000$.

from Blade 1 and Blade 2, respectively, flow around the stagnation point. This leads to additional upwash toward the upper blade's trailing edge and downwash on the lower blade. Second, as the blades align with each other, the space between them decreases, causing an increase in velocity on the suction side of Blade 1 and the pressure side of Blade 2. These effects result in higher dynamic pressure on the suction and pressure sides of Blades 1 and 2, generating an inward force.

These observations also align with the train crossover literature. These studies [61, 83] have shown that as the trains that cross each other align with each other, the pressure between the trains drops significantly due to flow acceleration. Similar phenomena could be present in current conditions, which would result in the blades to experience inward force as they align against each other. After the blades move apart (Fig. 6.2d), the flowfield reverts to a symmetric state and any shed vortices in the wake of the blades have minimal impact on the loads or flowfield characteristics following the crossover event.

To further explore the phenomena discussed above, the velocity profiles at a location of $0.5c$ above and below the chord line of the two blades were extracted at four instances: (1) when the blades were far apart ($s/c = -4$), (2) approaching each other ($s/c = -0.5$), (3) quarter

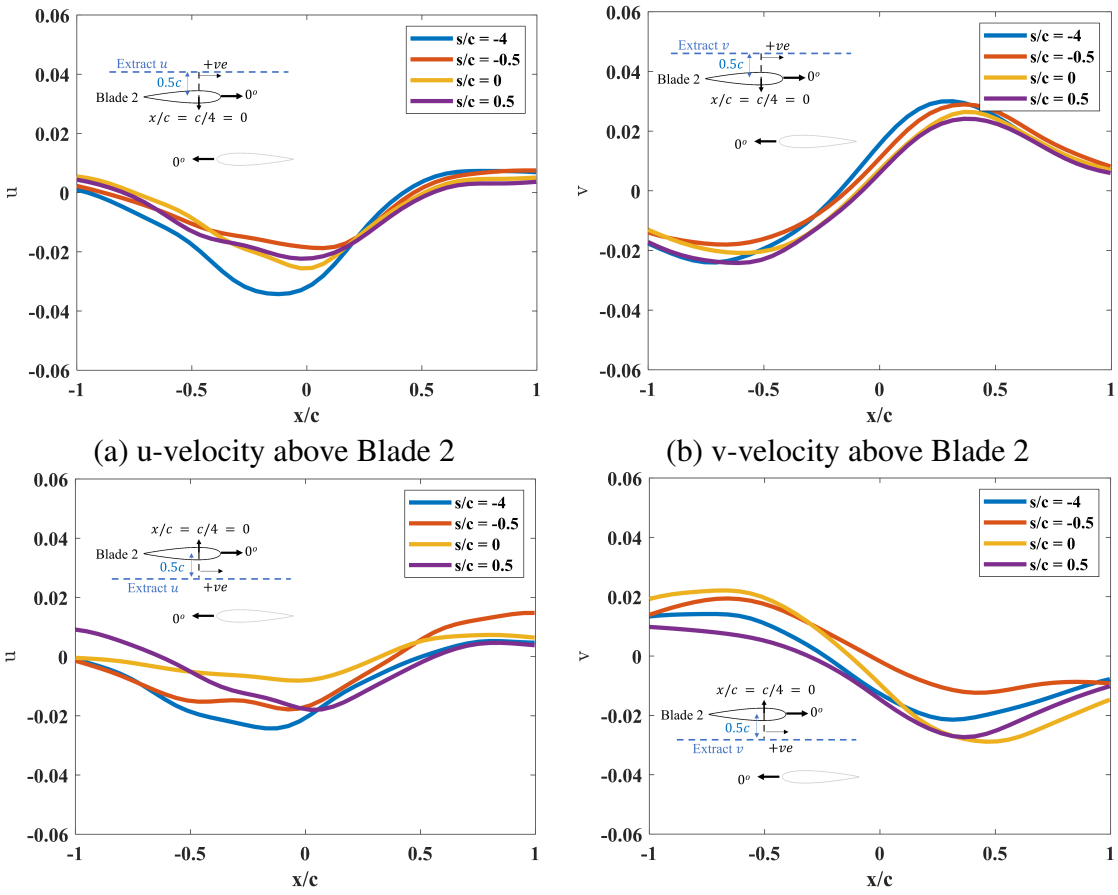

(a) u-velocity above Blade 2

(b) v-velocity above Blade 2

(c) u-velocity below Blade 2

(d) v-velocity below of Blade 2

Figure 6.3: Extracted velocity profiles above and below Blade 2 before, during, and after the blade crossover at the Reynolds number case of $Re = 25000$.

chord aligned against each other ($s/c = 0$) and (4) traveling away from each other ($s/c = 0.5$). The distance of $0.5c$ above and below the blades was chosen to ensure that velocity vectors were extracted in regions where the effects of reflections from the blade were minimal on the PIV cross-correlation algorithm. Although the velocity profile extracted at these locations does not provide a complete understanding of the velocity profile close to the airfoil surface, these velocity profiles could provide some explanation for the observed force measurements. The results from top blade (Blade 2) are shown in Fig. 6.3 and for the bother blade (Blade 1) are shown in Fig. 6.4. The x-axis represents the normalized horizontal distance by referencing the blade quarter-chord location.

For locations above the top blade (Blade 2) (Fig. 6.3a and b) and below the bottom blade (Blade 1) (Fig. 6.4c and d), the differences in the x and y components of the velocities

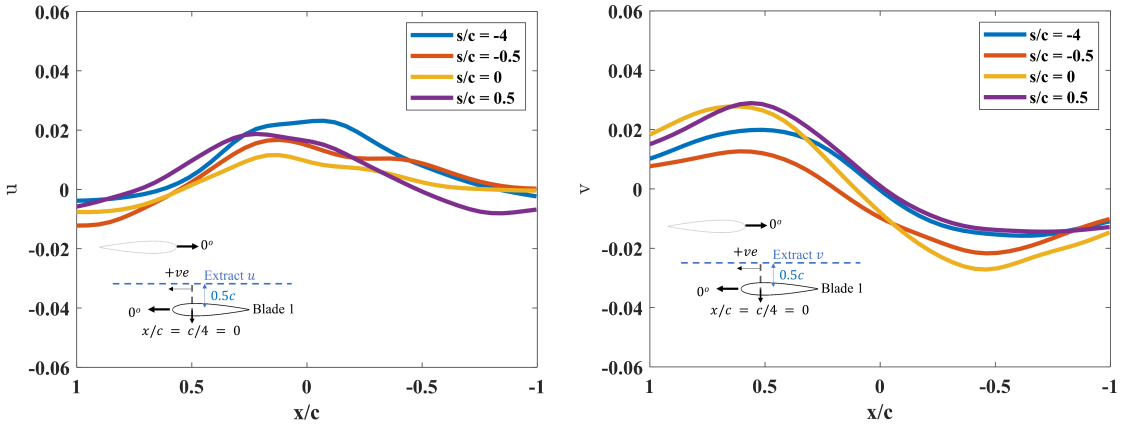

(a) u-velocity above Blade 1

(b) v-velocity above Blade 1

(c) u-velocity below Blade 1

(d) v-velocity below Blade 1

Figure 6.4: Extracted velocity profiles above and below Blade 1 before, during, and after the blade crossover at the Reynolds number case of $Re = 25000$.

were largely invariant to the blade crossover event. However, the velocity profiles below the top blade and above the bottom blade showed significant variation with respect to the crossover location. This observation suggests that the observed excursions in blade loads are largely due to variations in flowfield on the pressure and suction sides of the top and bottom blades, respectively.

The observed variations in the velocities between the two blades in different crossover stages corroborated with the observed load characteristics. As the blades approach each other ($s/c = -0.5$), reduction in the magnitude of the x and y-components of velocities were observed (Fig.6.3b and c, and Fig. 6.4a and b). As discussed earlier, this results from the combination of upwash and downwash effects of the two blades on each other and the stagnation flow region between the two blades (stagnation point). These effects result in an increase in static pressure on the pressure and suction sides of the top and bottom blades, respectively, and result in the observed outward forces. As the quarter-chord location of the blades aligned, a significant increase in velocity magnitude was observed for both the top (Fig. 6.3d) and bottom blades (Fig. 6.4b). This increase in velocity on the pressure and suction sides of the top and bottom blades indicates increased dynamic pressures at these locations. As a result, the blades experience an inward force as they align with each other.

Different operating and geometric variables could influence the magnitude of the observed upwash and downwash effects. As such, the relevant non-dimensional parameters were determined using Buckingham's π theorem to facilitate a systemic study of the effects of different variables. These non-dimensional parameters are presented in Section 6.2. The effects of these non-dimensional parameters on the loads during the blade passage are discussed in the next section.

6.4.1 Reynolds number effects

The Reynolds number (Re) is defined based on the blade chord length. The Reynolds number can be varied by changing the blade chord length or the translation velocity. To assess the potential effects of changing characteristic lengths and translation velocities, the reduced time (s_r)

was quantified. The reduced time is defined by [73] as:

$$s_r = \frac{2}{c}\int_0^t udt \tag{6.17}$$

The reduced time represents the relative distance traveled by the airfoil through the flow in terms of semi-chords for a time interval of t. Here, the time interval (t) for the blade crossover event is defined as the time that the airfoils travel from a configuration where their leading edges are aligned to a configuration where their trailing edges are aligned. The airfoils travel one chord length in this interval; thus, the time interval is $t = c/u$. Substituting this in Eq. 6.17 results in a constant reduced time of $s_r = 2$.

The calculation shows that the value of the reduced time is always constant, regardless of the translation velocity and the characteristic length. As such, the translation velocity, the characteristic length, and ultimately, the Reynolds number do not seem to influence the current problem. To explore this hypothesis, the Reynolds number was changed by changing the translation velocity and the blade chord length by keeping all the other parameters constant. The thickness to chord ratio was set to 12%, the initial bound circulation was set to zero with the pitch angle set to $0°$, and the non-dimensional blade spacing was set to $d/c = 1.4$. The parametric space for this study is summarized in Table 6.1. The chord length has been varied as $c = 0.036, 0.072\ m$, and the translation velocities for these blades have been varied between $u = (0.2 - 0.97)\ m/s$. The resulting Reynolds number of these combinations ranged from $Re = (15000 - 50000)$.

The lift variation at these Reynolds number cases was averaged, and the mean and standard deviation are shown in Fig. 6.5. The maximum excursion in the lift coefficient (δC_l) and its location ($s_{\delta Cl_{max}}$) is also shown in the insets of Fig. 6.5. Variations in the coefficient of lift behavior between the different Reynolds number cases were minimal, as shown by the standard deviation. Variation in the maximum coefficient of lift excursions and their locations was also minimal, as shown in Fig. 6.6. These results suggest that the effects of the Reynolds number on the lift behavior are not significant for the range tested in the current studies.

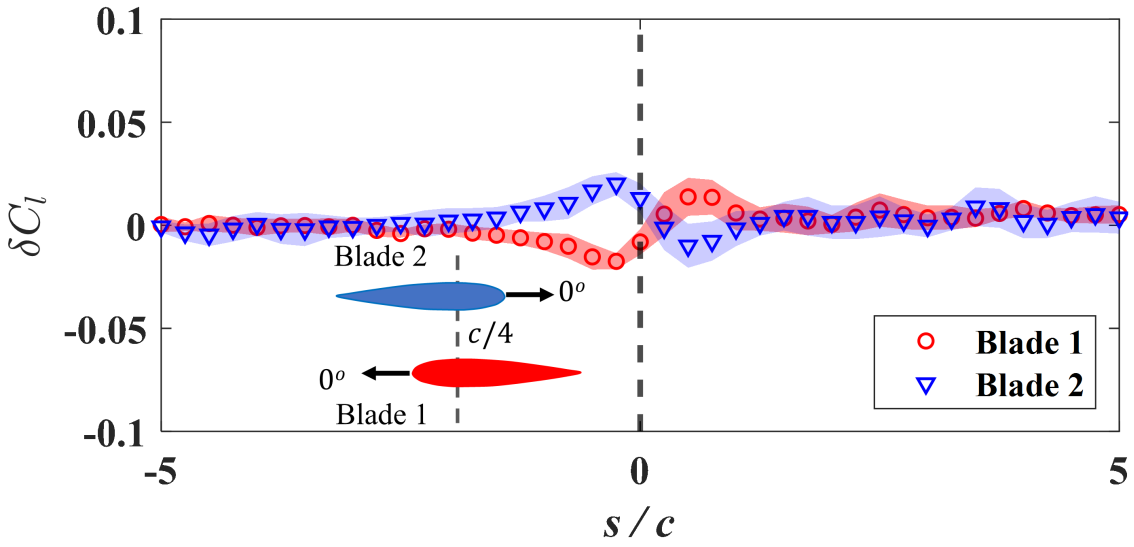

Figure 6.5: Normalized coefficient of lift across different Reynolds number cases. The shaded region represents the standard deviation. The data were down-sampled for demonstration purposes.

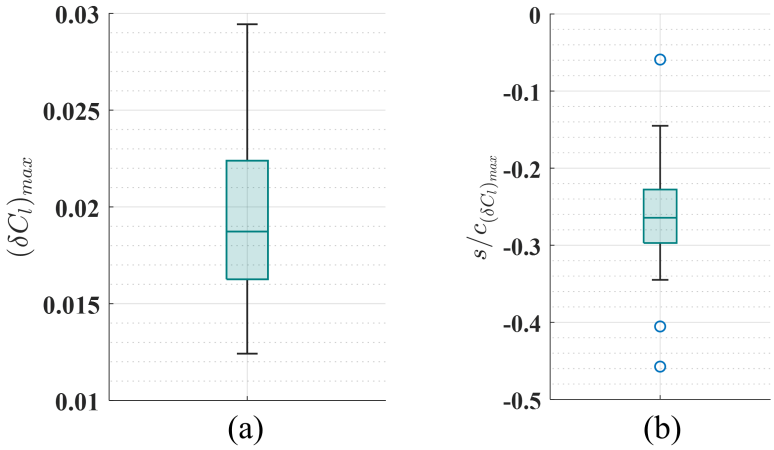

Figure 6.6: The box plots represent the variation in the peak excursion in the lift coefficient ($(\delta C_l)_{max}$) and the location of the peak excursion in the lift coefficient ($(s/c)_{(\delta C_l)_{max}}$).

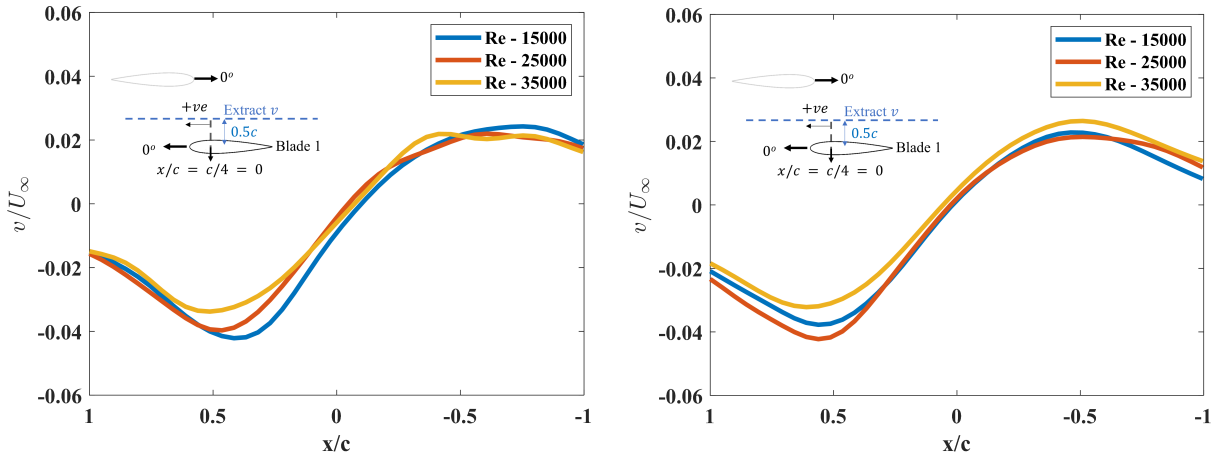

(a) At $s/c = -4$ (b) At $s/c = 0$

Figure 6.7: Extracted velocity profiles above Blade 1 before and during the blade crossover at three Reynolds number cases of $Re = 15000, 25000$, and 35000.

The y-component of velocity was extracted at the location of $0.5c$ above the bottom blade (Blade 1) chord line for the three Reynolds numbers of $Re = 15000, 25000$, and 35000. The location above the bottom blade was chosen as the velocity profile below Blade 1 was observed to be invariant to the blade crossover event. The velocity profiles for the upper blade were not presented here for the sake of brevity. The results are summarized in Fig 6.7, with Fig 6.7a illustrating velocity profiles at $s/c = -4$ and Fig 6.7b at $s/c = 0$. When normalized by their respective translation velocities (U_∞), it was evident that there was minimal variation in the velocity profiles with respect to the Reynolds number. This finding aligns with the load measurements, reinforcing the idea that the load variations during the blade crossover event are largely independent of Reynolds number effects.

In the current Reynolds number range, it is expected that phenomena like the formation of laminar separation bubbles and periodic vortex shedding in the wake would occur, as indicated in previous studies [75]. However, it is important to note that the behavior of these phenomena can significantly differ as the Reynolds number transitions from $Re = 15000$ to $Re = 50000$. This study underscores that these phenomena had minimal impact on the lift excursions of the blades during the blade crossover event. Furthermore, it is worth noting that quantifying the reduced time for blade crossover suggests that these results might apply to a broader range

of Reynolds numbers that haven't been tested yet. To confirm this, additional experiments spanning different Reynolds number ranges are necessary.

However, the effects of the Reynolds number can be substantial when considering the drag characteristics of the blades. The formation of laminar separation bubbles and vortex shedding in the wake can potentially alter the pressure drag experienced by the blades. Additionally, a change in the Reynolds number can influence skin friction drag. These factors collectively contribute to variations in drag characteristics during the blade crossover. It is crucial to acknowledge that the current load cells used in this study lacked the sensitivity required to measure these drag coefficient variations, particularly at low angles of attack. As a result, conducting further experiments with more sensitive load cells is imperative to comprehensively understand the drag variations during blade crossover at different Reynolds numbers.

The effects of Reynolds number on airfoils undergoing unsteady motion have attracted interest due to the increased application of micro air vehicles, which operate at relatively low Reynolds number conditions. Badrya [84] showed that the lift response of a pitching NACA0012 airfoil at low Reynolds number conditions of $Re = 10000$ follows a close trend with the predictions made by Theodorsen's [85] inviscid formulation. Although some high-frequency oscillations occurred during the acceleration and deceleration peaks, the general trend was closely matched. These observations suggest that, at low Reynolds numbers, while the general trend in the blade crossover events resembles that of high Reynolds number conditions, it might exhibit additional high-frequency oscillations. These oscillations might be important during the post-crossover phase, where the system responds to the impulsive perturbations imparted to the system by the blade crossover event. A further detailed analysis of the system response due to blade crossover event is required to fully understand these effects.

6.4.2 Effects of blade thickness to chord ratio and airfoil curvature effects

The effects of blade thickness and airfoil shape on load characteristics during unsteady flow conditions, such as pitching airfoil and gust interactions, have been studied in a few literatures [86, 87, 88]. These studies have highlighted a strong dependence of airfoil thickness and

shape on the unsteady load response. For example, Motta [87] numerically studied the influence of blade thickness on the load response of a pitching airfoil at low angles of attack. He considered NACA symmetric airfoil with a thickness ranging from 4% to 24% of the blade chord. The results were compared with Theodorsen's [85] lower-order unsteady aerodynamic model, which predicts the loads for a thin flat plate undergoing unsteady maneuvers. Some of the assumptions associated with this model are that the perturbations are of small amplitude, the flow is attached, and the Kutta condition at the trailing edge is satisfied.

Motta [87] observed that the results from the NACA0004 airfoil matched well with the predictions made by Theodorsen's function. However, the deviations from the theoretical predictions increased with increasing the airfoil thickness. These variations were attributed to the change in the circulatory component of the lift, which implies that the blade thickness mostly affects the circulatory aspect of the total lift. For current conditions, as the blade thickness to chord ratio increases, the fluid displaced by the translating blades increases. This could result in higher downwash and upwash effects for blades 1 and 2, respectively. These variations could ultimately modify the circulatory lift experienced by the other blade and vary the load characteristics.

Similarly, Lysak [88] numerically studied the variation in the lift response of a flat plate and NACA 65 series airfoils with an elliptical leading edge to the step gust input. He observed that the flat plate experienced an abrupt change in its lift response as the gust interacted with its leading edge. This abrupt change in lift response was smoothed out for NACA 65 series airfoil due to the leading edge curvature effects. As a result, the NACA 65 series airfoil experienced an earlier onset of the gust interaction effects. Similar effects can also be expected for the blade crossover event when the airfoil shape varies.

To explore all of these effects, three blade sections were considered: (1) flat plate, (2) NACA0012, and (3) NACA0018. These blades had the same chord length of $c = 0.036m$. The flat plate had a blade thickness ratio of 6%. This was due to the manufacturing challenges of producing flat plates with lower thicknesses and the decreased aerodynamic efficiency linked to thicker flat plates, particularly under these low Reynolds number conditions. Figure. 6.8 shows the variation in the excursion in the coefficient of lift (δC_l) for these three cases. These plots

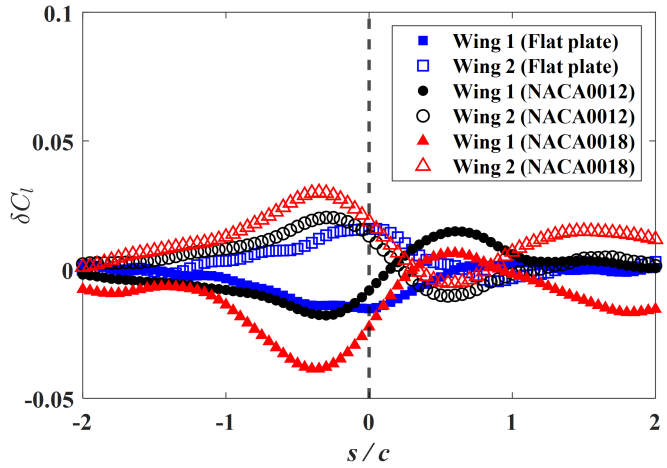

Figure 6.8: The variation in the lift coefficient for a flat plate, NACA0012 airfoil profile blades, and NACA0018 airfoil profile blades.

were averaged between the Reynolds number of $Re = 15000, 25000$, and 35000 for each case. The results show that the blades with symmetric NACA airfoil profiles do, in fact, experience an earlier onset of blade crossover effects similar to the observations made by Lysak [88] in his gust interaction study. In addition, the comparison shows that an increase in thickness results in higher excursions. To further quantify excursions due to thickness effects, the magnitude of maximum excursion in the coefficient of lift ($\delta C_{l_{max}}$) and its location were extracted from all of these Reynolds number cases for both blades. The box plot in Fig. 6.9 summarizes the results.

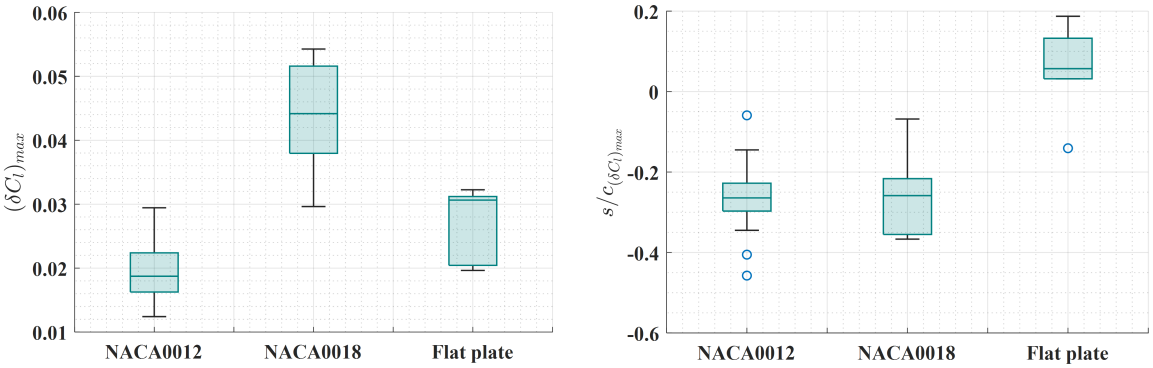

(a) Maximum excursion (b) Location of the maximum excursions

Figure 6.9: Variation in the magnitude of the maximum excursions in the coefficient of lift and its location relative to the crossover location.

The mean value of $\delta C_{l_{max}}$ showed a nearly two-fold increase, rising from 0.019 to 0.045, when the blade thickness ratio increased from 12% to 18%. This suggests a clear dependence of the load excursion characteristics on blade thickness. This is on par with the earlier discussion about the increased upwash and downwash effects due to an increased blade thickness. Increased lift excursions with blade thickness could be due to the change in the circulatory component, similar to the observations made for pitching airfoil by Motta [87]. The quantification of the circulatory and non-circulatory components on these observed load excursions will require further experimentation and analysis in the future. Despite the differences in maximum blade thickness between NACA0012 and flat plate blades, the magnitudes of excursions experienced by the flat plates were similar to NACA0012 airfoil blades. More experiments are required to explore this phenomenon.

The effects of airfoil curvature were also apparent in Fig. 6.9b, which shows the location of the initial peak excursions. For NACA0012 and NACA0018 cases, the peak occurred before the point where the quarter chords of the two blades aligned ($s/c = 0$), and the location of $\delta C_{l_{max}}$ didn't show significant changes between these two cases. This observation could be attributed to the symmetric nature of both blades, with their maximum thickness occurring at 30% of the chord length. However, $\delta C_{l_{max}}$ for the flat plate was located aft of $s/c = 0$. These differences can be attributed to curvature effects, suggesting that blade curvature also plays a significant role in shaping load characteristics during blade crossover events.

The results emphasize the fact that the effects of blade thickness and curvature effects are important considerations for modeling tools that predict the lift response during the blade crossover event. While developing a lower-order analytical model based on Theodorsen's formulation is possible, the underlying assumption of an infinitesimally thin flat plate could be problematic, as the rotorcraft employ airfoils with a finite thickness. However, it has been shown that the effects of blade thickness can be accounted for by adding corrections to Theodorsen's flat plate formulation. For instance, using a conformal mapping technique, Kussner [89] computed a set of modified Theodorsen's functions for Joukowsky airfoils.

Recently, Motta [87] observed that Theodorsen's function scaled with the blade thickness as the blade thickness varied from 4% to 24% for NACA symmetric airfoil. These empirical

scaling factors resulted in excellent agreement between Theodorsen's predictions and the numerical results. Lysak [88] also showed that an exponential correction to the flat plate gust response function, i.e., Sears function [90] (modified from Theodorsen's function), improved the theoretical predictions of the NACA 65 series airfoils. These results from the past literature show overwhelming evidence that the effects of blade thickness and airfoil shape can be accounted for through modifications to the lower-order models formulated for infinitesimally thin flat plates. This reduces the complexity of modeling approaches for blade crossover problems and potentially reduces the computational cost significantly.

6.4.3 Effects of steady-state lift coefficient

The preceding results have demonstrated that the blade profile and thickness significantly influence blade loads during blade crossovers. However, when the steady-state lift coefficient was zero, these load characteristics were symmetric for both the bottom and top blades (Blades 1 and 2). However, these load characteristics are expected to exhibit different behaviors when introducing a steady-state lift. The introduction of blade-bound circulation leads to additional upwash and downwash effects between the blades, potentially resulting in varying load characteristics. A close analogy can be drawn to airfoil interactions with vortical gusts to predict the load behaviors during blade crossover at finite steady-state lift conditions.

Many studies focusing on airfoil interactions with vortical gusts have established that when a counter-rotating vortex approaches an airfoil, it induces upwash onto the airfoil [91, 92, 93]. Hufstedler conducted an experiment in which he measured the lift response of a NACA0012 airfoil in the presence of a translating vortex in close proximity [93]. This vortex had clockwise and counterclockwise rotational directions, and the pitch angle of the blades was varied. The vortex was positioned at a finite distance above the airfoil. Notably, the interactions with a counter-rotating vortex could have analogous effects as the interactions between translating blades with finite pitch angles, as the bound circulation of the blades can be effectively modeled as a counter-rotating vortex.

In Hufstedler's experiment [93], as the vortex approached the blades, it caused an increase in their lift. However, as the vortex passed above the blades, the lift decreased to values below

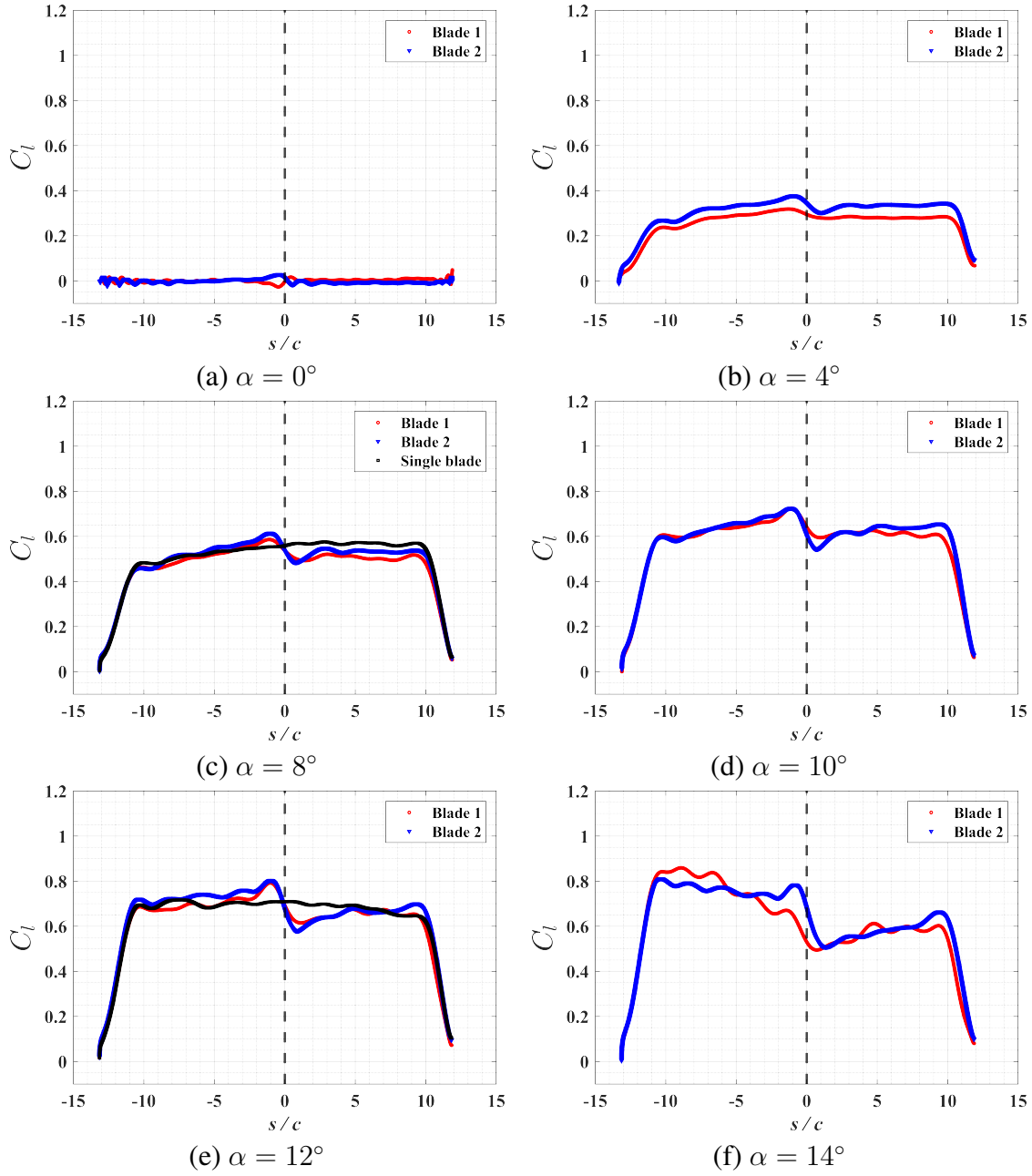

(a) $\alpha = 0°$ (b) $\alpha = 4°$

(c) $\alpha = 8°$ (d) $\alpha = 10°$

(e) $\alpha = 12°$ (f) $\alpha = 14°$

Figure 6.10: Variation in the coefficient of lift for Blade 1 and Blade 2 during the blade crossover at different angles of attack and the Reynolds number of $Re = 25000$.

the steady-state lift. Subsequently, the lift gradually recovered to the steady-state level as the vortex moved farther away from the blades. These influences were consistent across all blade pitch angles. The rate of lift recovery was contingent on the strength of the vortex, with a stronger vortex resulting in a longer recovery period. Given these findings, it is reasonable to expect similar influences and lift behavior during the blade crossover between blades with finite pitch angles. To investigate these effects, the pitch angle of the two blades was varied within the range of $\alpha = 0°, 4°, 8°, 10°, 12°$ and $14°$ and the resulting load characteristics during blade crossover are summarized in Fig. 6.10.

During the blade crossover at non-zero pitch conditions, both blades experienced an initial increase in the lift coefficient before $s/c = 0$. This was followed by a decrease in the lift coefficient in both blades close to and after $s/c = 0$. These behaviors were similar to the airfoil interactions with a translating vortex rotating counterclockwise and suggest that there is some analogy between the blade crossover problem and the vortical gust interaction problem. To better understand the underlying flow phenomena responsible for these load characteristics, the flow characteristics during the blade crossover test case of $\alpha = 8°$ at the Reynolds number case of $Re = 25000$ were analyzed. Figure 6.11 provides an overview of the flowfield before, during, and after the blade crossover.

The initial increase in the lift coefficient in both blades before the crossover can be attributed to the strong upwash induced by each blade's bound circulation effects on the other blade. This phenomenon is clearly visible in Figure 6.11a and results in an increase in the effective angle of attack, consequently increasing the lift. These upwash effects are also visible in the velocity profiles extracted at $0.5c$ distance above and below the two blades at an instance of $s/c = -0.5$. The results are shown in Fig. 6.14 and Fig. 6.13. Here, significant increases in the x and y-component of velocities were observed towards the leading edge of the two blades (refer to Fig. 6.14c and d and Fig. 6.13a and b). These effects are schematically represented in Fig.6.12, which shows the induced upwash effects due to the presence of bound circulation.

As the blades start aligning against each other, it is assumed that the top blade effects on the bottom blade are mainly concentrated on the bottom blade suction side. Similarly, the effects of the lower blade are concentrated on the pressure side of the top blade. This is a fair assumption

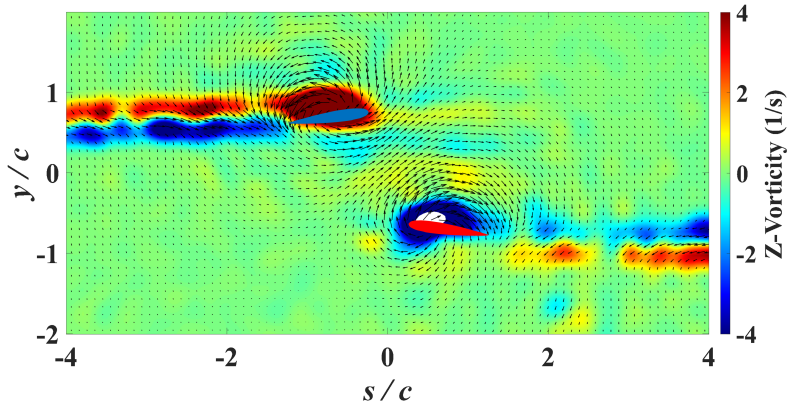

(a) $s/c = -0.5$

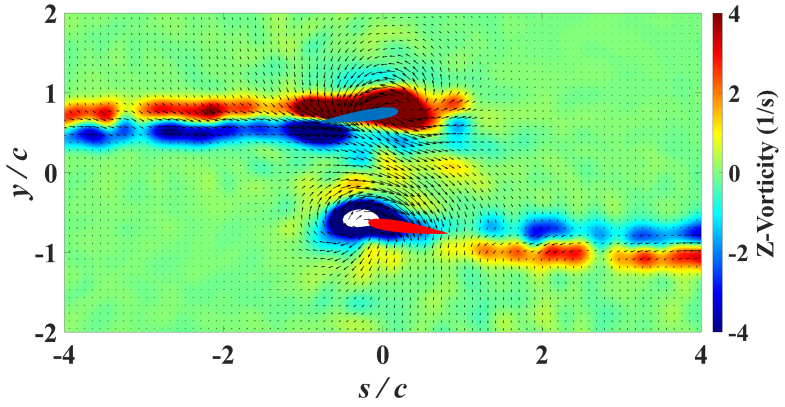

(b) $s/c = 0$

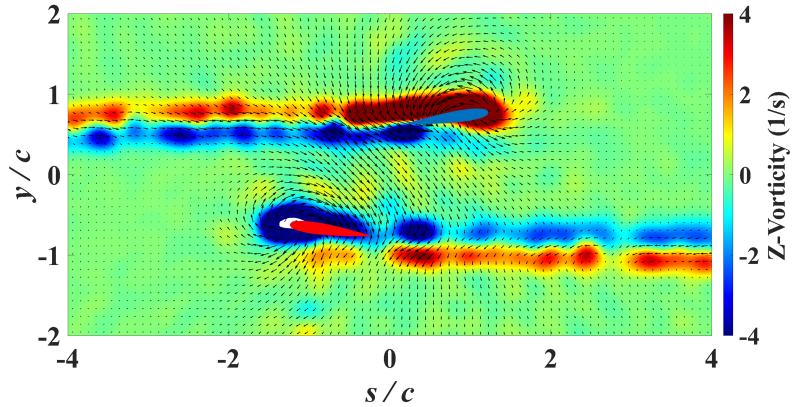

(c) $s/c = 1$

Figure 6.11: Flowfield evolution between the blades during blade crossover event for $\alpha = 8°$ and Reynolds number of $Re = 25000$.

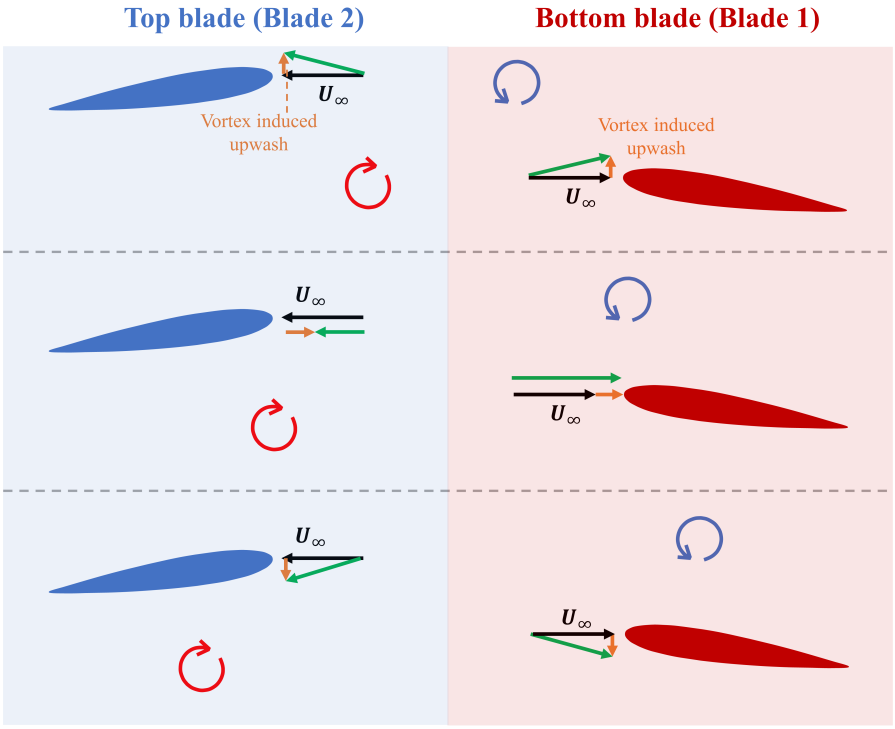

Figure 6.12: Schematic representation of the bound circulation effects of the blades during blade crossover. The bound circulation of the other blade is represented as a vortex, which is analogous to the vortical gust interaction of the blades. The velocity vectors are not to scale.

given the no penetration boundary condition due to the blades' presence. The velocity profiles above and below the two blades were examined to further confirm this. The velocity profiles above the top blade (Blade 2) and below the bottom blade (Blade 1) were largely invariant with respect to the blade crossover event (refer to Fig. 6.14a and b and Fig. 6.13c and d). The changes in velocities below the top blade and above the bottom blade were much more significant, suggesting that the changes in blade loads during the blade crossover are majorly due to the changes in flowfield in the pressure and suction sides of the top and bottom blades, respectively. The contribution of these variations on the lift characteristics is discussed next.

As the blades get closer, the upwash effects due to the bound circulation start to reduce, as shown in Fig.6.12.

As the quarter chords of the blades align (at $s/c = 0$), the bound circulation of the upper blade (Blade 2) induces downwash on the lower blade (Blade 1). These effects are also reflected in the extracted velocity profiles at $0.5c$ distance above Blade 1. The magnitude of the x and y-component of velocities was observed to increase in a rightward and downward direction,

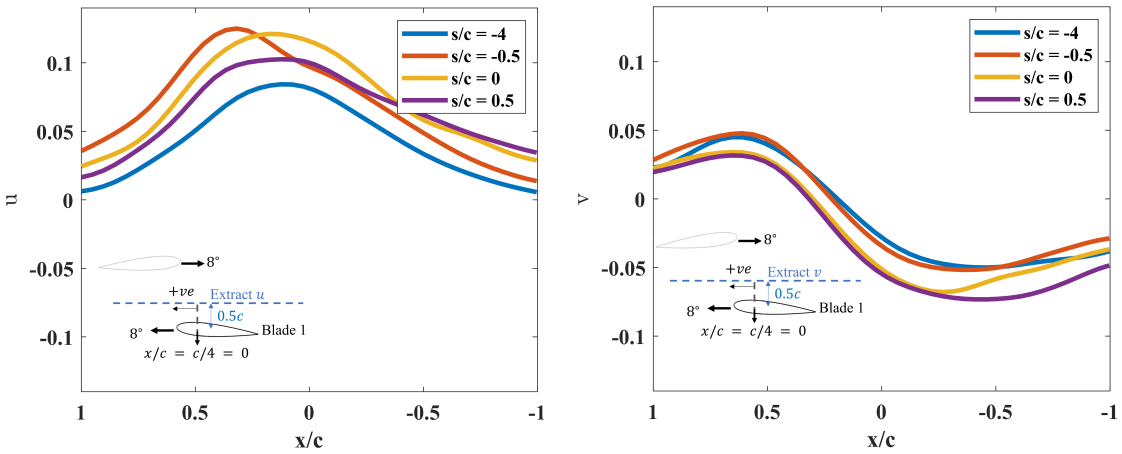

(a) u-velocity above Blade 1

(b) v-velocity above Blade 1

(c) u-velocity below Blade 1

(d) v-velocity below Blade 1

Figure 6.13: Extracted velocity profiles above and below Blade 1 before, during, and after the blade crossover at the Reynolds number case of $Re = 25000$ and the pitch angle of $\alpha = 8°$.

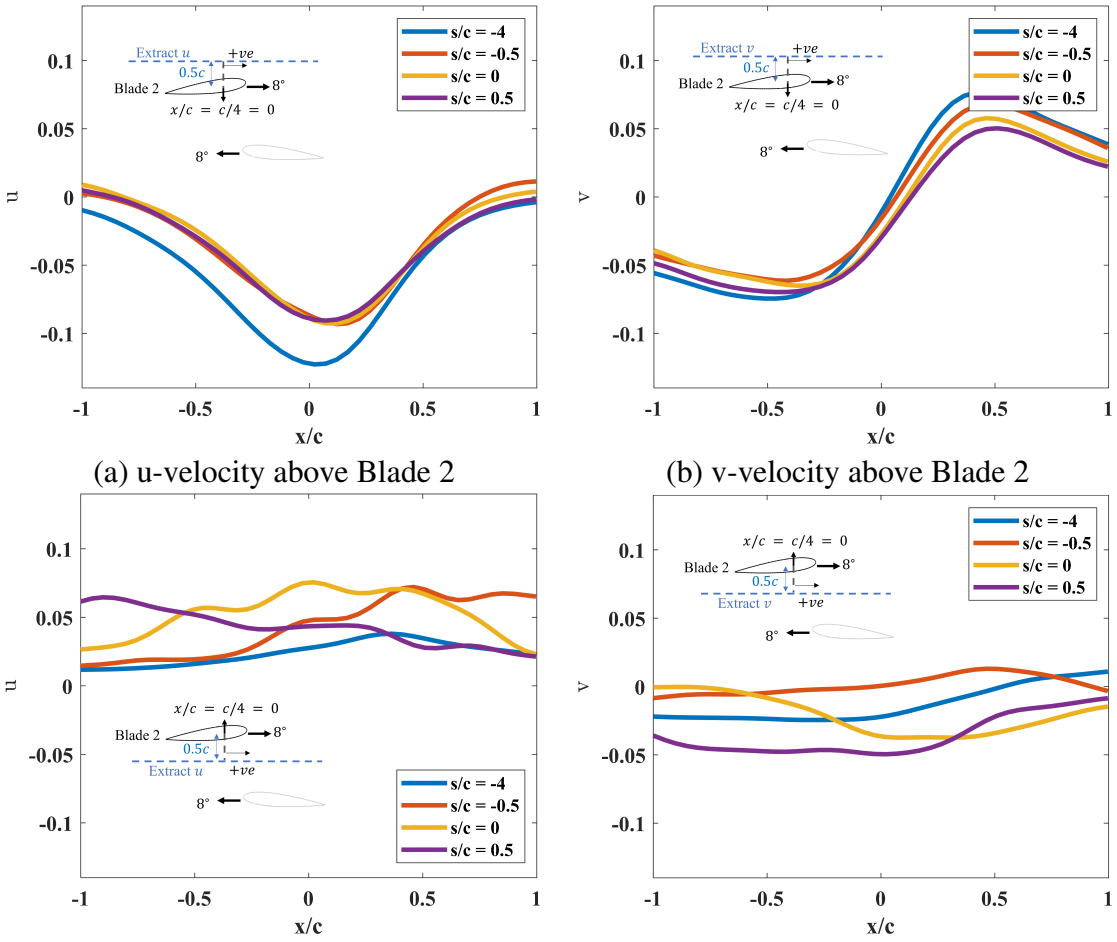

(a) u-velocity above Blade 2

(b) v-velocity above Blade 2

(c) u-velocity below Blade 2

(d) v-velocity below of Blade 2

Figure 6.14: Extracted velocity profiles above and below Blade 2 before, during, and after the blade crossover at the Reynolds number case of $Re = 25000$ and the pitch angle of $\alpha = 8°$.

respectively. These effects result in a reduced effective angle of attack of the bottom blade, resulting in decreased lift. These effects persist and become more pronounced as the blades continue translating, as seen in Figure 6.11c. This leads to the observed minimum peak in lift coefficient for Blade 1 right after the $s/c = 0$ location. Figure 6.12 shows a conceptualized schematic of how the downwash from the bound circulation from the top blades results in reduced blade angle of attack.

Additionally, as the blades aligned, the bottom blade-bound circulation-induced effects also induced downwash on the top blade. This concept is illustrated in Fig. 6.12. This is further substantiated by the velocities extracted at the location of $0.5c$ below the top blade. As seen in Fig. 6.14c, the x-component of velocity does increase in the translation direction, and the blade experiences additional downwash as the blades align against each other. The consequence is that the lift produced by the top blade also started to reduce as the blades aligned. As the blades travel further from each other, these effects reduce, and the lift starts to recover to the steady-state value.

The same mechanism contributes to the observed load behavior at all the pitch angles above $\alpha = 0^\circ$ and below stall. While the mechanisms remain the same, some differences were observed between these cases. For instance, the lower blade (Blade 2) at $\alpha = 4^\circ$ did not show significant influence from the crossover event compared to the other pitch angle cases. Similarly, for $\alpha = 0^\circ, 4^\circ, 8^\circ$ and 10°, the lift coefficient values after the crossover slowly returned to the initial values. However, after the crossover, a significant drop in the lift coefficient was observed for the $\alpha = 12^\circ$ case. This is indicative of an induced stall due to the blade crossover event. The upcoming sections provide a discussion on these observed effects.

Peak load excursions and their behavior

The peak excursions from the steady lift during the blade crossover event were extracted for each blade with the NACA0012 airfoil profile section at different angles of attack to quantify the variations. The results were averaged between the Reynolds number cases of $Re = 15000, 25000$. The $\delta C_{l_{peak}}$ and $(s/c_{\delta Cl_{peak}})$ were extracted, and the results are plotted in Fig. 6.15.

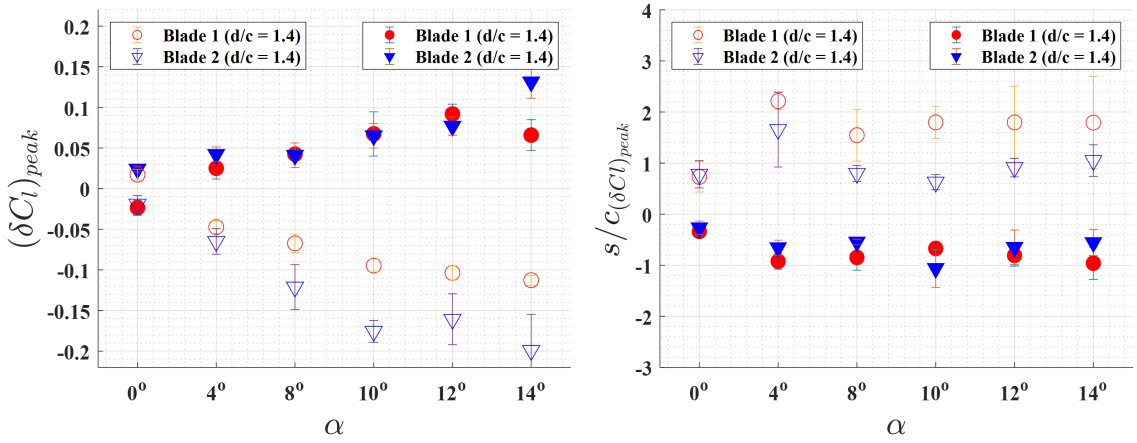

Figure 6.15: Variation in the (a) peak excursion values in the coefficient of lift and (b) location of the peak excursions at different angles of attack. Shaded markers represent the peak excursions and their location before the crossover, and non-shaded markers represent peak excursions and their location post-crossover.

The filled markers in this figure represent the properties of the peak excursions before $s/c = 0$, and non-filled markers represent peak excursion properties aft of $s/c = 0$.

The $\delta C_{l_{peak}}$ at $\alpha = 0°$ for the two blades were equal and opposite. This signifies the symmetric interactions between the blades with zero steady state-lift. As the pitch angle increased, the magnitude of the peak excursions before and after $s/c = 0$ was observed to increase linearly with the increase in the pitch angle. This is attributed to the increase in blade-bound circulation with increasing pitch angle. This result suggests that there might be a linear supposition of the pitch angle effect on the load characteristics during blade crossover. A simple linear superposition of the pitch angle effects simplifies the modeling approach, as the existing lower-order models are currently based on the linear superposition theory (for example, Theodorsen's formulation [85]). Some modifications of these linear unsteady theories can be used for modeling the blade crossover effects with a linear superposition of the pitch angle effects.

Despite the linear increase in peak excursions with pitch angle, notable differences were observed between the two blades and the peak excursion properties before and after $s/c = 0$. For instance, at $\alpha = 4°$, the magnitude of the peak excursions before $s/c = 0$ differed between Blade 1 and Blade 2, while the differences were minimal for higher pitch angles of $\alpha = 8°, 10°$ and $12°$.

At $\alpha = 4°$, the peak excursion values for the bottom blade (Blade 1) were lower than for the top blade (Blade 2). Here, the effects of bound circulation might not have been strong enough to counteract the blade thickness effects. As discussed earlier, blade thickness effects contribute upwash to the upper blade and downwash to the lower blade as they approach each other, resulting in an initial outward force on both blades. For the top blade (Blade 2), the upwash due to the lower blade's bound circulation added to the upwash due to thickness effects, increasing the effective angle of attack. However, the downwash from the upper blade's thickness to the lower blade counteracted the upper blade's bound circulation effects. This is why a difference in $\delta C_{l_{max}}$ was observed between the two blades at $\alpha = 4°$. As the pitch angle increased towards the stall angle of $\alpha = 12°$, the influence of bound circulation became dominant. Consequently, the differences in peak excursion magnitudes between the two blades decreased before $s/c = 0$.

The magnitude of ($s_{\delta Cl_{peak}}$) before $s/c = 0$ initially increased when pitch angle increased from $\alpha = 0°$ to $\alpha = 4°$. The induced upwash effects due to the blade-bound circulation result in the blades experiencing the effects to each other earlier than the crossover case at $\alpha = 0°$. This results in the earlier peak excursions during a crossover with an initial condition of finite bound circulation. As the pitch angle increased, the location of this peak excursion before $s/c = 0$ did not change significantly, suggesting that the increase in bound circulation only increases the magnitude of the upwash effects but not the region of influence of one blade to the other.

A significant difference in the peak excursion behavior after the $s/c = 0$ location was observed between the two blades. The magnitude of the peaks was higher for the top blade (Blade 2) than the bottom blade (Blade 1). The location of the peak for the top blade (Blade 2) was also closer to the $s/c = 0$ location compared to that bottom blade (Blade 1). As the blades aligned against each other, the upwash effects began to diminish. Concurrently, the top blade induced a substantial downwash on the suction side of the bottom blade, while the bottom blade effects act to reduce the net dynamic pressure of the flow. The current observations suggest that among these two influences, the effect of the bottom blade on the top blade is stronger than the influence of the top blade on the bottom. To confirm this, the drag and moment coefficient of the two blades were also analyzed for the crossover case at $\alpha = 8°$.

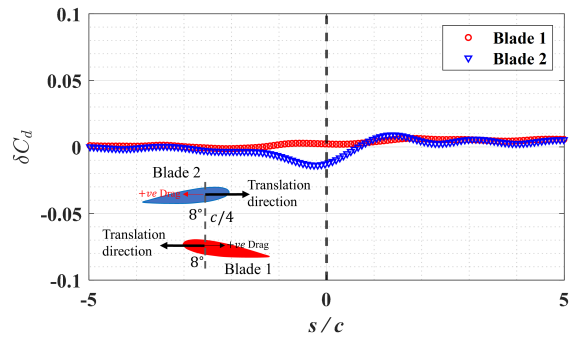

(a) Drag coefficient excursions

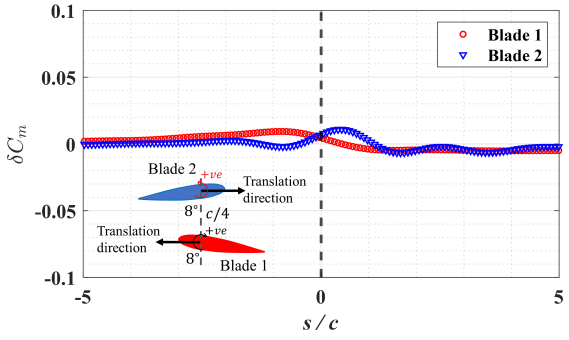

(b) Moment coefficient excursions

Figure 6.16: Excursions in the drag and moment coefficient during the crossover at $\alpha = 8°$. The insets represent the operating conditions and the directions of the drag and moment for each blade.

Figure 6.16 shows the excursions in the drag and moment coefficient of the two blades, which were extracted by subtracting the isolated blade results. While the drag of the bottom blade (Blade 1) did not show any measurable change during the crossover, the top blade (Blade 2) showed an initial reduction in the drag before $s/c = 0$, followed by a rise after $s/c = 0$. The changes in the moment coefficient were also more pronounced for the top blade (Blade 2) than for the bottom one. Before $s/c = 0$, the bottom blade (Blade 1) experienced a slight pitch-up moment about the quarter chord, followed by a pitch-down moment after $s/c = 0$. On the contrary, the top blade (Blade 2) experienced an initial pitch-down moment before $s/c = 0$, which was followed by a pitch-up moment after $s/c = 0$. These observations were consistent for both $\alpha = 4°$ and $\alpha = 10°$ cases, suggesting that the effects of the bottom blade on the top is more significant for cases with initial finite bound circulation.

Induced stall effects

The lift coefficient for the blade crossover at $\alpha = 12°$ (Fig. 6.15e) showed a significant drop in the lift coefficient after the crossover compared to other cases, which is indicative of induced stall. This is a plausible explanation, as the upwash effects induced by the blade-bound circulation might lead to a momentary stall effect, particularly at these high angles of attack. As such, the drag and moment characteristics of the blades were examined to study this phenomenon

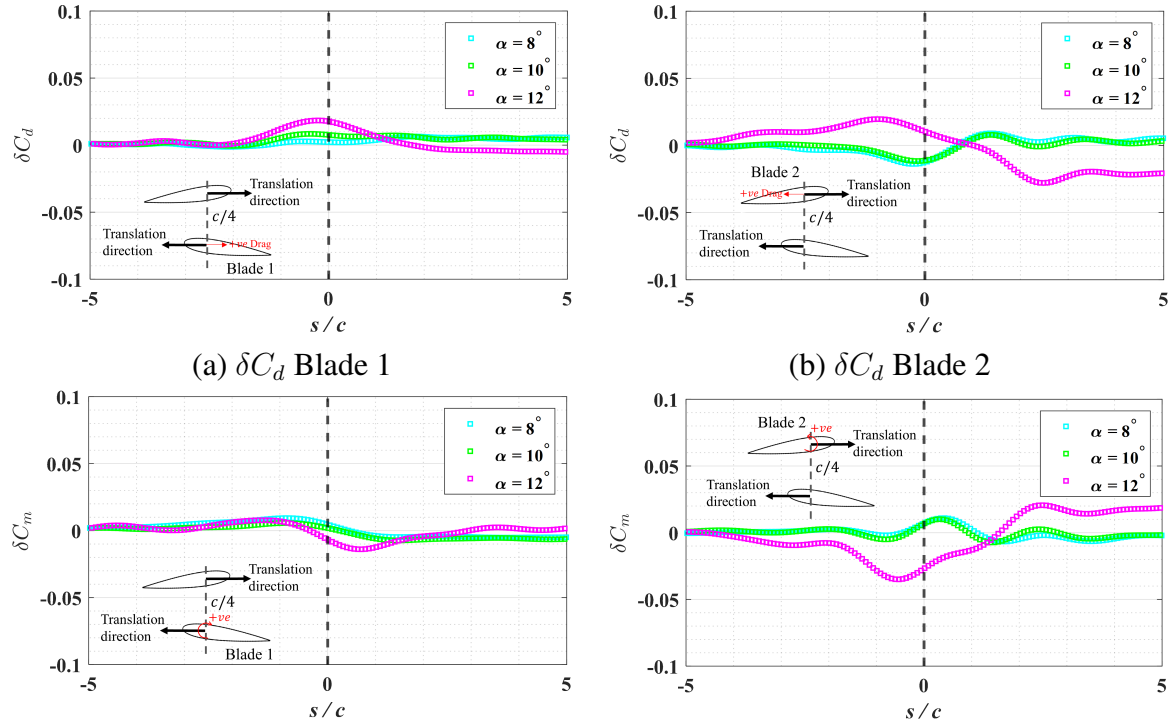

(a) δC_d Blade 1

(b) δC_d Blade 2

(c) δC_m Blade 1

(d) δC_m Blade 2

Figure 6.17: Excursions in the drag and moment coefficient during the crossover at $\alpha = 8°, 10°$ and $12°$. The insets represent the operating conditions and the directions of the drag and moment for each blade.

further. Figure 6.17 shows the excursions in the drag and moment coefficient for Blades 1 and 2 at $\alpha = 8°, 10°$ and $12°$ blade crossover cases.

The behavior of the drag and moment coefficients for the top blade during the crossover at $\alpha = 12°$ in Figure 6.17 differs from that at $\alpha = 8°$ and $10°$. For instance, at $\alpha = 8°$ and $10°$, the drag for the top blade decreased before s/c = 0, then began to increase after $s/c = 0$. However, at $\alpha = 12°$, the drag substantially increased before $s/c = 0$, then decreased after $s/c = 0$. The moment at $\alpha = 8°$ and $10°$ exhibited an initial pitch-down before $s/c = 0$, followed by an increase in the pitch-up moment peaking after $s/c = 0$. In contrast, at $\alpha = 12°$, the top blade experienced a significant pitch-down moment, even greater than that at smaller angles of attack. After $s/c = 0$, the top blade experienced a high pitch-up moment, surpassing those at smaller angles of attack. These observations clearly indicate that the top blade experiences induced stall effects due to the bottom blade. These effects were only observed at a spacing of $d/c = 1.4$. Further studies are needed to investigate whether similar induced stall effects occur

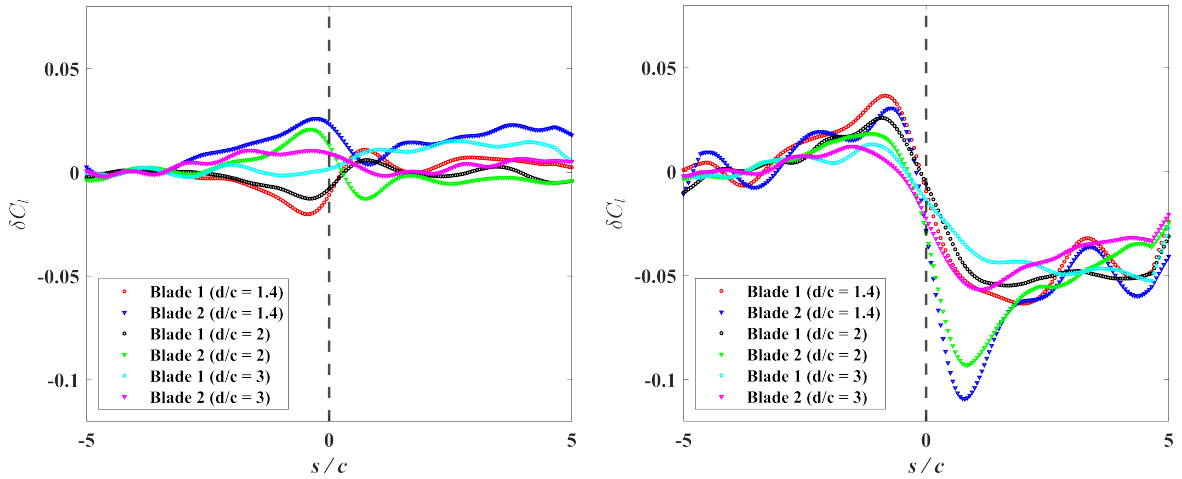

(a) $\alpha = 0°$ (b) $\alpha = 8°$

Figure 6.18: Variation in the blade loads at varying blade spacing.

at other blade spacings where the magnitude of the induced effects of the two blades on each other change.

At $\alpha = 8°$ and $10°$, the changes in the bottom blade (Blade 1) drag coefficient coefficients were not significant enough to be registered by the loadcells. However, the increase in the drag experienced by the bottom blade was more substantial for $\alpha = 12°$. The drag coefficient (δC_d) initially increased before $s/c = 0$ and reduced again to zero after the crossover. The pitch-down moment experienced by the bottom blade after $s/c = 0$ was also higher for the case of $\alpha = 12°$ when compared to that at $\alpha = 8°$ and $10°$. These results are indicative of induced stall characteristics for the bottom blade but are not substantial enough to claim that the bottom blade does, in fact, stall due to the top blade effects. The changes in the drag and moment of the bottom blade were not as significant as that of the top blade. Thus, further research is required to confirm if the bottom blade does, in fact, stall during the blade crossover when both blades were set at a pitch angle corresponding to the maximum lift coefficient ($\alpha = 12°$).

6.4.4 Effects of normalized blade spacing

As the spacing between the blades increases, the influence of the blades on each other is also expected to decrease. This section presents the influence of normalized blade spacing on the load characteristics. The spacing was changed as $d/c = 1.4, 2$ and 3. For brevity, only two

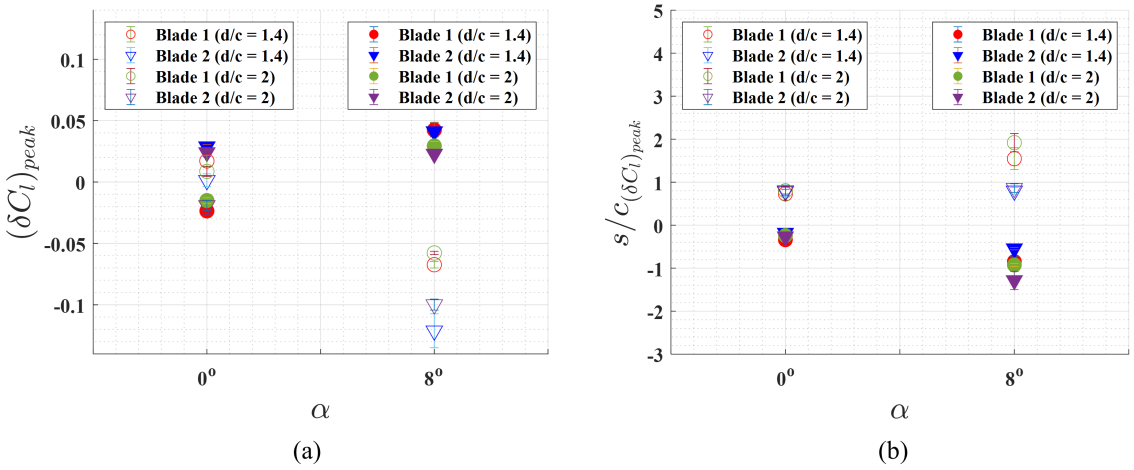

Figure 6.19: Variation in the (a) peak excursion values in the coefficient of lift and (b) location of the peak excursions at different blade spacing. Shaded markers represent the peak excursions and their location before the crossover, and non-shaded markers represent peak excursions and their location post-crossover.

cases of pitch angle, i.e., $\alpha = 0°, 8°$ were considered. Figure 6.18 shows the characteristics of the excursions in the lift coefficient for the bottom and top blades at different blade spacing. These plots were averaged over the Reynolds number cases of $Re = 15000, 25000$, and 35000. The effects of two blades onto each other do, in fact, reduce with increased blade spacing. This is consistent for $\alpha = 0°$ and $\alpha = 8°$. The peaks of the excursions before and after $s/c = 0$ and their locations were extracted from these plots for further analysis. The results are shown in Fig. 6.19.

The values of the peak excursions for both blades reduced as the spacing between the blades increased. As discussed earlier, the excursions observed before $s/c = 0$ during the crossover at $\alpha = 0°$ are due to the upwash and downwash effects of Blade 1 and 2 onto each other due to their thickness effects. The magnitude of these effects reduces as the spacing between the blades increases, mainly due to dissipation. Naturally, the magnitude of excursions would also reduce. However, the spacing doesn't influence the location of this peak excursion at $\alpha = 0°$ (refer to Fig. 6.19b). This is mainly because the location of the peak excursions depends on the curvature effects, as discussed earlier. Similar effects were observed for the higher pitch angle of $\alpha = 8°$ case. The magnitude of the peak excursions reduced with increasing blade spacing, but the excursions' location did not change significantly.

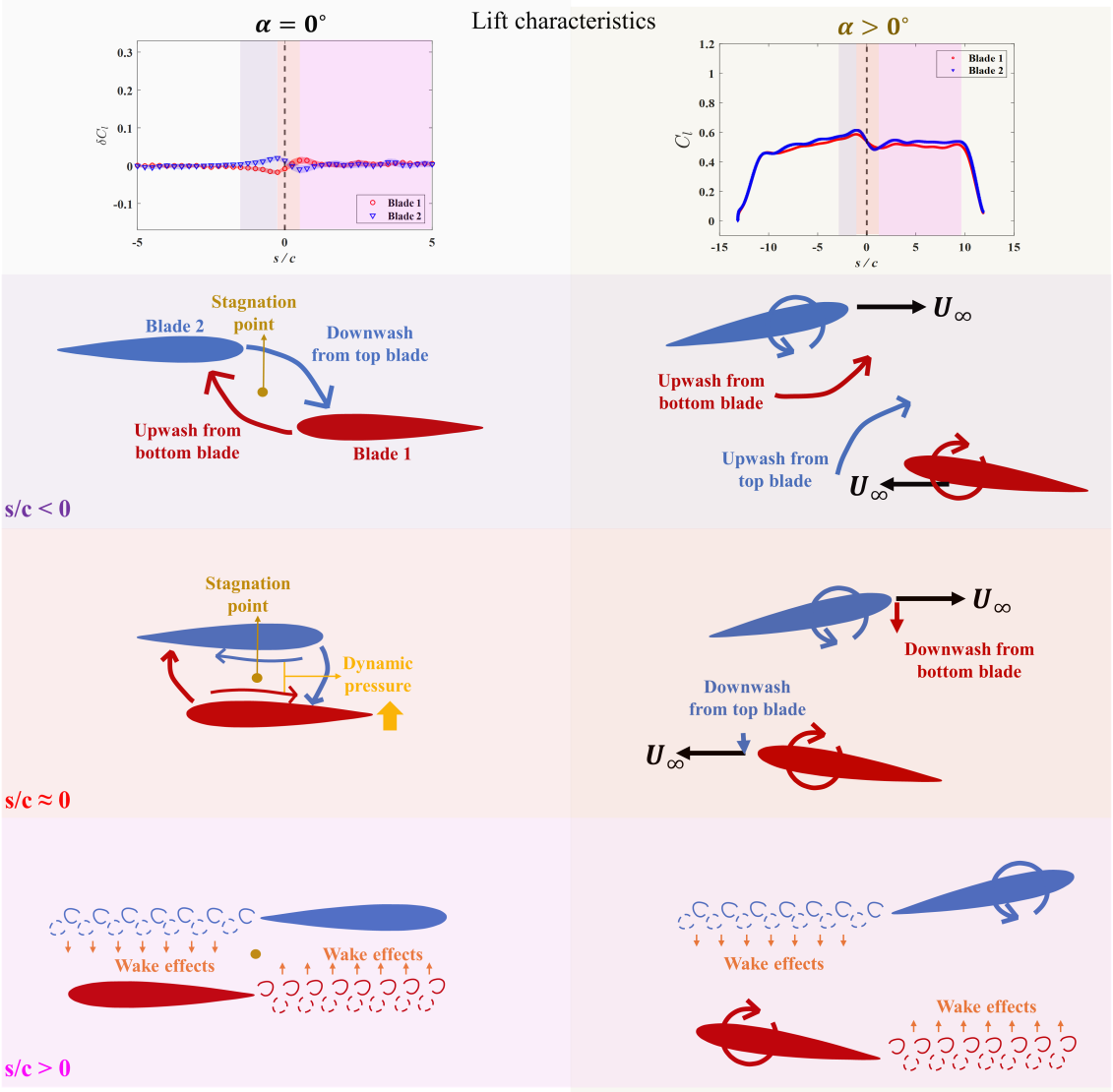

Figure 6.20: Summary of the observed load characteristics and contributing mechanisms for a symmetric airfoil.

6.4.5 Summary of the interactions during blade crossover

The findings thus far have revealed that the upwash and downwash effects induced by one blade strongly influence the load characteristics of the other during the blade crossover. Additionally, the flowfield behavior between the blades differed significantly between crossover cases with zero pitch angles and those with non-zero pitch angles. Specifically, a stagnation point was observed between the blades in the crossover case with a zero pitch angle, a feature not observed in cases with higher pitch angles. In such zero-pitch angle cases, the blade thickness effects were the dominant contributors to the load characteristics during the crossover. However, in

cases with higher pitch angles, the effects of bound circulation took precedence. This led to a substantial variation in the lift response of the blades during the crossover between the zero-pitch angle and the non-zero-pitch angle cases. While shed vortices in the wake were noted to interact with the blades after the crossover, these interactions were generally too subtle for the load cells to detect. This section summarizes the mechanisms contributing to the observed airload characteristics during the blade crossover as determined from the analysis so far. Figure 6.20 provides a schematic representation of the key mechanisms governing the lift response during the crossover.

The figure shows that at zero initial lift conditions, the two blades experienced an outward force compared to each other as they approached each other. This was due to the upper blade inducing downwash on the bottom blade and the bottom blade inducing upwash on the top blade. As the quarter chord of the blades aligned, the dynamic pressure of the suction side of the bottom blade and the pressure side of the top blade increased, resulting in inward force. This effect continued as the blades aligned against each other. As the blades translated farther away, the blades' interactions reduced, and the lift produced by each blade slowly recovered to the initial values.

For finite steady-state lift conditions, both blades experienced upward force as they approached each other. This was due to the induced upwash by the bound circulation of one blade to the other. As the blades aligned against each other, the blade-bound circulation reduced the effective angle of attack of the two blades. These effects resulted in both blades experiencing reduced lift as they aligned against each other. The lift slowly recovered to its steady state value as the blades translated farther away from each other.

The flowfield evolution between the blades was measured, and the velocity profiles near the top and bottom blades were extracted to understand these mechanisms. It was shown that the induced effects between the blades depended on factors like the blade's profile section, thickness, and spacing. Surprisingly, the Reynolds number effects were determined to be minimal on the general airload characteristics during the blade crossover. It was also shown that an analogy existed between the blade crossover problems and the problem with blade interactions with vortical gusts. Here, the lift response of the blades during the crossover and vortical

gust interactions exhibited similar characteristics. This observation suggests possibly modeling the blade crossover problem as a gust interaction problem. Further discussion on the matter is presented in the upcoming section.

6.4.6 Modelling approach for blade crossover

The findings thus far have highlighted the significance of blade thickness and bound circulation in influencing the blade load characteristics during blade crossover. These factors induce specific velocity profiles at the translation plane of the other blade, as illustrated in Figure 6.22a. These velocity profiles depend on blade thickness, airfoil curvature, and blade-bound circulation. This leads to a compelling question: can the blade crossover event be effectively modeled as a gust interaction problem, in which a translating blade interacts with the gust induced by the other blade? This section delves into the possibility of modeling the blade crossover and gust interaction problems.

First, it is assessed whether the unsteady effects play an important role during the blade crossover effects. Then, the potential use of the existing gust interaction model in the context of the blade crossover problem is explored.

Unsteady effects

The blade crossover problem is transient; thus, the unsteady effects are expected to influence the total blade load characteristics. But if the contribution of these unsteady effects is small, the blade crossover event can essentially be modeled as a quasi-steady problem by neglecting the unsteady effects. This reduces the computational complexity of solving the governing equation involving the temporal terms. A non-dimensional parameter called the reduced frequency ($k = \frac{\omega c}{2U_\infty}$) is usually calculated to get an indication of the unsteady effects on unsteady periodic aerodynamic problems. However, such a parameter does not currently exist for impulsive events such as blade crossover, which indicates the expected contribution of the unsteady effects. As such, the moving control volume approach, as discussed in the previous chapter, was employed to decompose the unsteady and convective effects from the total airloads experienced by the blades during the blade crossover problem.

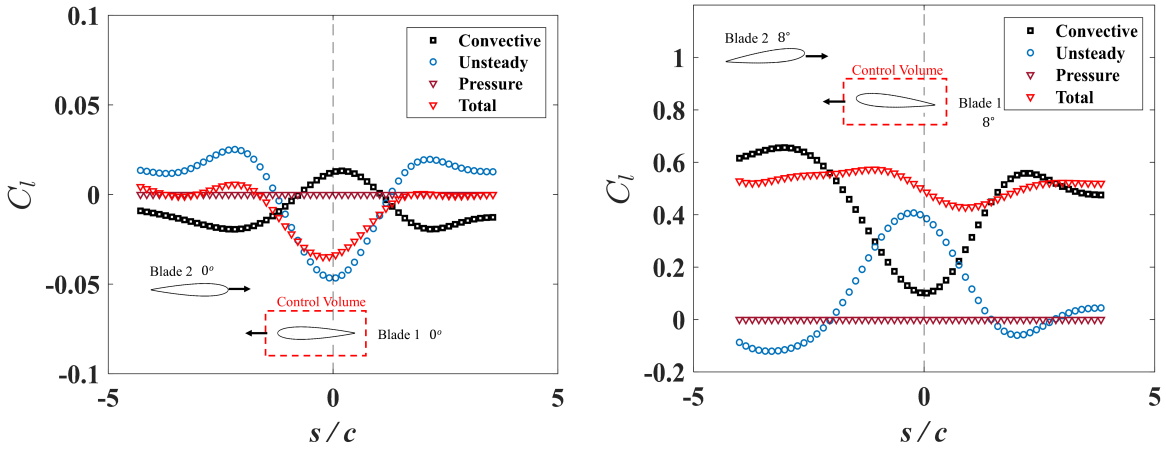

(a) Flat plate, $\alpha = 0°$ (b) NACA0012, $\alpha = 8°$

Figure 6.21: Decomposition of unsteady and convective effects for Blade 1 during a crossover between blades at pitch angles of $\alpha = 0°, 8°$. The inset represents the conditions under which the decomposition was carried out.

This analysis considered the crossover between the blades with the NACA0012 airfoil profile section. Two test cases were taken with pitch angles of $\alpha = 0°$ and $\alpha = 8°$. The moving control volume was applied to the bottom blade. The results are summarized in Fig. 6.21. The total lift response of the blades was a close match to the load measurements that have been reported previously. The results of the blade crossover case of $\alpha = 0°$ show that the unsteady effects significantly contributed to the total lift. The unsteady effects acted in the direction of the excursions, and the convective effect was always in the opposite direction to that of the unsteady effects. As expected, only the unsteady and convective terms contributed to the total lift, with near zero contribution from the pressure term.

Similar observations were made for the case of $\alpha = 8°$. However, the magnitude of change in the convective and unsteady terms was much higher compared to the case of $\alpha = 0°$. These observations show that the unsteady effects significantly contribute to the lift response during the blade crossover, and quasi-steady formulations will not be reliable.

Fortunately, Kussner's model, which predicts the load response of a thin airfoil interacting with a gust, is based on the unsteady aerodynamic theory and, thus, accounts for the unsteady effects. The upcoming part of this section describes the potential use of the Kussner model to predict loads during blade crossover.

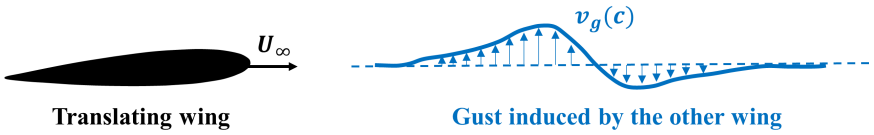

(a) Blade crossover analogy to gust interaction

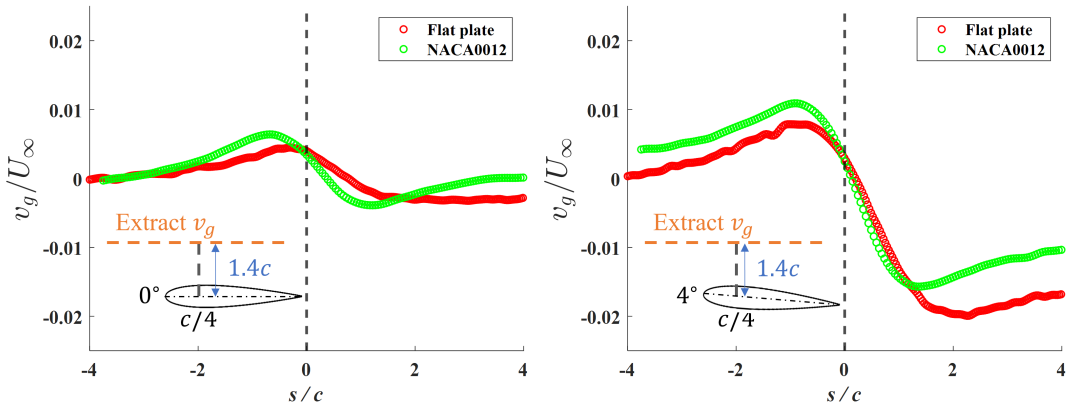

(b) $\alpha = 0°$ (c) $\alpha = 4°$

Figure 6.22: (a) Schematic representation of the interaction of a translating wing with gust induced by the other wing translating in the opposite direction. Normalized vertical velocity profile extracted at a distance of $1.4c$ above a translating wing (Flat plate and NACA0012) at angles of attack of (b) $\alpha = 0°$, and (c) $\alpha = 4°$. The insets in (b) and (c) show the schematic representation of the location where the velocities were extracted.

Kussner's model for blade crossover problem

Flowfield measurements were carried out for isolated translating flat plates and blades with the NACA0012 profile section for this analysis. The pitch angles of these blades were set at $\alpha = 0°$ and $4°$. Then, the velocity profile generated by these blades was extracted from the flowfield measurements at a vertical spacing of $d/c = 1.4$ above the blade chord line. These velocity profiles were extracted for a horizontal distance of $4c$ in front and behind the blade quarter chord location. Figure 6.22b and c show the extracted velocity profiles for these blades, and the insets represent the conditions under which these profiles were extracted. These velocity profiles were extracted for three Reynolds number cases of $Re = 15000, 25000$, and 35000 and were normalized by the translation velocity for each case, i.e., $U_\infty = 0.41, 0.69$, and $0.97\ m/s$ to find the gust ratio. As the normalized velocity profile variations between the three Reynolds numbers were minimal, the velocity profile shown in Figure 6.22b and c were averaged for the three given Reynolds numbers.

These velocity profiles were then treated as gusts interacting with a translating wing. The extracted gust profiles shown in Fig. 6.22 were fitted into a parameterized Kunnser's model to extract the lift response. These results were compared with the experimental data. A total of four experiments were carried out for comparison with the parameterized Kussner model:

1. Crossover between flat plates - both at $\alpha = 0^\circ$.

2. Crossover between flat plates - bottom blade (Blade 1) at $\alpha = 4^\circ$ and top blade (Blade 2) at $\alpha = 0^\circ$.

3. Crossover between blades with NACA0012 airfoil profiles - both at $\alpha = 0^\circ$.

4. Crossover between blades with NACA0012 airfoil profiles - bottom blade (Blade 1) at $\alpha = 4^\circ$ and top blade (Blade 2) at $\alpha = 0^\circ$.

These conditions were chosen to vary the gust profile by changing the blade curvature and the bound circulation. As the Kussner model is developed for thin airfoils operating at small angles of attack, the current analysis was only carried out for a flat plate and NACA0012 thin airfoil operating at low angles of attack. The results are summarized in Fig. 6.23.

The general load characteristics predicted by the Kussner model fall within the experimental results' standard deviation for $\alpha = 0^\circ$ and 4°. The model even captures the differences in the location of the first lift excursion peaks between the flat plate and NACA0012 airfoil blades for $\alpha = 0^\circ$ crossover case. For the flat plate crossover case, the first peak in lift excursion occurred after $s/c = 0$, while that for the NACA0012 airfoil profile crossover case occurred before $s/c = 0$. The magnitude of the first lift excursion peaks during the crossover also matched quite well between that predicted by the Kussner model and that from the experiments. This was true for both $\alpha = 0^\circ$ and 4°. However, the differences between the predicted loads and those from the experiments were apparent after $s/c = 0$.

These differences result from the Kussner model not accounting for the flow coupling between the gust and the body. Here, as the blades start to align against each other, the modification of the flowfield between the blades affects the load characteristics of both blades. This, in turn, would further modify the flowfield characteristics between the blades. As these effects are

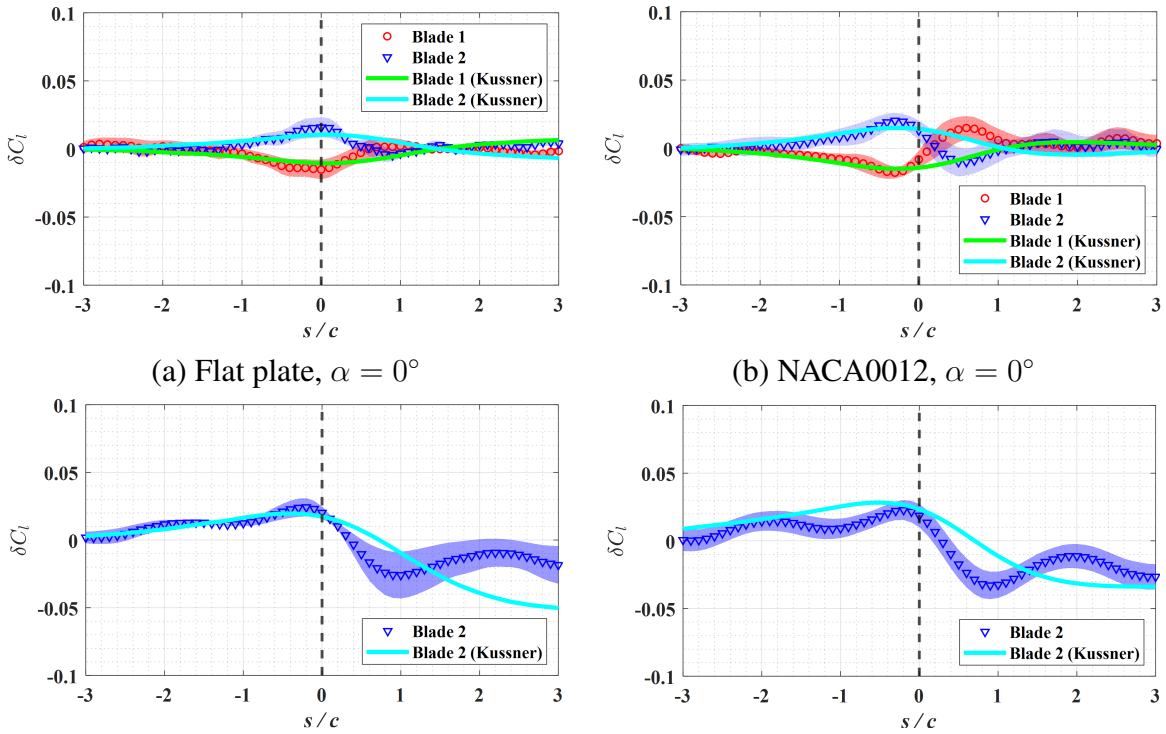

(a) Flat plate, $\alpha = 0°$

(b) NACA0012, $\alpha = 0°$

(c) Flat plate, $\alpha = 4°$

(d) NACA0012, $\alpha = 4°$

Figure 6.23: Comparison of the excursions in the lift coefficient between the experiments and results predicted by the Kussner model for predicting the gust interaction problems.

not accounted for in the Kussner model, its predictions start to fail as the blades align against each other during the crossover. The current Kussner model also does not model the system response to impulsive perturbations such as a blade crossover event. These factors also add to the deviation of Kussner's prediction from the experiments. However, the similarities between the results from the Kussner model and the experiments before $s/c = 0$ provide a possibility of modifying the Kussner model to adapt to the blade crossover problems. The modifications could either be empirical or a formulation of a new lower-order model based on Theodorsen's unsteady aerodynamic theory.

6.4.7 Future modeling considerations

The previous section showed that the Kussner model for the gust interaction problem provided close predictions of the lift response for the crossover problem, especially during the initial stages of the blade crossover. Kussner's model showed a good prediction of the initial peak experienced by the blades during blade crossover. While the predictions of the initial peaks provide useful information, these models might not be helpful in cases where the prediction of the post-crossover behavior is also required. In addition, there were also some limitations to using the existing gust interaction theories to model the blade crossover problem. These limitations are summarized below:

1. The extraction of the gust profile to model the blade crossover problem relied on experimental flowfield measurements. This is problematic as the gust profiles depend on blade geometric characteristics and suggests that this approach would require a database of induced gust profiles for various blade sections. This might not be computationally efficient.

2. The gust interaction model also doesn't account for the changes in the lift characteristics of the two blades during crossover due to their coupled interactions. These effects were shown to deviate the predictions from the actual measurements as the blades got closer to each other.

Despite these limitations, the previous section did exhibit that the lower-order unsteady aerodynamic theories, such as that developed by Theodorsen [85], do have a potential to predict the force responses. A similar approach can be followed to devise a solution for two thin airfoils translating in opposite directions and undergoing blade crossover. The non-circulatory contributions can be calculated by solving the unsteady Bernoulli's equation in the circle plane using conformal mapping. Similarly, the circulatory contributions can be calculated by imposing the Kutta condition at the trailing edge and solving the unsteady Bernoulli's equation. This formulation negates the need to extract gust profiles through experimental or numerical methods and could also capture the coupled interactions between the two blades. However, the underlying assumptions of this formulation could lead to unsatisfactory results. As such, this section discusses the implications of these underlying assumptions and important considerations to be accounted for to ensure the success of the potential prediction tool based on unsteady aerodynamic theory.

Blade geometric properties

The section on the discussion regarding the blade thickness and curvature effects (Section 6.4.2) has clearly shown that these parameters significantly influence the blade load characteristics during blade crossover. Given that real-world aerial vehicles with CCR employ blades with specific airfoil shapes and finite thicknesses, the modeling tool should have the capability of incorporating a custom airfoil profile. However, the proposed lower-order model based on the linear unsteady aerodynamic theory is for infinitesimally thin airfoils. Nevertheless, this model could serve as a starting point to obtain initial solutions, and modifications can be made to account for different blade sections. Examples of modifications to Theodorsen's formulation to account for different airfoil shapes have already been discussed in Section 6.4.2. A similar approach can also be followed for the blade crossover problem.

High pitch angle considerations

The success of the proposed lower-order model relies on satisfying Kutta conditions at the trailing edge. While this might be a fair assumption at low-pitch angles, these might not be

valid at higher-pitch angles close to stall [60]. The current analysis also shows that the blade crossover induces stall characteristics on the blades when blades operate at pitch angles close to the stall. The blade crossover event between blades that are already in a dynamic stall state, where there is a presence of a leading edge vortex, could yield different load characteristics. All these effects will result in a significant deviation of the predicted loads from the actual loads. These effects are highly non-linear in nature and are significantly harder to model. As such, while the proposed model could provide accurate predictions at low angles of attack, significant modifications will be required to improve the model's accuracy at high-pitch angles.

6.5 Summary

The effects of blade crossover were investigated in a hydrodynamic towing tank facility. This experimental setup involved translating two infinite blades in opposite directions, simulating a single-blade crossover event. The blade loads and flowfield were measured during the blade crossover. The loads were measured using strain gauge load cells, while particle image velocimetry was employed for flowfield measurements. To systematically explore the problem, Buckingham's π theorem was utilized to identify the relevant non-dimensional parameters that influenced the blade crossover event. The experiment's parametric study involved varying key factors, such as blade airfoil section, blade thickness, translation velocity, and pitch angles, to discern the impact of these non-dimensional parameters on the load characteristics.

Furthermore, the study explored the potential of modeling the blade crossover problem by drawing an analogy with the gust interaction problem. This approach sought to assess whether the complex interactions during blade crossover could be effectively understood and modeled through a comparison with the dynamics of a blade in a gust. The results of this comprehensive analysis are summarized as follows:

1. The blade airfoil profile section, blade thickness to chord ratio, non-dimensional blade spacing, and the blade steady-state lift were the important non-dimensional parameters that govern the blade crossover problem.

2. For zero pitch angles cases, where the steady-state lift is zero, the blade airfoil profile shape and blade thickness induced upwash and downwash on each other. These effects resulted in the observed load excursions.

3. The blade thickness mainly increased the magnitude of the excursions during the crossover, while the blade airfoil profile section affected the locations of the observed peak excursions.

4. For higher values of non-zero steady-state lift conditions, the bound circulation effects dominated the load excursion characteristics.

5. During the crossover at a pitch angle corresponding to the maximum steady-state lift coefficient, the upwash effects due to bound circulation resulted in induced stall effects on the blades.

6. Analogy to the gust interaction problem showed that the Kussner model predicted the general load characteristics only during the initial phase when the blades approached each other. After the blades aligned against each other, the model failed to capture the coupled interactions, and the predictions deviated.

7. The unsteady effects had a significant influence on the load characteristics during the blade crossover, which suggests that unsteady effects should be accounted for in the modeling approaches.

Chapter 7

Conclusions and future work

7.1 Conclusions and implications

In this thesis, two studies were carried out: (1) the investigation of the performance characteristics of counter-rotating coaxial rotor (CCR) hovering in in-ground effect (IGE) conditions, and (2) a fundamental study of the blade crossover effects on the blade airloads. The first study delved into the performance characteristics of counter-rotating coaxial rotors (CCR) when hovering near the ground. Analysis of the experimental data provided insights into the intricate aerodynamic interactions between the rotors and the ground. The second study focused on a fundamental examination of the effects of blade crossover on blade airloads. This study aimed to isolate the unsteady effects of blade crossover from other rotational and three-dimensional factors, allowing for an in-depth understanding of the underlying physics.

Here are some key conclusions and implications of these studies for the rotorcraft community:

7.1.1 Conclusions from CCR IGE study

1. The performance characteristics of the CCR in IGE closely mirrored those of a single, isolated rotor. Surprisingly, changes in rotor spacing, a key parameter, had a limited impact on the CCR's performance trend in IGE.

2. While the overall performance of CCR followed a trend close to the single rotor, further analysis revealed variations in the performance of the individual rotors. Although the general trend of individual rotor performance resembled that of a single rotor, distinct

deviations were evident, dependent upon the axial spacing between the rotors. In particular, these interactions resulted in the lower rotor experiencing a greater influence of ground proximity than the upper rotor. Consequently, the lower rotor negated some of the performance benefits the upper rotor would experience from the ground plane.

These observations have significant implications for the rotorcraft community, which are summarized below:

1. The current results suggest that the CCR performance varies similarly to a single rotor when operating in IGE. While this observation is intuitive, the current experimental results provide conclusive evidence for any future reference.

2. These findings simplify the complexity associated with modeling and predicting the overall performance behavior of CCR systems near the ground. By utilizing well-established single-rotor models, engineers and researchers can better understand and predict the performance of CCR systems in IGE, which is beneficial for rotorcraft design, optimization, and safety considerations.

3. The current comprehension of the interactions between the upper and lower rotors in CCR under IGE conditions serves as a foundational element for developing physics-based models to predict the performance characteristics of individual rotors in CCR when operating in IGE.

4. Comprehending these interactional effects is crucial for enhancing the handling capabilities of CCR configurations and mitigating the potential risks of accidents when operating in diverse in-ground effect (IGE) conditions. Due to the distinct influences of the ground on the upper and lower rotors, continuous adjustment to the yaw trimming for the CCR rotors becomes necessary during hovering in IGE. Neglecting this adjustment can lead to a momentary loss of vehicle control, which poses significant risks.

7.1.2 Conclusions from blade crossover study

1. The current study showed that the relevant non-dimensional parameters for the blade crossover problem were blade thickness-to-chord ratio, steady-state lift coefficient, and non-dimensional blade spacing. The thickness of the blade was found to influence the magnitude of airload excursions, while variations in the airfoil shape altered the locations of the peak excursions. As the initial steady-state lift coefficient of the blades was increased, the airload characteristics were dominated by the effects of bound circulation. In particular, altering blade spacing for a given blade only affected the magnitudes of blade airload excursion peaks without significantly changing overall airload characteristics.

2. The results from the crossover between blades at a pitch angle of 12° (corresponding to the maximum C_l) revealed that the interactions between the blades during the crossover event induced a stall on the top blade.

3. Using Kussner's model, which is designed to predict the lift response to a gust, the study aimed to evaluate the applicability of this model to the blade crossover problem. The results indicated good agreement between the Kussner model and the experimental data during the initial phase of the crossover event, with the model providing excellent prediction of the initial load peaks. However, as the blades aligned against each other, deviations between the model predictions and experiments became apparent. This deviation in the later stages of the crossover event suggests that coupling effects significantly influence blade airloads during this critical phase.

The importance of these findings and observations is summarized below:

1. By establishing these non-dimensional parameters, the study laid the foundation for systematic investigations across diverse operational conditions, mirroring the operational regimes of different Counter-Rotating Coaxial Rotor (CCR) vehicles. This characterization of parameters informs modeling approaches for the blade crossover problem in

full-scale CCR configurations. These induced stall effects can have substantial implications for CCR configuration vehicles, particularly in their vibrational and acoustic characteristics, especially when operating under high thrust conditions. Understanding and mitigating these effects is essential for improving the performance and safety of CCR vehicles in practical applications.

2. The findings indicate that lower-order unsteady models hold promise in accurately predicting the load behavior during the crossover event. Specifically, if the main objective is to forecast the initial peak excursions and pinpoint their locations in the crossover event, even Kussner's model demonstrates a close approximation.

3. Although Kussner's model provides a reliable estimate in the initial phases of the crossover event, there is still a requirement for enhanced lower-order models that can predict the load response consistently across the entire blade crossover phase. The results underscore the potential for modifying existing lower-order unsteady models to better capture the coupled interactions between blades throughout the crossover. This approach simplifies the need to develop complex and computationally expensive predictive tools.

7.2 Recommendations for future work

1. Counter-rotating coaxial rotors in ground effect

   (a) The study utilized a three-bladed aerodynamic coaxial rotor thrust stand, and it's important to note that variations in parameters, such as the number of blades and blade twist, could potentially lead to different effects compared to those observed in the current study. Consequently, further experiments are necessary to accurately quantify the influence of these parameters on the characteristics of counter-rotating coaxial rotors when operating in ground effect. Expanding the scope of research to investigate these additional factors will contribute to a more comprehensive understanding of CCR behavior in ground effect conditions.

(b) To gain deeper insights into the underlying physics of these complex aerodynamic interactions, it's imperative to conduct simultaneous flow measurements alongside performance measurements. These flowfield measurements can provide valuable data on the aerodynamic characteristics and behavior of counter-rotating coaxial rotors when operating near the ground. This holistic approach will contribute to a more comprehensive understanding of the system's behavior and enable the development of more accurate predictive models.

(c) Indeed, it's crucial to investigate the influence of rotor-on-rotor interactions on outwash characteristics thoroughly. The outwash from a counter-rotating coaxial rotor system, especially when operating in ground proximity, can pose potential hazards to surrounding structures and objects. Understanding these interactions and their effects on outwash will be essential for safety assessments and design considerations.

2. Blade crossover studies

(a) While the experiments conducted under hover conditions with both rotor blades set at identical pitch angles are foundational, it's crucial to extend this research to explore how operational conditions in actual flight scenarios can influence the blade crossover phenomenon. Specifically, the impact of thrust offset and variations in collective pitch settings between the upper and lower rotors, common in counter-rotating coaxial rotor systems, should be a focus of future investigations. In addition, the influence of helical vortex structure shed in the wake of the CCR also needs to be considered for future studies.

(b) The experimental setup involved translating the two blades at equal and opposite velocities to mimic CCR hover conditions. However, replicating forward flight scenarios requires the blades to move at different velocities. This change in boundary conditions might introduce variations in airload characteristics, which warrant further exploration to comprehensively address the blade crossover effects on CCR systems in different flight modes.

(c) The observation of induced stall effects during blade crossover at high-pitch angles raises the need for in-depth investigation, particularly in scenarios where rotor blades could encounter dynamic stall. The interaction between blades from different rotors might significantly impact the dynamic stall behavior within the CCR configuration. This aspect requires further, detailed examination to better understand the complexities of rotor dynamics in various operating conditions.

(d) An enhanced model that effectively captures the substantial coupling between the upper and lower blades is necessary to provide precise predictions of blade crossover effects. These models could be developed based on linearized unsteady aerodynamic theories, possibly incorporating empirical corrections to better account for the intricate interactions involved in blade crossover events. Such an improved modeling approach is pivotal for advancing the understanding and prediction of these phenomena.

References

[1] Lockheed Martin. *BLACK HAWK Helicopters*, 2017. https://www.lockheedmartin.com.

[2] Wikipedia. *Boeing AH-64 Apache*, 2013. https://en.wikipedia.org/wiki/Boeing_AH-64_Apache.

[3] National Air and Space Museum. Hiller XH-44 Hiller-Copter. https://airandspace.si.edu.

[4] NASA. NASA's Aeronautics Experts Help Prepare Ingenuity to Fly on Mars, 2020. https://www.nasa.gov.

[5] Puneet Singh. *Aeromechanics of Coaxial Rotor Helicopters using the Viscous Vortex Particle Method*. PhD thesis, 07 2020.

[6] Manikandan Ramasamy. Hover Performance Measurements Toward Understanding Aerodynamic Interference in Coaxial, Tandem, and Tilt Rotors. *Journal of the American Helicopter Society*, 60(3):1–17, 2015.

[7] Experimental Investigation of Rotorcraft Outwash in Ground Effect. In *71th Annual Forum of the American Helicopter Society*, 2015.

[8] Puneet Singh and Peretz P. Friedmann. Application of Vortex Methods to Coaxial Rotor Wake and Load Calculations in Hover. *Journal of Aircraft*, 55(1):373–381, sep 2017.

[9] Qiulin Qu, Pingyang Zuo, Wei Wang, Peiqing Liu, and Ramesh K Agarwal. Numerical investigation of the aerodynamics of an airfoil in mutational ground effect. *AIAA Journal*, 53(10):3144–3154, 2015.

[10] Felipe Bohorquez. Rotor Hover Performance and System Design of an Efficient Coaxial Rotary Wing Micro Air Vehicle. 2007.

[11] Tomohisa Ohtake, Yusuke Nakae, and Tatsuo Motohashi. Nonlinearity of the aerodynamic characteristics of naca0012 aerofoil at low reynolds numbers. *Japan Society of Aeronautical Space Sciences*, 55(644):439–445, 2007.

[12] Kenneth Munson and John W Wood. Helicopters and other rotorcraft since 1907: the pocket encyclopedia of world aircraft in color. *(No Title)*.

[13] AJ Ruddell, W Groth, and R McCutcheon. *Advancing blade concept (ABC) technology demonstrator*. The Laboratory, 1981.

[14] Marion K Taylor. A balsa-dust technique for air-flow visualization and its application to flow through model helicopter rotors in static thrust. nov 1950.

[15] Robert D Harrington. Full-Scall-Tunnel Investigation of The Static-Thrust Performence of a Coaxial Helicopter Rotor. *NACA Technical Note 2318*, 5(1980):5–7, mar 1951.

[16] Alfred Gessow. Effect of rotor-blade twist and plan-form taper on helicopter hovering performance. Technical report, 1948.

[17] V M Paglino. Forward flight performance of a coaxial rigid rotor. In *Proceedings of the 27th American Helicopter Society Forum, Washington, DC*, 1971.

[18] R F Klingloff. Rigid coaxial rotor system stability and control characteristics. In *Proceedings of the 32nd American Helicopter Society Forum, Washington, DC*, 1976.

[19] M J Andrew. Co-axial rotor aerodynamics in hover. 1980.

[20] T Nagashima and K Nakanishi. Optimum performance and wake geometry of co-axial rotor in hover. 1981.

[21] V A Anikin. Aerodynamic-features of a coaxial rotor helicopter. 1991.

[22] Colin P Coleman. A Survey of Theoretical and Experimental Coaxial Rotor Aerodynamic Research. *NASA Technical Paper*, (March):1–25, 1997.

[23] MC Cheney. The abc helicopter. *Journal of the American Helicopter Society*, 14(4):10–19, 1969.

[24] T Nagashima, K Shinohara, and T Baba. A flow visualization study for the tip vortex geometry of the coaxial counter rotating rotor in hover. *Technical note*, pages 442–445, 1978.

[25] Anton J. Landgrebe. Wake geometry of a hovering helicopter rotor and its influence on rotor performance. *Journal of the American Helicopter Society*, 17(4):3–15, 1972.

[26] K.W. McAlister, C. Tung, O. Rand, V. Khromov, and J.S. Wilson. Experimental and Numerical Study of a Model Coaxial Rotor. may 2006.

[27] Lokesh Silwal, Karlyle Munz, and Vrishank Raghav. Development and validation of a thrust-scaled counter-rotating coaxial rotor to study interactional aerodynamics. In *AIAA Scitech 2019 Forum*, page 1100, 2019.

[28] Patrick Mortimer, Jayant Sirohi, Stefan Platzer, and Juergen Rauleder. Coaxial Rotor Wake Measurements in Hover Using Phase-Resolved and Time-Resolved PIV. In *The Vertical Flight Society's 75th Annual Forum*. AHS International, 2019.

[29] Lokesh Silwal and Vrishank Raghav. Preliminary study of the near wake vortex interactions of a coaxial rotor in hover. In *AIAA Scitech 2020 Forum*. American Institute of Aeronautics and Astronautics (AIAA), jan 2020.

[30] Dhwanil Shukla and Narayan Komerath. Drone scale coaxial rotor aerodynamic interactions investigation. *Journal of Fluids Engineering, Transactions of the ASME*, 141(7), jul 2019.

[31] Mehmet Fatih Konus. *Vortex Wake of Coaxial Rotors in Hover*. PhD thesis, University of California, Berkeley, 2017.

[32] Hover Performance Correlation for Full-Scale and Model-Scale Coaxial Rotors. *Journal of the American Helicopter Society*, 54(3):32005, 2009.

[33] J. Lee, Kwanjung Yee, and S. Oh. Numerical investigation of dual rotors using a time-marching free-wake method. volume 1, pages 71–85, 01 2008.

[34] Jimmy C. Ho, Hyeonsoo Yeo, and Mahendra Bhagwat. Validation of rotorcraft comprehensive analysis performance predictions for coaxial rotors in hover. *Journal of the American Helicopter Society*, 62(2), apr 2017.

[35] Vinod K. Lakshminarayan and James D. Baeder. High-resolution computational investigation of trimmed coaxial rotor aerodynamics in hover. *Journal of the American Helicopter Society*, 54(4), oct 2009.

[36] J. Gordon Leishman and Monica Syal. Figure of merit definition for coaxial rotors. *Journal of the American Helicopter Society*, 53(3):290–300, jul 2008.

[37] Seongkyu Lee and Maxime Dassonville. Iterative blade element momentum theory for predicting coaxial rotor performance in hover. *Journal of the American Helicopter Society*, 65(4):1–12, 2020.

[38] Montgomery Knight and Ralph A Hegner. Analysis of ground effect on the lifting airscrew. 1941.

[39] Naohiro Iboshi, Noriaki Itoga, JVR Prasad, and Lakshmi N Sankar. Ground effect of a rotor hovering above a confined area. *Frontiers in Aerospace Engineering*, 3(1):7–16, 2014.

[40] J. Zbrozek. Ground Effect on the Lifting Rotor. *ARC RM 2347*, pages 1–8, 1950.

[41] Jeffrey S. Light. Tip vortex geometry of a hovering helicopter rotor in ground effect. *Journal of the American Helicopter Society*, 38(2):34–42, 1993.

[42] D. Zagaglia, A. Zanotti, and G. Gibertini. Analysis of the loads acting on the rotor of a helicopter model close to an obstacle in moderate windy conditions. *Aerospace Science and Technology*, 78:580–592, 2018.

[43] IC Cheeseman and WE Bennett. The effect of the ground on a helicopter rotor in forward flight. *British RM No. 3021*, 1955.

[44] Albert Betz. The ground effect on lifting propellers. Technical report, 1937.

[45] J.S. Hayden. The Effect of the Ground on Helicopter Hovering Power Required. In *Proc. AHS 32nd Annual Forum*, 1976.

[46] Jürgen Rauleder and J Gordon Leishman. Flow environment and organized turbulence structures near a plane below a rotor. *AIAA journal*, 52(1):146–161, 2014.

[47] Jürgen Rauleder and J Gordon Leishman. Particle–fluid interactions in rotor-generated vortex flows. *Experiments in fluids*, 55:1–15, 2014.

[48] Federico Rovere, George Barakos, and Rene Steijl. Safety analysis of rotors in ground effect. *Aerospace Science and Technology*, 129:107655, 2022.

[49] Manikandan Ramasamy and Gloria K. Yamauchi. Using model-scale tandem-rotor measurements in ground effect to understand full-scale CH-47D outwash. In *Journal of the American Helicopter Society*, volume 62. American Helicopter Society, jan 2017.

[50] Ali Mehrabi and Ali R Davari. Outwash flow measurement around the subscale tandem rotor in ground effect. *Engineering Science and Technology, an International Journal*, 23(6):1374–1384, 2020.

[51] W.P. Schane. Effects of Downwash Upon Man. Technical report, U.S. Army Aeromedical Research unit, Fort Rucker,AL, 1967.

[52] Daiju Uehara, Jayant Sirohi, and Mahendra J Bhagwat. Hover performance of corotating and counterrotating coaxial rotors. *Journal of the American Helicopter Society*, 65(1):1–8, 2020.

[53] Charles E Tinney and John Valdez. Thrust and acoustic performance of small-scale, coaxial, corotating rotors in hover. *AIAA Journal*, 58(4):1657–1667, 2020.

[54] Christopher Cameron, Jayant Sirohi, Roland Feil, and Jürgen Rauleder. Measurement of transient loads and blade deformation in a coaxial counter-rotating rotor. *Annual Forum Proceedings - AHS International*, (June 2020):1334–1345, 2017.

[55] Daiju Uehara, Jayant Sirohi, Roland Feil, and Jürgen Rauleder. Blade Passage Loads and Deformation of a Coaxial Rotor System in Hover. *Journal of AIrcraft*, 56(6):2144–2157, sep 2019.

[56] Rajneesh Singh, Hao Kang, Christopher Cameron, and Jayant Sirohi. Computational and Experimental Investigations of Coaxial Rotor Unsteady Loads. In *54th AIAA Aerospace Sciences Meeting*. American Institute of Aeronautics and Astronautics (AIAA), jan 2016.

[57] Zhongqi Jia and Seongkyu Lee. Impulsive loading noise of a lift-offset coaxial rotor in high-speed forward flight. *AIAA Journal*, 58(2):687–701, 2020.

[58] Bo Wang, Chenkai Cao, Qijun Zhao, Xin Yuan, and Zheng Zhu. Aeroacoustic Characteristic Analyses of Coaxial Rotors in Hover and Forward Flight. *International Journal of Aeronautical and Space Sciences 2021*, pages 1–15, aug 2021.

[59] Natasha L Barbely, Narayanan M Komerath, and Luke A Novak. A study of coaxial rotor performance and flow field characteristics. Technical report, Georgia Institute of Technology Atlanta United States, 2016.

[60] Wenbo Zhu, Matthew H McCrink, Jeffrey P Bons, and James W Gregory. The unsteady kutta condition on an airfoil in a surging flow. *Journal of Fluid Mechanics*, 893, 2020.

[61] Takanobu Ogawa and Kozo Fujii. Numerical simulation of compressible flow induced by a train moving in a tunnel. In *23rd Fluid Dynamics, Plasmadynamics, and Lasers Conference*, page 2951, 1993.

[62] Patricia Coton. Study of environment effects by means of scale model flight tests in a laboratory. In *21st ICAS Congress*, pages 13–18, 1998.

[63] Shih-An Yang and Pan-An Luh. A numerical simulation of hydrodynamic forces of ground-effect problem using lagrange's equation of motion. *International journal for numerical methods in fluids*, 26(6):725–747, 1998.

[64] Jeremy Shipman, Srinivasan Arunajatesan, Peter Cavallo, Neeraj Sinha, and Susan Polsky. Dynamic cfd simulation of aircraft recovery to an aircraft carrier. In *26th AIAA Applied Aerodynamics Conference*, page 6227, 2008.

[65] Benton H Lau, Alan J Wadcock, and James T Heineck. Wake visualization of a full-scale tiltrotor in hover. 1998.

[66] Bernhard Wieneke. PIV uncertainty quantification from correlation statistics. *Measurement Science and Technology*, 26(7):074002, jun 2015.

[67] Andrea Sciacchitano. Uncertainty quantification in particle image velocimetry. *Measurement Science and Technology*, 30(9):092001, 2019.

[68] M Samimy and SK Lele. Motion of particles with inertia in a compressible free shear layer. *Physics of Fluids A: Fluid Dynamics*, 3(8):1915–1923, 1991.

[69] Jerry Westerweel. Fundamentals of digital particle image velocimetry. *Measurement science and technology*, 8(12):1379, 1997.

[70] Jie-Zhi Wu, Ze-Liang Pan, and Xi-Yun Lu. Unsteady fluid-dynamic force solely in terms of control-surface integral. *Physics of Fluids*, 17(9):098102, sep 2005.

[71] Ali Mohebbian and David E. Rival. Assessment of the derivative-moment transformation method for unsteady-load estimation. *Experiments in Fluids 2012 53:2*, 53(2):319–330, mar 2012.

[72] S. Wang, Y. Zhou, Md. Mahbub Alam, and H. Yang. Turbulent intensity and Reynolds number effects on an airfoil at low Reynolds numbers. *Physics of Fluids*, 26(11):115107, nov 2014.

[73] Gordon J Leishman. *Principles of helicopter aerodynamics*. Cambridge university press, 2006.

[74] Wayne Johnson. *Helicopter Theory*. Princeton University Press, Princeton, NJ, 1980.

[75] Thomas J Mueller and Stephen M Batill. Experimental studies of separation on a two-dimensional airfoil at low reynolds numbers. *AIAA journal*, 20(4):457–463, 1982.

[76] Dong-Ha Kim, Jo-Won Chang, and Joon Chung. Low-reynolds-number effect on aerodynamic characteristics of a naca 0012 airfoil. *Journal of aircraft*, 48(4):1212–1215, 2011.

[77] J Mayo Greenberg. Airfoil in sinusoidal motion in a pulsating stream. Technical report, 1947.

[78] Philip B Kirk and Anya R Jones. Vortex formation on surging aerofoils with application to reverse flow modelling. *Journal of fluid mechanics*, 859:59–88, 2019.

[79] Herbert Wagner. Über die entstehung des dynamischen auftriebes von tragflügeln. 1924.

[80] Robert T Jones. The unsteady lift of a wing of finite aspect ratio. Technical report, 1940.

[81] Luke R Smith and Anya R Jones. Vortex formation on a pitching aerofoil at high surging amplitudes. *Journal of Fluid Mechanics*, 905:A22, 2020.

[82] Avi Zaide and Daniella Raveh. Numerical simulation and reduced-order modeling of airfoil gust response. *AIAA journal*, 44(8):1826–1834, 2006.

[83] Jenn-Long Liu. Computations of two passing-by high-speed trains by a relaxation overset-grid algorithm. *International journal for numerical methods in fluids*, 44(12):1299–1315, 2004.

[84] Camli Badrya, Bharath Govindarajan, and Inderjit Chopra. Basic understanding of unsteady airfoil aerodynamics at low reynolds numbers. In *2018 AIAA Aerospace Sciences Meeting*, page 2061, 2018.

[85] Theodore Theodorsen. General theory of aerodynamic instability and the mechanism of flutter. Technical report, 1935.

[86] Christoph Stangfeld, Christopher L Rumsey, Hanns Mueller-Vahl, David Greenblatt, C Nayeri, and Christian O Paschereit. Unsteady thick airfoil aerodynamics: experiments, computation, and theory. In *45th AIAA Fluid Dynamics Conference*, page 3071, 2015.

[87] Valentina Motta, Alberto Guardone, and Giuseppe Quaranta. Influence of airfoil thickness on unsteady aerodynamic loads on pitching airfoils. *Journal of Fluid Mechanics*, 774:460–487, 2015.

[88] Peter D Lysak, Dean E Capone, and Michael L Jonson. Prediction of high frequency gust response with airfoil thickness effects. *Journal of Fluids and Structures*, 39:258–274, 2013.

[89] HG Küssner and WP Jones. Nonstationary theory of airfoils of finite thickness in incompressible flow. *AGARD manual on aeroelasticity, Part*, 2, 1960.

[90] William R Sears. Some aspects of non-stationary airfoil theory and its practical application. *Journal of the Aeronautical Sciences*, 8(3):104–108, 1941.

[91] Di Peng and James W Gregory. Vortex dynamics during blade-vortex interactions. *Physics of Fluids*, 27(5), 2015.

[92] Di Peng and James W Gregory. Asymmetric distributions in pressure/load fluctuation levels during blade-vortex interactions. *Journal of Fluids and Structures*, 68:58–71, 2017.

[93] Esteban AL Hufstedler and Beverley J McKeon. Vortical gusts: experimental generation and interaction with wing. *AIAA Journal*, 57(3):921–931, 2019.

Appendix A

Facility fabrication considerations

The facilities used in this study were constructed for the first time in this department and required substantial efforts to develop and benchmark. As future work, it's essential to maintain and enhance the capabilities of these facilities to ensure their ongoing utility. In this context, the subsequent section outlines key factors and considerations for the maintenance and improvement of these facilities.

A.1 Aerodynamic coaxial rotor thrust stand

Constructing a facility of this nature necessitates careful consideration of potential challenges, one of the most critical being the issue of vibrations. Resonance between the rotational frequency of the rotor and the thrust stand can lead to damaging vibrations that affect not only the facility's operation but also its structural integrity. During the construction of this facility, resonance was encountered at a rotational frequency of 1000 RPM, which initially seemed to jeopardize the ability to reach the desired operational RPM of 1500. Fortunately, a solution was identified: using dampers located beneath the rotor hubs.

The selection of the dampers is of paramount importance. In this context, the most effective dampers were found to be those offered by a company named Sorbothane[1]. These dampers, when correctly employed, significantly reduced the severity of vibrations during resonance. Although some vibrations remained, they were substantially mitigated, enabling the facility to operate above the resonant frequency and achieve the desired operational conditions.

[1]Link to the company website: https://www.sorbothane.com/

It's essential to emphasize that vibrations can be highly detrimental to the load cells utilized to measure rotor performance. Vibrations may introduce additional, unwanted loads to the strain gauges, potentially causing damage that cannot be rectified. To address this issue, a mock-up load cell was manufactured to conduct preliminary tests under various operating conditions. Only after confirming that vibrations had minimal impact on the facility were the actual load cells mounted for data collection. This precaution was vital in preserving the integrity of the load cells and the reliability of the experimental results. After the load cells were installed for data collection, it remained crucial to verify that the measurements obtained were not tainted by any inherent vibrations that could introduce noise into the data. To achieve this, a Fast Fourier Transformation (FFT) was conducted on the thrust measurements. The results of this analysis are presented in the following section.

A.1.1 Characterization of the unsteady effects

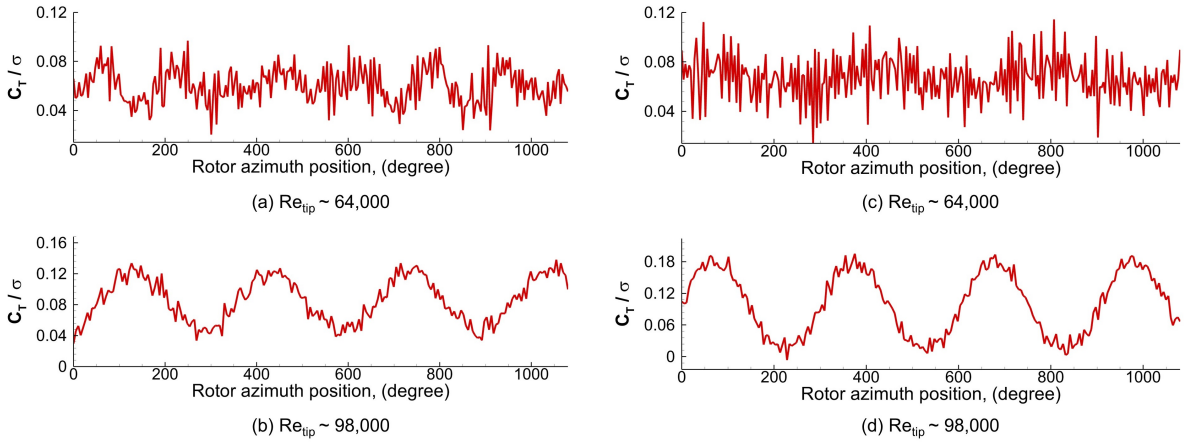

Figure A.1: Instantaneous variation in the thrust of the counter-rotating coaxial rotor at an axial separation distance of $d/R = 0.14$ and high thrust settings: (a) Lower Rotor at Re_{tip} 64000, (b) Lower Rotor at Re_{tip} 98000, (c) Upper Rotor at Re_{tip} 64000, (d) Upper Rotor at Re_{tip} 98000

First, the instantaneous variation in thrust produced by both the upper and lower rotors was examined for three cycles of rotation, and the results are summarized in Fig. A.1. For this comparison, an arbitrary case of CCR at a rotor spacing of $d/R = 0.14$ and high thrust settings was considered. The analysis revealed periodic variations in the instantaneous thrust produced by the rotor, with one cycle corresponding to one rotor revolution. Notably, for the low Re_{tip} condition, the mean sinusoidal path exhibited higher fluctuations in thrust (see Fig.A.1 a & c).

These fluctuations were reduced for the case of high Re_{tip} of 98000, as observed in Fig.A.1 b & d. To further explore these variations, frequency spectrum analysis of the instantaneous thrust data was conducted using Fourier Transform analysis. MATLAB was employed to compute the FFT of the instantaneous thrust data for upper and lower rotors under higher thrust conditions in single and CCR configurations, with a rotor spacing of $d/R = 0.14$.

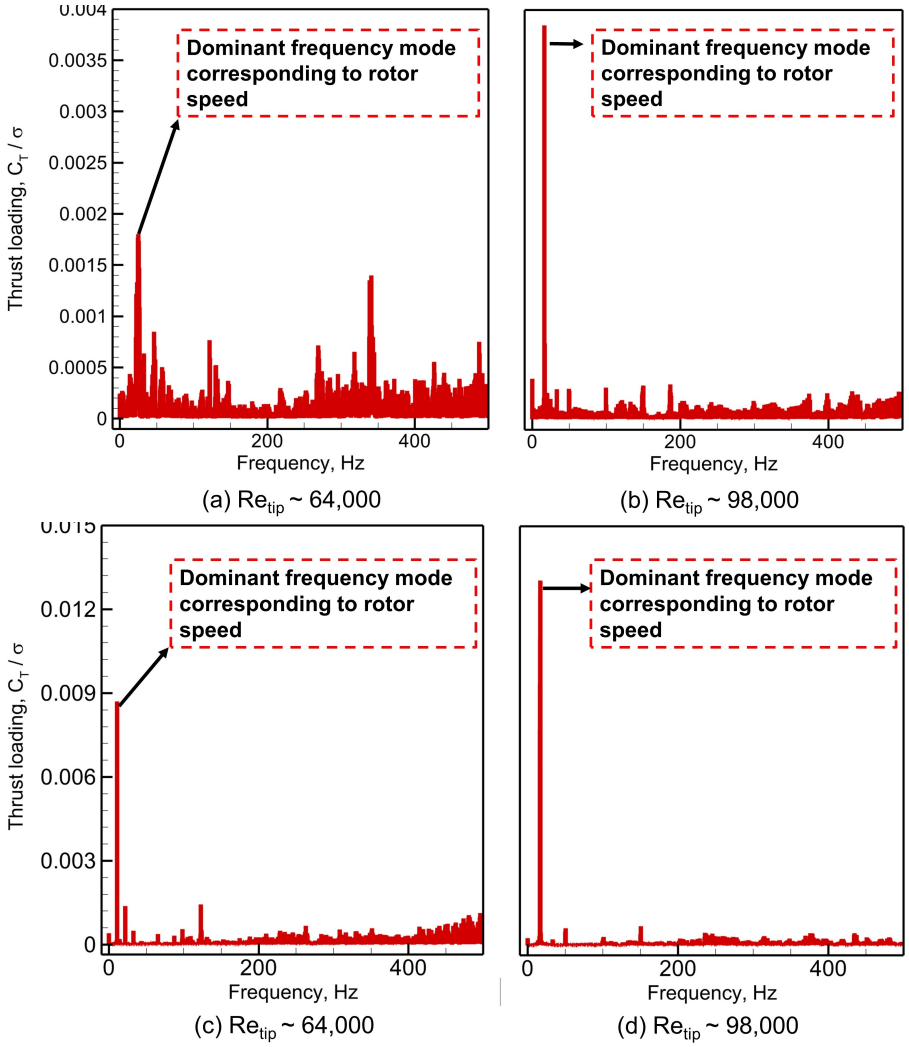

Figure A.2: FFT for the upper and lower rotor at coaxial rotor configuration for a collective pitch of 10° at $d/R = 0.14$ spacing, (a) Lower rotor at Re_{tip} 64000, (b) Lower rotor at Re_{tip} 98000, (c) Upper rotor at Re_{tip} 64000, (d) Upper rotor at Re_{tip} 98000

Figure A.2 presents an overview of the frequency content of the instantaneous thrust for both the upper and lower rotors in a single rotor configuration during hover. When comparing the frequency spectrum between the upper and lower rotors in the single rotor configuration at Re_{tip} of 64000, it was evident that the lower rotor exhibited a higher number of frequency

modes (Fig.A.2a) compared to the upper rotor(Fig. A.2c). The most dominant frequency mode observed for both rotors corresponded to the rotational speed of the rotor. Increasing the Reynolds number dampened the higher frequency modes while augmenting the lower frequency mode, as clearly seen in Fig. A.2.

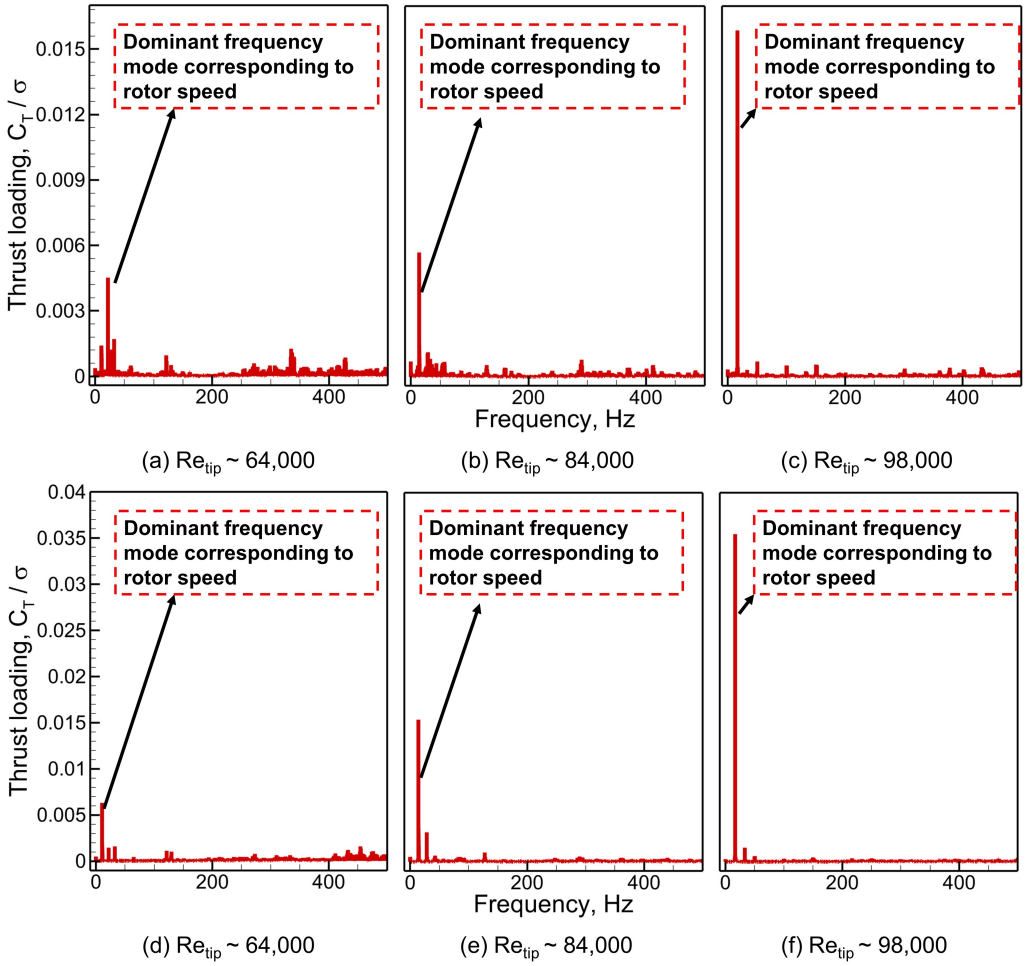

Figure A.3: FFT for the upper and lower rotor at coaxial rotor configuration for the collective pitch of 10° at $d/R = 0.14$ spacing, (a) Lower rotor at Re_{tip} 64000, (b) Lower rotor at Re_{tip} 84000, (c) Lower rotor at Re_{tip} 98000, (d) Upper rotor at Re_{tip} 64000, (e) Upper rotor at Re_{tip} 84000, (f)Upper rotor at Re_{tip} 98000

Figure A.3 provides an overview of the frequency content of the instantaneous thrust in a coaxial configuration with an axial separation distance of $d/R = 0.14$ while operating under high thrust hover conditions. This analysis compares two different Reynolds number conditions for the CCR at the specified axial separation distance. One of the notable observations from this analysis is the distinct difference in the frequency content of the thrust produced by the

upper and lower rotors. Specifically, in the higher frequency modes, the upper rotor exhibits much lower amplitudes than the lower rotor, as evident in Fig. A.3.

This phenomenon can be attributed to the influence of rotor interactions, particularly because the lower rotor operates within the wake of the upper rotor. This wake interaction likely contributes to the dampening of higher frequency modes observed in the thrust produced by the lower rotor, as compared to the higher frequency modes observed in the single rotor configuration for the lower rotor. Furthermore, the change in Reynolds number significantly impacts the higher frequency modes for both the upper and lower rotors. While there were subtle differences in the frequency content between single and CCR configurations and different Reynolds numbers, the dominant frequency for all these cases still corresponded to the rotor rotational frequency. This suggests that the loadcell measurements are free from any inherent vibrations induced by the thrust stand.

A.2 Hydrodynamic towing tank facility

One important consideration for this facility was the use of transformers. The motor and driver were procured from China, and they were designed for use with 220V outlets. To operate the motor in the United States, a step-up transformer had to be acquired. During the initial development of this facility, significant challenges related to electromagnetic interference (EMI) and vibrations were encountered. The following section provides an overview of how these issues were addressed.

A.2.1 Electromagnetic interference

The facility incorporates a high-powered AC servo motor with a 750 Watts capacity. The system comprises a motor and a driver, with two cables connecting them, one for communication and the other for powering the motor. In the initial setup, the driver was placed on the floor, and the motor was elevated to actuate the linear actuators. This configuration resulted in a dangling power cable, which was a major source of EMI. This EMI issue arose due to poor grounding

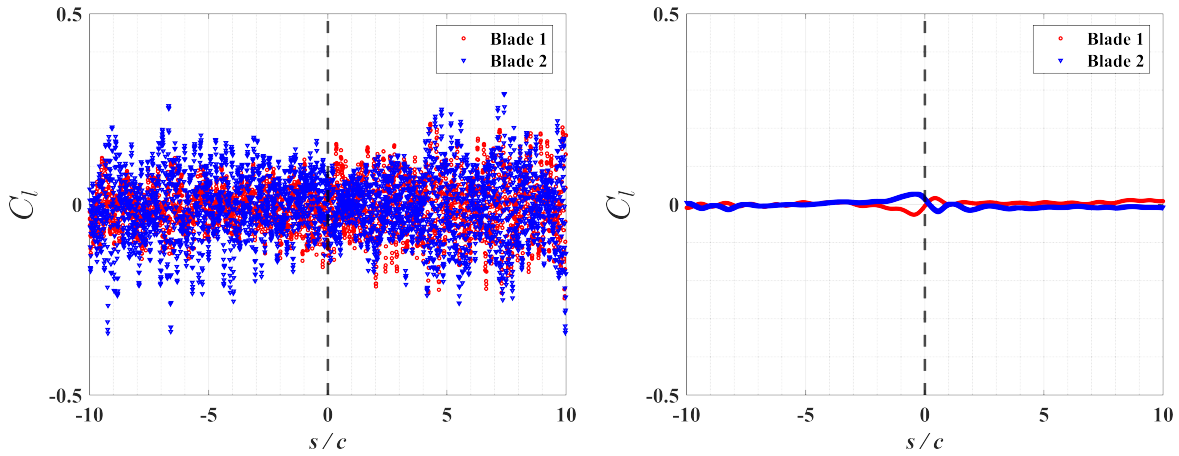

(a) Raw data (b) After applying digital filtering

Figure A.4: Sample data to show the difference between the raw data and post-processing using a frequency filter. A specific case of blade crossover at $\alpha = 0°$ and $Re = 15000$ was used for demonstration purposes.

between the driver and the motor. The consequences of this EMI could be significant, especially for the load cell measurements, given that the load cell signals are in the millivolt range. Therefore, it was imperative to minimize the impact of EMI.

To address this issue, the driver and the motor were placed on the same platform, establishing a common ground for both the motor and the driver. This reduced the EMI induced by the power cable to a considerable extent. Additionally, an EMI filter was inserted between the power connection and the driver to prevent motor-generated EMI from interfering with other circuits. These measures significantly mitigated the effects of EMI on the load measurements.

A.2.2 Vibrations

Vibrations induced by various system components, including the bevel gear, the motor, and the teeth of the belt driving the linear actuators, significantly affected the load cell measurements. These vibrations introduced high-frequency noise into the load cell data. Identifying and mitigating the source of these vibrations proved challenging. To address this issue, digital filtering was employed as a post-processing method to eliminate the high-frequency noise in the data. The specific filter used was the Butterworth filter, a low-pass frequency filter. This filter can be designed in MATLAB using the built-in function ”butter.” The designed filter was then applied

to the data using another MATLAB function, "filtfilt," which ensured no phase differences were introduced into the data.

For all cases, a low-pass frequency of $30Hz$ was used in the filtering process. This frequency was chosen based on the determination that the frequency of the blade crossover event, occurring at a maximum velocity of $U_\infty = 0.97m/s$ was less than $20Hz$. The effectiveness of the digital filtering process in dealing with noisy data is highlighted in Fig. A.4. This figure illustrates the comparison between raw data and data subjected to post-processing through digital frequency filtering.

Appendix B

Products during the graduate program

Manuscripts under review/preparation

1. **Silwal, L.**, Bhargav, V., Stubbs, D.C., Fulone, B., Thurow, B.S., Scarborough, D.E., and Raghav, V. "Ejecta Behavior during Plume-Surface Interactions under Rarefied Atmospheric Conditions." Acta Astronautica (2023).

2. **Silwal, L.**, Gururaj, A., Youngblood, C., Mettelsiefen, H., and Raghav, V. "Development and validation of a hydrodynamic towing tank facility to study unsteady aerodynamic interactions." (2024).

3. **Silwal, L.**, and Raghav, V. "Blade aerodynamic characteristics during blade crossover." (2024).

4. Stubbs, D.C., **Silwal, L.**, Bhargav, V., Thurow, B.S., Raghav, V., and Scarborough, D.E. "Non-intrusive, 3-D Crater Formation Measurements Due to Plume-Surface Interactions Under Sub-Atmospheric Pressure Conditions." (2024).

Journal publications

1. **Silwal, L.**, Bhagwat, M.J., and Raghav, V. "Aerodynamic Interactions of Counter-Rotating Coaxial Rotors Hovering in Ground Effect." Journal of Aircraft (2022): 1-10.

2. Stubbs, D.C., **Silwal, L.**, Thurow, B.S., Hirabayashi, M., Raghav, V., and Scarborough, D.E. "Three-Dimensional Measurement of the Crater Formation During Plume–Surface Interactions Using Stereo-Photogrammetry." AIAA Journal 60.3 (2022): 1316-1331.

3. Tan, Z.P., **Silwal, L.**, Bhatt, S.P., and Raghav, V. "Experimental Characterization of Speech Aerosol Dispersion Dynamics." Scientific Reports 11.1 (2021): 1-12.

Conference publications

1. Stubbs, D.C., **Silwal, L.**, Thurow, B.S., Hirabayashi, M., Raghav, V., and Scarborough, D.E. "Non-intrusive, 3-D Crater Formation Measurements Due to Plume-Surface Interactions Under Sub-Atmospheric Pressure Conditions." AIAA Scitech 2023 Forum. 2023.

2. **Silwal, L.**, Stubbs, D.C., Thurow, B.S., Hirabayashi, M., Raghav, V., and Scarborough, D.E. "Effect of Sub-atmospheric Conditions on Jet-induced Cratering on a Granular Surface." 23rd Australasian Fluid Mechanics Conference. 2022.

3. Stubbs, D.C., **Silwal, L.**, Thurow, B.S., Hirabayashi, M., Raghav, V., and Scarborough, D.E. "Non-intrusive, 3D Optical Measurements of Crater Formation due to Plume-Surface Interactions." AIAA Scitech 2021 Forum. 2021.

4. **Silwal, L.**, and Raghav, V. "Preliminary Study of the Near Wake Vortex Interactions of a Coaxial Rotor in Hover." AIAA SciTech 2020 Forum. 2020.

5. **Silwal, L.**, Munz, K., and Raghav, V. "Rotorwash Characterization of a Counter-rotating Co-axial Rotor System." The VFS Forum 75 2019.

6. **Silwal, L.**, Munz, K., and Raghav, V. "Development and Validation of a Thrust-scaled Counter-rotating Coaxial Rotor to Study Interactional Aerodynamics." AIAA Scitech 2019 Forum. 2019.

Posters and presentations

1. **Silwal, L.**, and Raghav, V. "Development and validation of a facility to study the unsteady aerodynamic interactions between lifting surfaces." APS Division of Fluid Dynamics Meeting Abstracts. 2022.

2. **Silwal, L.**, Stubbs, D.C., Thurow, B.S., Hirabayashi, M., Raghav, V., and Scarborough, D.E. "Returning to the moon safely-cratering and ejecta dynamics during plume-surface interactions." APS Division of Fluid Dynamics Meeting Abstracts. 2022.

3. **Silwal, L.**, Stubbs, D.C., Thurow, B.S., Hirabayashi, M., Raghav, V., and Scarborough, D.E. "Study of ejecta properties during plume surface interactions using three-dimensional optical diagnostic technique." APS Division of Fluid Dynamics Meeting Abstracts. 2021.

4. **Silwal, L.**, Tan, Z.P., and Raghav, V. "Three-dimensional study of the near wake of a small-scale coaxial rotor system using tomographic particle image velocimetry." APS Division of Fluid Dynamics Meeting Abstracts. 2020.

5. Rajamanickam, P., **Silwal, L.**, and Raghav, V. "Investigation of tip-vortex instability in the near-wake region of a rotor." APS Division of Fluid Dynamics Meeting Abstracts. 2020.

6. Tan, Z.P., **Silwal, L.**, Bhatt, S.P., and Raghav, V.. "Fluid Dynamics of Speech and Cough Aerosols in the Context of COVID-19 Transmission." APS Division of Fluid Dynamics Meeting Abstracts. 2020.

7. **Silwal, L.**, Stubbs, D.C., Thurow, B.S., Hirabayashi, M., Raghav, V., and Scarborough, D.E. "Study of the plume surface interaction cratering process using stereo photogrammetry." APS Division of Fluid Dynamics Meeting Abstracts. 2020.

8. Raghav, V., and **Silwal, L**. "Analysis of Unsteady Wall Jet Created by a Coaxial-Rotor in Ground Effect." APS Division of Fluid Dynamics Meeting Abstracts. 2019.

9. Swiney, P., Taylor, H., **Silwal, L.**, and Raghav, V. “Development and Validation of Helium-Filled Soap Bubble System for Time-Resolved Velocimetry.” Bulletin of the American Physical Society 63 (2018).

10. **Silwal, L.**, Munz, K., Sexton, B., Reed, N., and Raghav, V. “Wake characterization of thrust scaled counter-rotating coaxial rotor.” Bulletin of the American Physical Society 63 (2018).